ALKALI SILICA REACTION IN THE AFSLUITDIJK

Assessment of concrete damage and remaining service life using experimental and modelling research

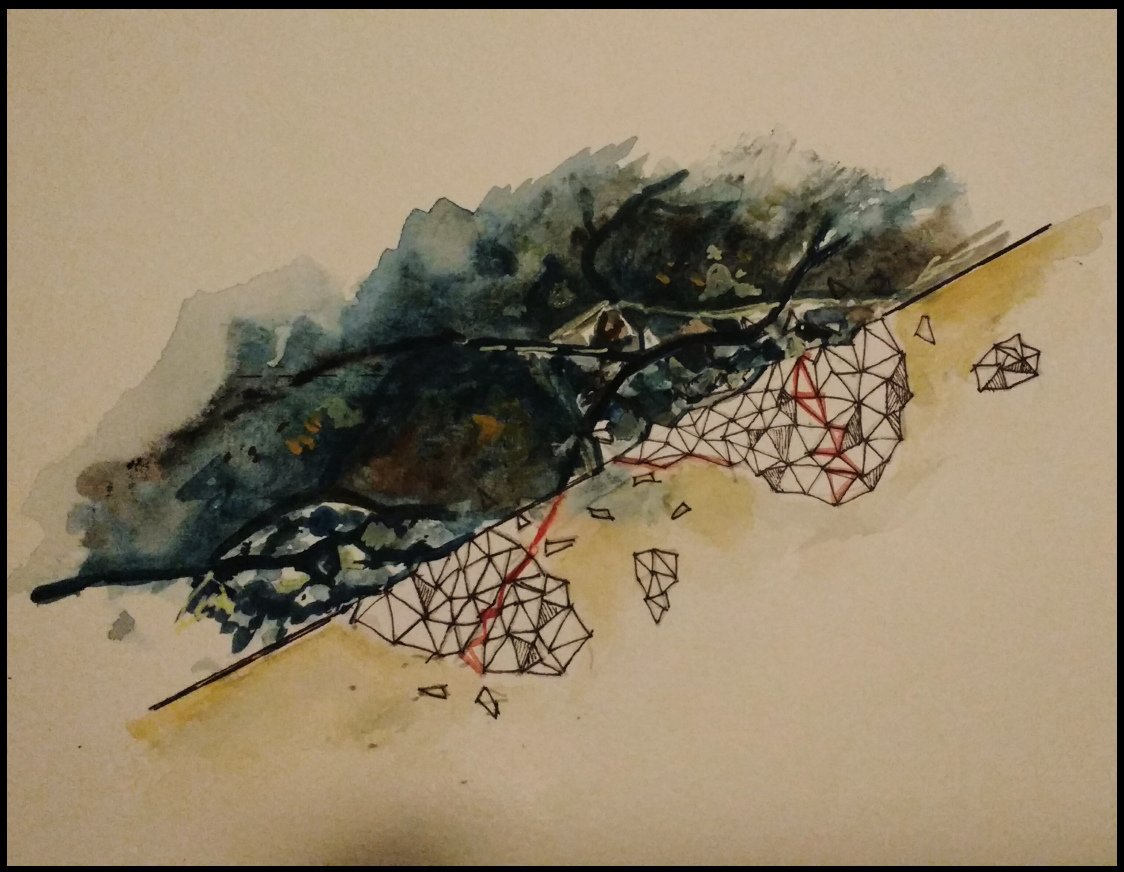

BY

AMEYA KAMAT

TU Delft

DELFT UNIVERSITY OF TECHNOLOGY

Alkali silica reaction in the Afsluitdijk: Assessment of concrete damage and remaining service life using experimental and modelling research

by

Ameya Kamat

Supervised by
Dr. Oğuzhan Çopuroğlu

Assessment committee:
Prof. Dr. Erik Schlangen
Dr. Mladena Luković
Mr. Lambert Houben

A thesis submitted in partial fulfillment for the
degree of Master of Science

in the
Civil Engineering and Geosciences
Structural Engineering: Materials and Environment

October 2017

"It's not denial. I'm just very selective about the reality I accept."

-Bill Watterson
(Calvin and Hobbes)

Abstract

Alkali Silica Reaction (ASR) is one of the degradation mechanisms in concrete that poses a threat to the service life of existing structures. This physio-chemical process is progressive and can affect the the strength, stiffness and stability of concrete structures. A lot of mitigation measures are available to prevent the deleterious effects of ASR in new structures. However, assessment and monitoring of ASR in the existing structures still remain a challenge. Thus the main aim of this thesis is to develop a simplified tool for the assessment of existing structures to assist the asset owners in decision making. This is addressed by a combination of petrographic techniques to quantify the damage and development of a numerical model to predict the remaining service life. Various existing petrographic tools (Damage rating index and image analysis) are investigated and modified to not only identify the ASR signs but also to quantify the damage. A meso-scale numerical model (ASR expansion model) is developed as an extension to the existing Delft Lattice Model to incorporate the effect of ASR by application of randomly distributed internal expansions. A case study (Aflsuitdijk, The Netherlands) is used to apply these methods. The model is compared with the findings from the petrographic analysis using a physical parameter 'crack densities'. This model is able to simulate localised network of cracks typical of ASR and expansion strains as a function of time. These expansions are compared with the permissible expansion thresholds set by RILEM and CUR to assess the remaining service life. Additionally, the numerical model showcases the importance of different boundary conditions by making a comparative study between free expansions and concrete in confined state. Finally, the limitations and drawbacks of this expansion model are discussed critically.

Acknowledgements

First and foremost I would like to thank my thesis supervisor Dr. Oğuzhan Çopuroğlu for his guidance, patience and endless support throughout the project. He was always available to answer my questions, suggest quirky ideas and provide words of encouragement whenever this journey became a bit rough. Thanks a lot for that! I would also like to express my gratitude towards my committee members: Prof. Dr. Erik Schlangen and Dr. Mladena Lukovic who took time off their busy schedules to steer me in the right direction. Prof. Schlangen's impressively creative inputs And Dr. Lukovic's critical approach helped me fix the weak spots in my thesis. I would also like to acknowledge my track coordinator Mr. Lambert Houben who ensured all my paper work went smooth so I could focus better.

I would like to thank Dr. Rob Polder for introducing me to the Afsluitdijk project and Mr. Huibert Borsje from TNO who enthusiastically provided me with the necessary information pertaining to the project and some interesting historical facts about the Afsluitdijk! I would like to extend my thanks to Mrs. Natascha de Boer from Rijkswaterstaat and Mr. Robert Haverkort from Intron for providing the concrete cores from the Afsluitdijk, without which this project would have been impossible. A special mention to Mr. Stefan Benders from Intron who not only made sure the cores were delivered on time but also labelled them neatly which made my job easy.

A special thanks to all the people who helped me on this project in one way or the other. I want to thank Caner Anac who answered all my queries over Skype calls and was kind enough to share his Matlab codes. He has been an immense help to me! I would also like to thank my colleagues Xu Ma (or Ma Xu) and Branko Savija for helping me with the lattice model. I am grateful to the most cheerful person in the Microlab: Maiko "Winston Wolf" van Leeuwen who always had solutions to all my lab problems and took a keen interest to help me with all the lab work. I would also like to thank Jakub Pawlowicz, Ton Blom and Arjan Thijssen for their help. I am also grateful to my colleague Bahman Ghiassi with whom I shared my office for not only tolerating me but also making me critically aware of my results. Furthermore, I would like to thank Dr. Leandro Sanchez (University of Ottawa) for his insights in ASR quantification and Dr. Rita Esposito (TU Delft) for providing me access to some rare ICAAR proceedings.

A heart felt thanks to everyone at the Microlab for sharing the lunch table (and ofcourse providing free unlimited coffee). All my international friends from the university who made my two years in Delft memorable. Thanks a lot! I would like to thank my long time friends Adwait and Saurabh for helping me settle down in my initial days in Delft and my best friend Rasika for keeping me motivated over the entire programme. And finally, I would like to thank my parents and my sister Ruchira for their unconditional love and support.

Contents

List of Figures

List of Tables

Abbreviations

AAR	**A**lkali **A**ggregate **R**eaction
ASR	**A**lkali **S**ilica **R**eaction
BC	**B**oundary **C**onditions
CA	**C**oarse **A**ggregates
CAD	**C**oarse **A**ggregate **D**ebonded
CCA	**C**losed **Cracks** in **C**oarse **A**ggregates
CCAG	**C**losed **Cracks** in **C**oarse **A**ggregates with **G**el
CCP/CCPG	**Cracks** in **C**ement **P**aste with/without **G**el
CD	**C**rack **D**ensity
CF	**C**rack **F**raction
CT	**C**omputerised **T**omography
DLM	**D**elft **L**attice **M**odel
DRI	**D**amage **R**ating **I**ndex
FA	**F**ine **A**ggregates
FEM	**F**inite **E**lement **M**ethod
GGBFS	**G**round **G**ranulated **B**last **F**urnace **S**lag
ITZ	**Interfacial T**ransition **Z**one
LLD	**Internal Local Loads**
OPC	**O**rdinary **P**ortland **C**ement
OCCA	**O**pened **C**racks in **C**oarse **A**ggregates

PLM	**P**olarised **L**ight **M**icroscopy
PPL	**P**lane **P**olarised **L**ight
RGB	**R**ed **G**reen **B**lue **I**mage
SCM	**S**upplementary **C**ementetious **M**aterials
UV	**U**ltra **V**iolet
XPL	**C**rossed **P**olarised **L**ight
w/c	**W**ater **C**ement **R**atio

Chapter 1

Introduction

Concrete is the most widely used construction material in the world. Over the first 100 years since its existence, much attention was paid to the structural design and optimisation of the material composition. Most of these structures are reaching the end of their service life and the focus has now shifted to the maintenance and repair of these structures. Alkali Silica Reaction (ASR) is one of the complex degradation mechanism in concrete that has been posing a threat to the service life of the existing structures. Past studies have shown that the effects of ASR can be severe, progressive and can globally affect the strength, stiffness, serviceability, safety and stability of the affected structures (Swamy, 1992). Haavik and Mielenz (1991) add that even though in most cases, the overall stability of the structure is not affected, the serviceability may be seriously affected. The cracks developed because of ASR may also accelerate other mechanisms like reinforcement corrosion due to chloride ingress, carbonation or freeze/ thaw damage further deteriorating the mechanical properties of concrete (Anaç, 2016). The currently available mitigation measures; for example: controlling the moisture or using non-reactive aggregates in concrete mixes are not practically possible in most of the cases. The measures like the use of supplementary cementitious materials (SCMs) to mitigate ASR is common for designing new structures (Silva de Souza, 2016). However, this does not work for already existing structures. Since the techniques to stop the propagation is not so apparent,it is essential to look for tools to monitor the structural safety. However, it is often difficult to recognise, identify and monitor the damage in ASR (Swamy, 1992).

Since last seven decades, several laboratory tests have been performed to study this phenomenon and understand the reaction mechanism. Petrographical studies have proven to provide a good understanding of potential reactivity, yet they lack the ability to explain the severity of damage (Poole and Sims, 2015). Other methods include using laboratory

tests to correlate expansion due to ASR to the degree of expansion. These laboratory tests often called as accelerated expansion tests have to use artificial conditions like elevated temperatures and alkali levels to compensate for the time (as ASR manifests slowly) rendering the tests somewhat unreliable (Chatterji, 2005). The determination of ASR cannot thus, solely be based only on laboratory tests and field observations (Swamy, 1992). Moreover, the laboratory tests are expensive and time consuming. Storage of samples for testing for a long period of time is also posing a problem. The available methods to a large extent depend on the judgement and expertise of the petrographer, laboratory procedures, controlled environments and thus is case specific.

There is a need to quantify the damage in order to truly design sustainable, durable structures (Grattan-Bellew and Mitchell, 2006). Quantification of damage may help to estimate the state of material degradation and assist in making decisions on maintenance of existing structures. Computational modelling of the ASR damage could be a solution to tackle the existing limitations mentioned above. Numerical models to predict material degradation due to ASR have been extensively studied in the past decade. Various numerical models have proven to be reliable at various scales but not yet definitive for use at a structural level. Due to the complexity of the reaction, the multiscale modelling approach remains a challenge. The lattice model developed by Schlangen and van Mier (1992) has been successfully used to simulate cracking and material response due to mechanical loading. The same model was used in an attempt to simulate fracture due to ASR under free expansion conditions. The study was conducted by TU Delft as a part of Performance Assessment tool for ASR (PAT-ASR) in 2011 under the Integral solutions for sustainable constructions programme by Anaç (2016). The tool needs to be developed further to consider different scenarios and parameters to make it more reliable.

1.1 Objectives

This project aims to study the damage due to Alkali silica reaction in concrete. The Lorrentz sluice at Kornwerderzand in the Afsluitdijk structure is used as a case study. Parts of the structure are suspected to be affected by the alkali silica reaction after some preliminary investigations by Borsje and Swinkels (2016) especially in the foundation slab. The foremost objective thus, is to confirm the presence of damage due to ASR. The study focuses on quantification of crack features and compare the results obtained from the model simulations with the actual samples from the Lorrentz sluice. The effect of confinement on crack propagation is also an important focus of the study. A combination of petrograhpical studies and model simulations are used in the process. In

conjunction with model simulations, a complete material characterisation and estimation of the original mix design is carried out. Finally, an estimate is made over the crack propagation and potential future expansion at a material level using a simplistic model. This may provide insights to the degradation at a structural level and help the asset owner (in this case Rijkswaterstaat) to make decisions on maintenance plans.

1.2 Project plan

The project consists of three parts. Part one of the project is material characterisation and quantification of ASR micro-structural features using petrographic techniques. This part is also used to find evidence of ASR damage. This is the experimental part of project. Second parts involves working on a numerical model to predict future potential expansion under free expansions. Last part involves studying different boundary conditions (BC) and its effect on concrete fracture and expansion. This is an addition to the numerical model. The project plan is elucidated below.

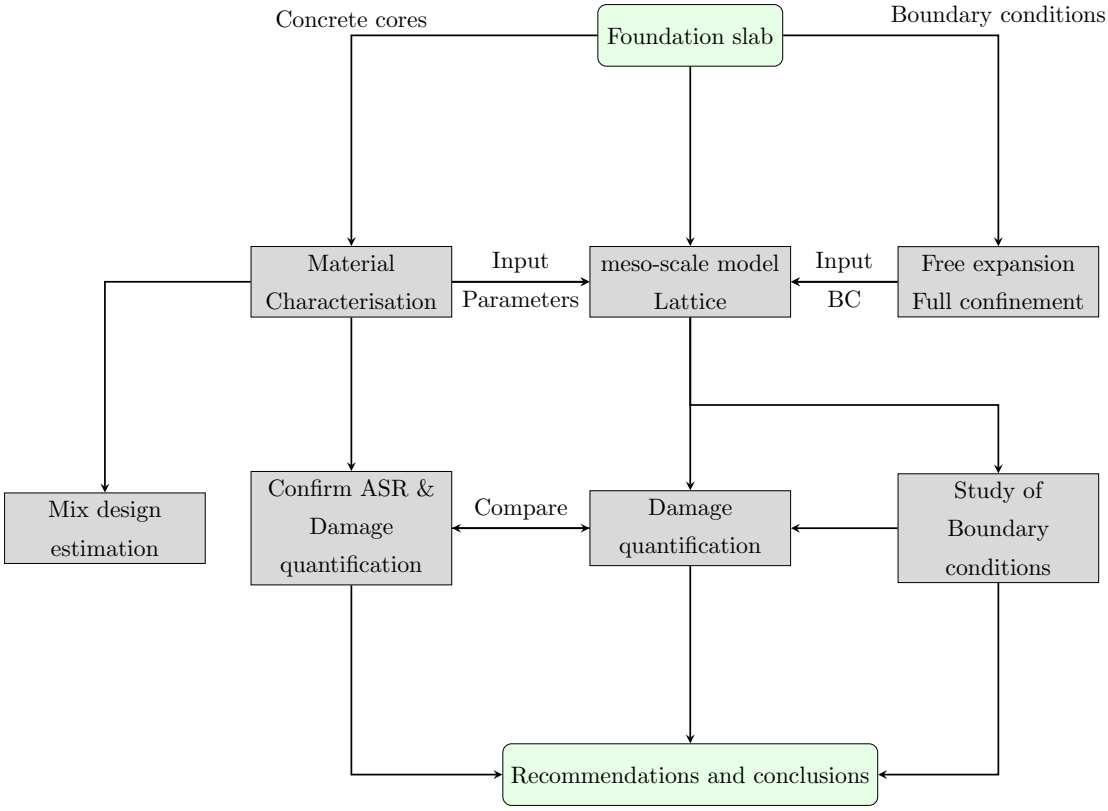

FIGURE 1.1: Project Plan

1.3 Thesis outline

The thesis is divided into five chapters which are followed by appendices. Chapter 1 introduces the topic and explains the scope, the motivation and the objectives of the project. This is followed by Chapter 2 which is a thorough literature review to delve deeper into the topic and get abreast with the past and current research. Chapter 3 provides a broad materials characterisation. It provides evidence to confirm presence of alkali silica reaction (ASR) and also estimates the mix design of the existing concrete. It also discusses semi-quantitative techniques to describe physical distress. Chapter 4 discusses the meso-scale modelling aspects, input approaches, model limitations and assumptions. This chapter also studies the effect of confinement on crack propagation and evolution of expansion strains within the model simulations. Finally remarks are made on the present condition of the structure, effect of boundary conditions and future expansion due to ASR. Chapter 5 is the concluding chapter to reflect on the thesis by providing concluding remarks and recommendations for future research. The two long chapters: Chapter 3 and Chapter 4 also include a concise chapter summary at their end to make this report coherent for the reader.

Chapter 2

Literature Review

2.1 Overview of alkali aggregate reaction (AAR)

The alkali aggregate reaction is a deleterious process affecting the durability of concrete infrastructure around the globe (Fournier and Bérubé, 2000). It is a complex chemical-physical process which involves an interaction between the alkalies and to some extent the calcium hydroxide between the cement paste and certain reactive phases of aggregates (Jensen, 1993, p 6). This in presence of water results in a formation of a hygroscopic gel. The gel expands in volume due to uptake of moisture generating pressure that eventually disrupts concrete (Swamy, 1992, p 21). This usually results in formation of cracks and in long term can affect the mechanical properties, stability and durability of the structure.

The alkali aggregate reaction can be divided into two main type of reactions (Poole and Sims, 2015, p 511-512):

1. Alkali Silica Reaction
   The fairly common alkali silica reaction which involves a reaction between alkalies and certain varieties of siliceous phases like opal, chalcedony, crystobalite, tridymite, volcanic glass etc. to form an expansive gel. This reaction will be the focus of this report.

2. Alkali Carbonate Reaction
   An uncommon type of AAR and observed usually in some parts of Canada. The reaction involves aggregates of argillaceous dolomitic limestones. The mechanism around this reaction is not well understood and not further discussed in this report.

The first publication and confirmation of alkali silica reaction dates back to 1940 thanks to Stanton (1940) in California. This lead to an extensive research in the coming years to investigate the mechanism of the deleterious dissolution of silica . More than 2000 cases have been reported today across the world: The USA, United Kingdom, Australia, India, Japan and European countries likes The Netherlands, Norway, Germany, Denmark etc. (Jensen, 1993). The first definitive case of ASR in the Netherlands was confirmed in 1991 via petrography. Porous chert was reported to be the main reactive coarse aggregate in the Netherlands (Broekmans, 2002). It has been observed that it takes around 5-15 years on an average for alkali silica reaction to manifest itself. (Poole and Sims, 2015)

2.2 Mechanism of ASR

There are several theories proposed to understand the mechanism of the alkali silica reaction. As per Poole, three important conditions must be fulfilled for the reaction to continue. The reaction will cease if even one of these conditions is not satisfied (Poole and Sims, 2015, p 512).

1. A high alkalinity in the pore solution.
2. Reactive phase of silica in a critical proportion range. The reactive phase depends on the structural composition of the minerals.
3. Sufficient/continuous presence of moisture. Poole states that the relative humidity should be at least 85 percent.

One of the well-known chemical mechanism theories has been proposed by Dent Glasser and Kataoka (1981). They state that the structure of silica plays a crucial role in the reaction kinetics. The silicates are composed of a chain in a 3D framework of silica (SiO_2) tetrahedron with a silica atom in the center, surrounded by 4 oxygen atoms. The arrangement of these atoms determine the reactivity of silicates. A well arranged, regular silicate structure indicating a crystalline nature is considered to be less reactive compared to its irregular poorly crystalline silicate structure (Silva de Souza, 2016). Dent-Glasser and Kataoka describe the reaction as a three step-process. In the first step of the reaction, the high pH of the pore water solution attacks the poorly crystallised silicate chains to break the Siloxane (Si-O-Si) bonds into Silanol (Si-OH) bonds.

$$Si - O - Si + H_2O \rightarrow Si - OH..OH - Si \tag{2.1}$$

The newly formed silanol bonds readily react further with the basic pore solution. Thus, the second stage involves further hydrolysis:

$$Si - OH + OH^- \rightarrow Si - O^- + H_2O \tag{2.2}$$

$$Si - O - Si + 2OH^- \rightarrow Si - O^- +^- O - Si + H_2O \tag{2.3}$$

The negative charge of the $Si-O^-$ is balanced by the readily available positively charged alkalies like Na^+ and K^+ in the pore solution to form the so called alkali-silica gel.

$$Si - O^- + Na^+ \rightarrow Si - O...Na \tag{2.4}$$

The approximate stoichiometry of the gel reaction proposed by (Dent Glasser and Kataoka, 1981) is presented as follows:

$$H_{0.38}SiO_{2.19} + 0.38Na_2O \rightarrow Na_{0.38}SiO_{2.19} +_{0.38} H_2O \tag{2.5}$$

In the third stage of the reaction, more siloxane (Si-O-Si) bridges are attacked leading to a progressive reaction. The reaction product (gel) occupies more volume than its constituent reactants and thus exerts a swelling pressure (Swamy, 1992, p65).

There are two damage mechanism theories in which the cracking initiates in concrete. In the first mechanism, dissolution of disordered silica takes place around the rims of the aggregate and the gel is formed near the inter-facial transition zone (ITZ). The resulting swelling pressure results in the formation of cracks in the matrix. The dissolution is not uniform which leads to localised gel pockets around the aggregate rim, consequently resulting in crack localisation (Haha, 2006). The other mechanism theory states that the dissolution of silica takes place in the already existing fractures or faults within the aggregate. Presence of crypto-crystalline grains with a high surface area within these faults is the catalyst for the gel formation. The gel is formed in these faults and the resulting pressure results in the opening up of these faults. consequently, the initiation of the crack starts within the aggregate and subsequently extends into the matrix. The resulting structure gives an impression of veins (Reinhardt and Mielich, 2011). The formation of gel around the aggregate makes it difficult for the alkalies to reach the reactive surface of the silica in the aggregates. The reaction now progresses only via diffusion of the ions through the gel layer. It is proposed thus, that the rate of reaction must slow down (Charpin and Ehrlacher, 2012). Golterman states that it is complex to explain the state of distress as the damage is not homogeneously distributed in concrete. The author states that the heterogeneous deleterious mechanism due to the reactive aggregates results in evolution of tensile stresses within the aggregate and

compressive stresses over the surface of the aggregates. This leads to cracking inside the aggregates in the so called tension zones and these cracks radiate outward along the outer part of the aggregates and to some extent in the surrounding cement paste (Sanchez et al., 2015).

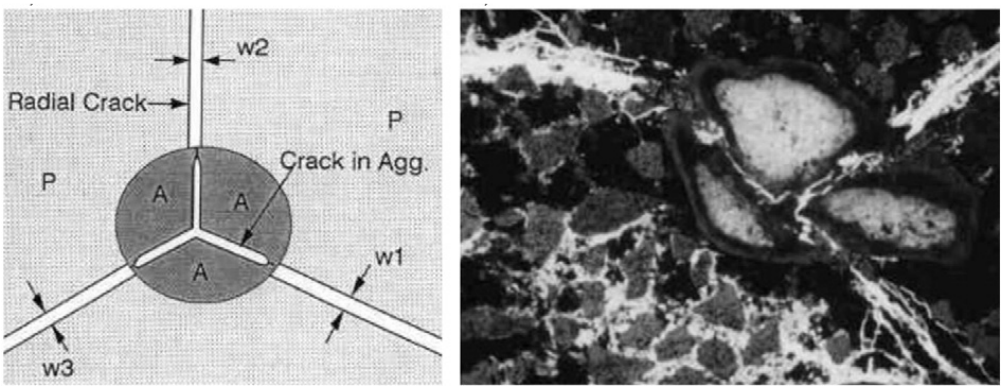

FIGURE 2.1: Radiating cracks through the aggregate (Sanchez et al., 2015)

2.3 Factors affecting ASR

Alkali Content

The alkalies present in the pore solution $[Na^+, K^+, OH^-]$ are the driving force for the alkali aggregate reaction (Diamond, 1989). The alkalies in the cement are measured in terms of 'sodium equivalent'. This correlates the sodium and potassium oxides in terms of molecular proportions. The sodium equivalent can be worked in the following way (Swamy, 1992, p35):

$$Sodium\ Equivalent = Na_2O + 0.658K_2O\ (In\ weight\ Percent) \tag{2.6}$$

However, a threshold of alkali content must be reached to initiate and sustain the expansion. This threshold also depends on the type of aggregates. It was observed further in a study of Canadian aggregates that the expansion related to AAR increased with increase in alkali content (Sodium equivalent) (Fournier and Bérubé, 2000). A sodium equivalent (Na_2O_eq) below 0.6 % of cement is considered to be harmless when it comes to alkali silica expansion (Swamy, 1992). The Federal highway administration proposed that a limiting value Na_2O_eq of $3kg/m^3$ of cement as a safe alkali limit (Federal Highway Administration, 2012). However as per the ICAAR proceedings in 2016, these limits have been exceeded in cases of highly reactive aggregates and thus may not be enough

to prevent the deleterious expansion (Andiç-Çakir et al., 2016). The alkali content in cement should not however be the only criterion to determine the sodium equivalent. The aggregates exposed to de-icing salts, sea water, natural or industrial alkali salt solutions etc. may provide additional alkalies to facilitate AAR (Diamond, 1989). Admixtures and supplementary cementitious materials are also known to increase alkali levels. In some cases even aggregates proved to be a source of alkalies (Poole and Sims, 2015, p513). The alkali concentration may also be increased because of cathodic protection at a local level resulting in an anisotropic gel expansion (Shayan and Song, 2000). These factors must also be taken into consideration while deciding the alkali limits. Evaluation of alkali profiles is necessary in such cases (Nijland and de Bruijn, 2002).

Moisture content

Moisture content is necessary for the reaction to sustain. Water has a dual role: It acts as a carrier of alkali cations and hydroxyl ions and secondly, it is absorbed by the hygroscopic gel which expands and thus exerts swelling pressure on the surrounding concrete matrix (Swamy, 1992, p30). Various literature states a relative humidity of atleast 80 to 85% is required for the reaction to proceed (Poole and Sims, 2015) and (Fournier and Bérubé, 2000). The relation between humidity and AAR expansion is seen in fig 2.2.

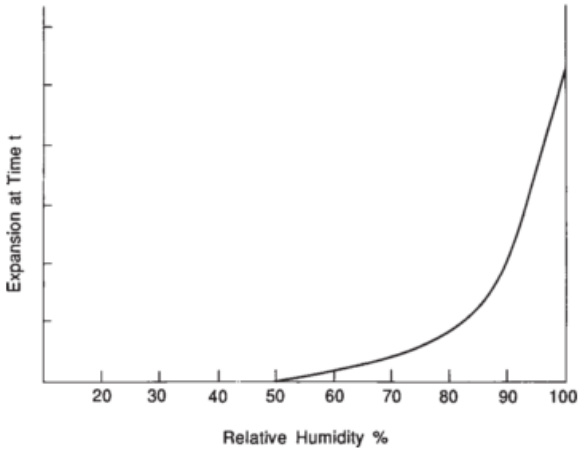

FIGURE 2.2: Relation between moisture content and AAR expansion (Swamy, 1992)

Reactive aggregates

The alkali aggregate expansion depends on the reactivity of aggregates. This is a function of aggregates' constituent minerals rather than type of rock (Swamy, 1992). The size and

structure of grains proves crucial in determining the reactivity. Smaller grain size implies more reactive surface for the alkalies to react. The reactive forms of silica as per Swamy exhibit a poorly crystalline structure with lattice defects or alternatively display an amorphous or a glassy phase (Swamy, 1992). As little as 2% by volume of reactive silica has been reported to show deleterious effects in concrete (Poole and Sims, 2015). Jensen conducted a study on 96 reacted Norwegian aggregates and concluded that the grain size between 36-60 micrometers was the most reactive (Jensen, 1993). Classification based on grain size was first introduced by Wigum (1995) and later modified by Wigum (2006). The EU PARTNER project adopted this classification to divide aggregates in three types of classes based on size of grains. This was used as the basis of petrographic assessment laid down by RILEM (Nixon and Sims, 2016).

Swamy (1992) divides reactive aggregates in 2 types: One consisting of crystalline, low density polymorphs of SiO_2 such as crystobalite and tridymite and other irregularly ordered, non-crystalline forms like Opal, Cherts, glasses etc. As per Poole and Sims, Opal, Chalecdony, Cristobalite, Tridymite and Volcanic ash can be considered to be type 1 or 'classic ASR' aggregates. Whereas, 'slow reactive/expansive' form of ASR consisting of poorly ordered forms of silica and quartz can be considered to be type 2. This expansion is based on the pressure developed by internal crystallisation rather than uptake of water (Poole and Sims, 2015) and (Jensen, 1993).

(Hobbs, 1986) came up with the concept of pessimum concentration. He observed that at a certain proportion of reactive silica to alkalies, there is a drop in expansion and slowing down of the reaction. This can be seen in fig 2.3

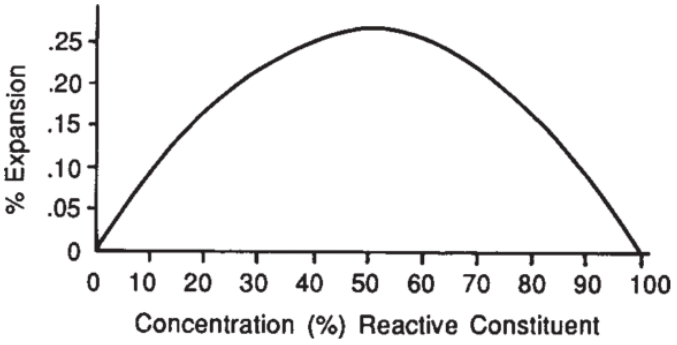

FIGURE 2.3: Effect of pessimum concentration on aggregate expansion (Swamy, 1992) and first proposed by (Hobbs, 1986)

.

2.4 Existing assessment methods

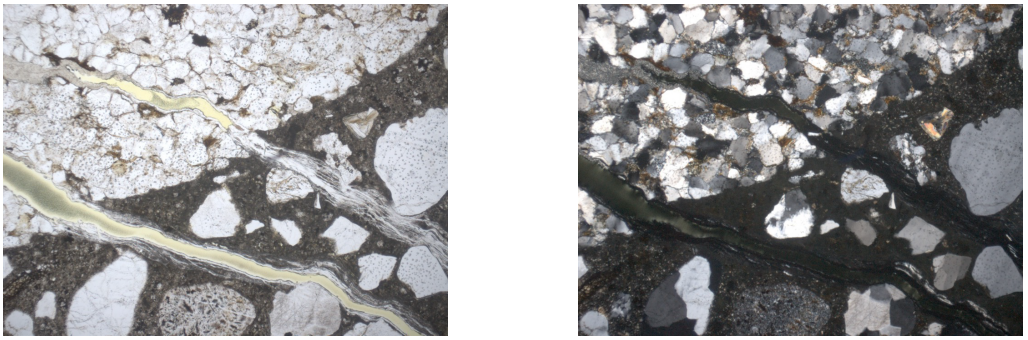

(a) (b)

FIGURE 2.4: (a) Plane polarised (PPL) image showing ASR gel through a quartzitic aggregate. (b) Cross polarised image (XPL) showing individual quartz grains and amorphous nature of gel. Image width (2.87mm) (Çopuroğlu, 2013)

2.4.1 Petrographic techniques

Concrete petrography is the study and classification of physical as well as mineralogical features of constituent components in concrete. This widely used technique in the field of applied geology can be also applied to concrete which is a man-made rock. It can be considered to be the first step in identifying potential alkali silica reactivity and ASR damage in a structure. Petrographic studies are considered cheap and effective (Broekmans, 2002). The damage is often localised and sampling should be representative to yield reliable results. This depends on the visual examination and judgement of personnel carrying out field investigation. The common signs and symptoms of ASR are well listed by Poole and Sims (2015). Some typical symptoms at structural and meso level being map cracking, presence of dark rims around the aggregates. Cracking through aggregates with presence of ASR gel can be an important sign to identify/confirm the ASR degradation. The petrographic techniques use a combination of optical and electron microscopy, image analysis and point counting techniques on representative sampling to identify potentially reactive phases (Poole and Sims, 2015). Observation of thin sections under plane polarised light (PPL) and cross polarised light (XPL) using optical microscopy can be a useful preliminary test to identify reactive components in a specimen. However, petrographic analysis fails to confirm deleterious effects of these aggregates. These tests have not been adequately able to correlate petrographically the reactivity of chalcedony, disordered silica, altered glass etc.(Poole and Sims, 2015). Petrographic techniques also exhibits certain limitations in identifying certain mineral constituents. On one hand the crystalline, metastable quartz aggregates are easy to identify while on the other hand the identification of poorly ordered, amorphous phases

of silica can be difficult using petrographic techniques. Swamy states that there is no reliable way to determine reactivity of siliceous aggregates with respect to their susceptibility to AAR. This could be because of a number of varying factors like the surface area, crystal structure and hydration (Swamy, 1992, p53).

Damage rating index

Petrographic analysis is usually a qualitative analysis and depends a lot on the skill and judgement of the petrographer, sample preparations and the available equipments. To some extent this limitation was overcome by introduction of a semi-quantitative petrographic technique called Damage Rating Index (DRI), originally introduced by Grattan-Bellew in 1995 (Grattan-Bellew and Mitchell, 2006). The method involves counting of cracks and ASR features over a polished concrete section. The counting is done at a magnification of 16x using a stereo microscope with a 1 cm^2 overlaid grid. Each counted feature inside the grid is assigned a weighing factor and finally the number of counts along with these factors are normalised to an area of 100 cm^2. This technique provides a way to differentiate between relative damage between various samples of existing cores. The method also showed a good correlation against expansion due to ASR. The results of this method were not easily reproducible since some of the petrographic features were harder to observe. The coefficient of variability was acceptable at around 20% when performed by experienced petrographers in the same laboratory. However, the variability increased to an unacceptable range when the test was performed across various laboratories (Rivard et al., 2000). This is the reason the method has still not become standardised.

In 2012 Villeneuve et al. (2012) conducted a study to decrease the co-efficient of variation and increase the reliability of DRI method. The crack classification and the corresponding weighing factors were modified. This has significantly increased the reproducibility of the test. This modified DRI method was used by Sanchez et al. (2015) to study concretes of varying compressive strengths consisting of various reactive aggregates from Canada. As per the paper the damage was classified into 3 branches: 1. Reduction of compression and tensile strength, 2. Decay of elastic properties and 3. Physical integrity loss of the material that can be linked to durability. The study showed promising results to quantify damage due to physical distress (type 3) and a good co-relation was obtained between DRI, physical distress and expansion. However, this method does not consider crack orientations, nor can it explain the reaction mechanism. The length and extent of the crack is only obtained indirectly. In spite of the shortcomings, DRI seems to be a promising tool to quantify cracks in damaged cores. It also seems to be a good input tool for numerical models.

Quantification by image analysis

Image analysis technique proves to be a more automated technique as compared to DRI. Unlike DRI which provides a good classification of relative damage, the image analysis techniques provide absolute damage. The method is faster and does not need a microscope.

The quantitative petrographic method for concrete using image analysis for ASR affected samples was introduced by Rivard et al. (2000). The technique requires preparation of polished sections with fluorescent epoxy impregnation. Under UV light all the cracks become prominent and easy to identify. Often the sample is treated with uranyl acetate so that the gel pockets are also illuminated. The image is then segmented using an image processing software by greyscale thresholding to obtain a binary skeletonized image of the crack. The technique provides quantitative data like length of cracks, crack densities as well as information over crack orientation. These are considered to be important parameters for ASR damage. However, this method fails to classify various types of cracks based on its origins. In contrast to DRI, this method is more automatic and reproducible. Based on similar principles, this method was simplified by Lindgård (2013). Instead of crack densities, percentage fraction of crack area to the original area was used. This method was performed from an extensive set of 60 different prisms from various locations across Europe as a part of the EU-PARTNER project. 16 fluorescent impregnated polished samples were observed under the ultra violet illumination. He was also able to correlate this crack intensity to the expansion in laboratory tested prism under RILEM's AAR-3 (fig 2.5).

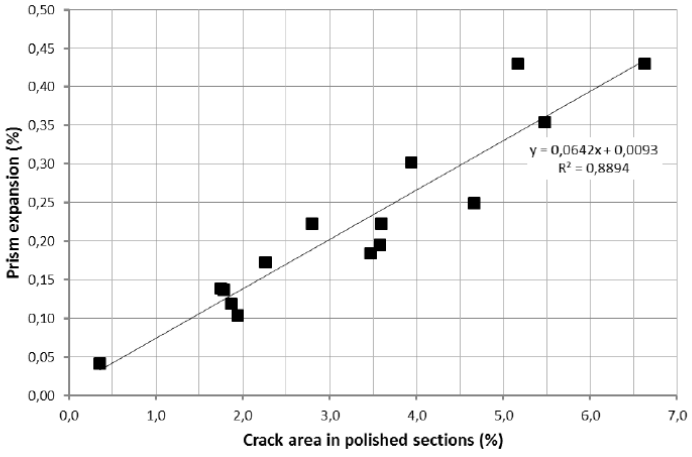

FIGURE 2.5: Total cracking intensity (%) plotted against expansions in 16 prisms (Lindgård, 2013)

.

In another study, Haha et al. (2007) tried to establish a quantitative relationship between ASR expansion and the degree of reaction using Scanning Electron Microscopy Image Analysis (SEM-IA). A well documented image segmentation protocol can be found in his study.

2.4.2 Laboratory tests

The DRI method still lacks to quantify damage pertaining to mechanical properties and other assessment methods are necessary to quantify these features. Yurtdas et al. (2013), Ahmed et al. (2003) through experimental research and Esposito et al. (2016) through a comparative study along with laboratory tests demonstrated the effect of ASR on mechanical properties. They concluded that ASR is sensitive towards the tensile strength and elastic modulus decay is a better assessment criterion. They also recommended that the assessment must not be based on the compressive strength of concrete as it can yield misleading results. Some researchers in the past have shown the dependence of different boundary conditions on strains developed due to ASR. Multon and Toutlemonde (2006) studied the effect of alkali silica expansion under restraints and axial loading on cylindrical specimens. He demonstrated that the total volumetric expansion remains the same. Under the influence of compressive stresses, " expansion transfer" takes place. This is explained as under the loading, the gel expands in the less compressed direction. The test also validated the effect of confinement on the radial directions and loading along the axial direction. The "expansion transfer" was proven to be a consistent result as long as the compressive stress developed by the restraint was lower than the applied compressive stress. Morenon et al. (2017) studied the effects of anisotropic gel expansion under the restraint from reinforcements. The study backed the "expansion transfer" concept. Moreover, the reinforcement imposed compressive stresses on concrete and consequently delayed cracking due to expansion.

Some petrographic limitations like predicting the future expansion potential of aggregates to some extent can be overcome by using chemical tests. A lot of research has been done over the years in developing reliable laboratory tests. The aim of the tests is to determine the reactivity of aggregates and set an acceptable limit to the gel expansion (Wigum, 2006). A review by Chatterji (2005) makes a comparison by different empirical and semi-empirical tests. The study is conducted on Danish aggregates and lists pitfalls and limitations of various tests. The ASTM C 289 test conducted at 80^0C in 1M NaOH for 24 hours is a purely empirical tests with acceptance limit from service record of tested aggregates. This is the most widely used chemical test but not suitable for all aggregate types. Other common laboratory tests include concrete prism test and mortar bar tests. These test simulate accelerated conditions with elevated alkalies and

higher ambient temperature (Swamy, 1992). The tests are reliable to a good extent to predict the maximum expansion. However there has been some criticism as these tests are very much influenced by test conditions. Often the elevated temperature and alkali results in unrealistic expansion values. Moreover, these tests take a long time in order of 6 months to 1 year to simulate a complete expansion. Some rapid tests like ultra accelerated mortar bar tests can provide results in 14 days. However,the reliability of this test is heavily controversial due to highly unrealistic laboratory conditions.(Swamy, 1992).

The current International ASR testing guidelines are laid down by The International Union of Laboratories and Experts in Construction Materials, Systems and Structures (RILEM) Nixon and Sims (2016). The guidelines included a collaboration of prominent laboratories and standards over the world and is considered to be the most reliable standardised testing till date. RILEM 219-ACS provides a flow chart as seen in fig 2.6. For performing petrographic analysis, RILEM also provides comprehensive atlas of the reactive minerals in aggregates. This serves as a complimentary tool to petrographic test AAR-1 (Fernandes et al., 2016).

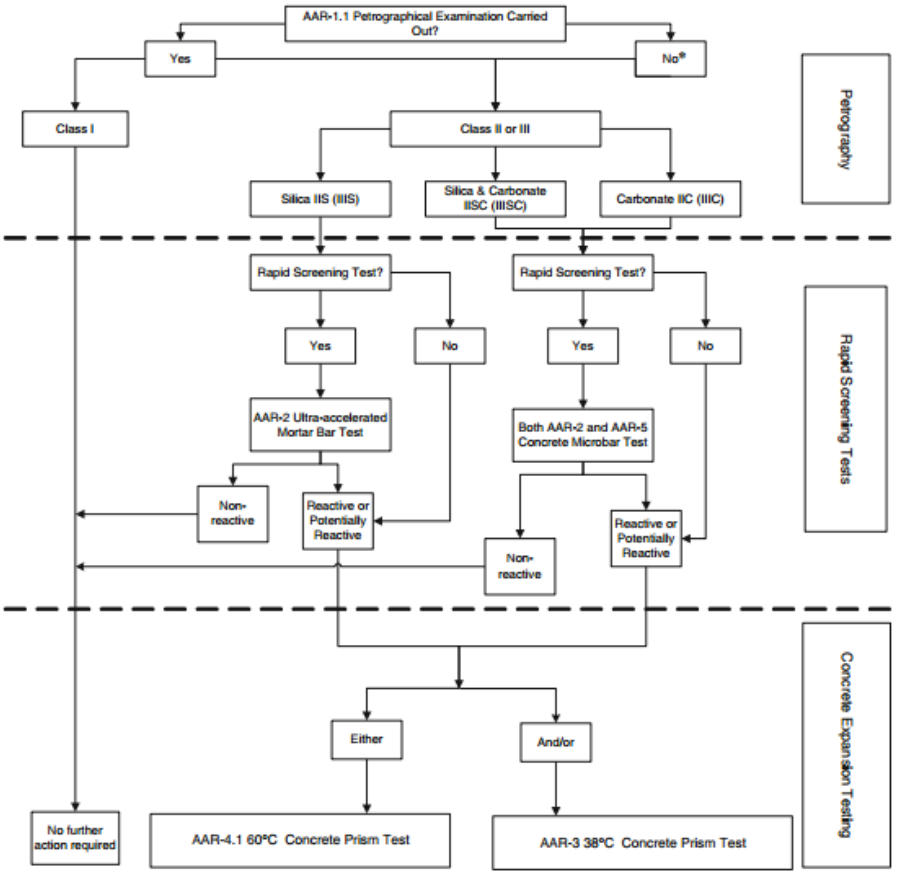

FIGURE 2.6: Flowchart as per RILEM's AAR-0 (Nixon and Sims, 2016)

AAR-0 provides the basic overview and a guide of the RILEM tests which is to be followed by AAR-1. AAR-1 is a petrographic investigation. The aggregates are divided in three classes based on the rock type and the size of the mineral grains:

1. Class I: Very unlikely to be alkali active
2. Class II: Potentially alkali reactive or alkali reactivity uncertain
3. Class III: Very likely to be alkali reactive.

Petrographers are also required to distinguish between silica phases and carbonate phases. This is followed by rapid screening tests. Subsequently, the AAR-4.1 or AAR-3 is carried out. Both the tests are concrete prism tests. AAR-3 is carried out at 38^0C and takes 12 months to yield result whereas, AAR-4.1 stored at 60^0C takes half the time i.e 15-20 weeks. RILEM has set a threshold expansion value for different tests. The tests exceeding the value are termed as potentially reactive.

2.5 Modelling of ASR

It has been already seen that even the most reliable RILEM tests take a long time to yield results. Storing the samples for such a long time is also expensive. The existing assessment methods are mostly qualitative and hence less reliable. Considering these factors and owing to improved computation power, the focus has shifted to numerical computational models. Some of these models have shown promises to be cheaper alternatives to the existing methods. Since 2000s various new models have been studied by researchers at different levels: From analysing the micro level, intermediate meso-scale to the damage response at a structural level. Structural model developed by Saouma and Perotti (2006) is a thermo-chemo-mechanical model based on gel expansion. The model uses temperature expansion as imposed strains. It demonstrates coupling of internal swelling of material with the stress state. Capra and Sellier (2003) also at the structural level provides a probabilistic model to consider orthotropic expansion coupled under moisture and temperature effects. The probabilistic model considers spatial distribution of reaction sites. Due to advancement in microscopy, computational models at lower scales have been possible. At meso-level, the heterogeneity of concrete is considered. Bažant et al. (2000) adopted a linear elastic fracture mechanics approach at meso-level. The model makes use of a periodic cubic cell as aggregate embedded in mortar. The gel pressure developed due to ASR expansion is considered as internal loading. The model was primarily used to demonstrate the pessimum effect of aggregates and does not comment on mechanical properties like compressive strength and tensile strength.

The model by Comby-Peyrot et al. (2009) is a 3D FEM meso-level model where aggregates are embedded randomly in mortar using particle size distribution and the effect of inter-facial transmission zone (ITZ) was not considered. A chemo-mechanical constitutive model was used to assign isotropic dilation as internal load. The model was able to simulate crack patters and loss in stiffness to a good accuracy. Schlangen and van Breugel (2005) adopted the already developed linear elastic lattice model Schlangen and van Mier (1992) to predict tensile strength reduction in concrete. The same model was later used by Çopuroğlu and Schlangen (2007) to simulate realistic crack patterns on a 2D model and by Schlangen and Çopuroğlu (2010) on a 3D model. This model takes into account the mechanical consequences of the ASR reaction without considering the physio-chemical coupling. They used internal expansions at potentially reactive sites based on petrographic analysis. The model made use of digital photo-micrographs and CT scanning to recreate the micro structure in the model. However, this model represents a small model of one aggregate. As a part of PAT-ASR project, (Anaç, 2016) tried to validate the results with experimental data under the effect of free expansions. His aim was to find a quantifiable parameter to correlate experimental data with model simulations.

A simplistic numerical model to estimate an expansion-time relationship has been developed by Karthik et al. (2016). The advantage of this model is that it considers only a few parameters to get a realistic expansion curve. The model was validated in a lab at a beam level as well as at a specimen level by conducting accelerated tests. However, this model has not been tested at a real time scale yet. the model requires some empirical inputs. This model seems to be a promising model to combine with the lattice model to estimate an expansion-time relationship.

2.6 Overview of Afsluitdjik

The Afsluitdijk is a 32.5 km dam built in 1932 as a flood barrier. The dam is located in the northern part of the Netherlands and connects the province of Noord-Holland and Friesland. Apart from being a flood-defence barrier, the dam also functions as a motor-causeway (A7/E22). Most of the dam is made using boulder clay dredged from the floor of Zuiderzee. The dam consists of 2 main sluice complexes for the discharge of water from Ijsselmeer into the Wadenzee and 2 lock complexes for transport of ships both along the north and the south part of the Afsluitdijk. The sluice in the south along Den Oever named as ‘Steven Sluice’ consists of 3 sluice sub-complexes where as the sluice in the north along Kornwerdezand named as ‘Lorrentz sluice’ consists of 2 sluice sub-complexes. The Sluice and lock complexes are built in reinforced concrete.

In 2008, a study of the residual lifetime of the concrete elements in the Afsluitdijk was conducted by the Rijkswaterstaat (Ministry of Infrastracture and Environment). The sub-report 05 dealt with the alkali silica reaction as their primary damage hypothesis. The report confirms the use of reactive aggregates in the foundation and further states that the foundation of the Lorrentz sluice at Kornwerdezand to be the most affected concrete element. The report recommends that although the probablity of ASR propagation is small, the possibility of ASR damage should not be ruled out. Additional investigation must be performed to predict the damage (Boutz et al., 2008).

Chapter 3

Materials Characterisation

This chapter covers a broad characterisation of the existing specimens of the structure at a material level. A brief description of the structure and the cores is also included in the chapter. The test setup and the test analysis are described in detail. The characterisation focuses on concrete composition, investigation of original mix design, type of cement and aggregates used. The tests help to identify potentially reactive sites that encourage alkali silica reaction. The existing crack patterns and the crack densities are studied and an attempt is made to quantify the damage using image analysis and petrographic techniques.

The data obtained from material characterisation is used as input parameters for the simulation of the lattice model and are discussed in Chapter 4.

3.1 Description of structure

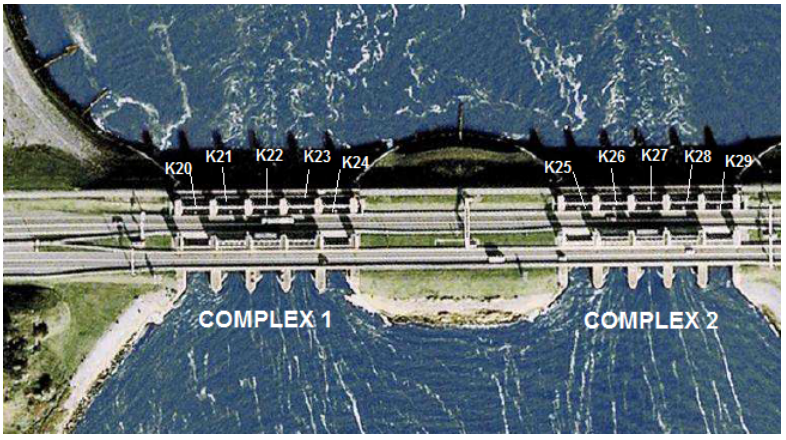

FIGURE 3.1: Aerial view of Lorrentz sluice, Kornwerderzand (Borsje and Zwarthoed, 2008)

The study focuses on a part of the Afsluitdijk that is the Lorrentz sluice complex at Kornwerderzand in the north of the Afsluitdijk. The sluice complex is divided further into to 2 sub-complexes as shown in fig 3.1. Each sub-complex is further divided into 5 gates. Each gate is labelled successively from K20 to K29.

The sluice sub-complex can be discretized in simple structural elements. Fig 3.2 shows how they are distinguished. The foundation slab of the sluice supports 4 pillars and 2 buttress-walls on the edge (fig 3.3). All the pillars support the bridge decks which is a part of the A7 highway and carries traffic. There are 3 bridge decks in total. 2 Bridge decks for automobile traffic and one deck reserved for bicycles. Apart from that, the pillars also support the lift towers. The sluice gates are in between the pillars and the wing walls. A detailed description is provided by (Borsje and Zwarthoed, 2008).

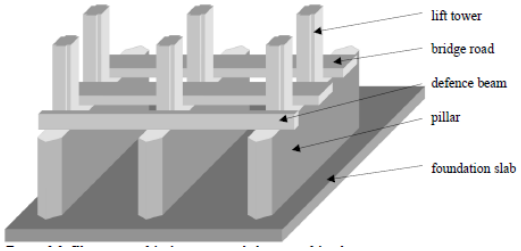

FIGURE 3.2: Structural elements in a sub-complex (Borsje and Zwarthoed, 2008)

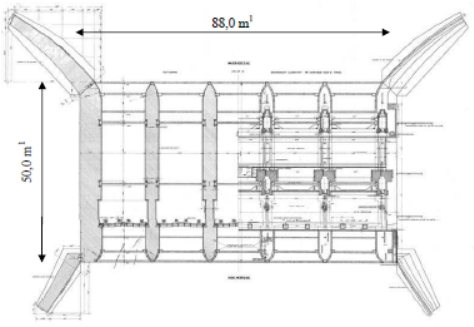

FIGURE 3.3: Plan view of the complex with different elements (Borsje and Zwarthoed, 2008)

3.1.1 Foundation slab

Based on the recommendations of (Borsje and Swinkels, 2016), the foundation slab was chosen for the study of ASR. The foundation slab of the Kornwerderzand sluice is 88m×50m in dimensions and 1.3m thick. The slab is made of reinforced concrete and the top surface of the slab is covered by a 25-40 cm brick wall topping. The foundation slab is supported on timber piles. The layout and configuration of the piles is shown in fig 3.4.

3.2 Description of the concrete cores

The concrete cores were drilled and supplied by SGS Intron. They were drilled at various locations. The cores described in this chapter concern with the ones drilled from the foundation slab of Kornwerderzand as described in fig 3.1. These were drilled at each

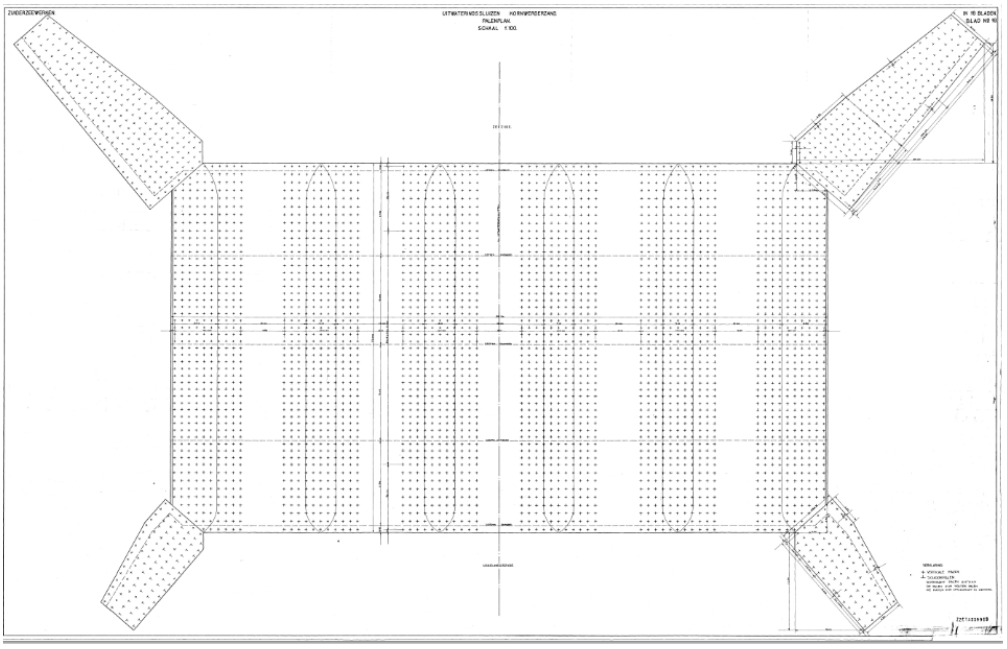

FIGURE 3.4: Pile configuration, Kornwerderzand (Borsje and Zwarthoed, 2008)

gate at 4 locations. These locations are indicated in fig 3.5. Thus a core located at gate 22 in Kornwerderzand foundation slab along section 14 was labelled as K22-14.

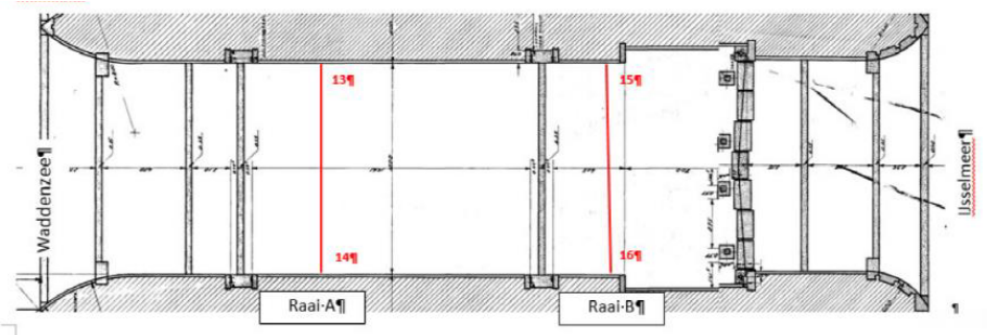

FIGURE 3.5: Boring Locations for each gate in the foundation slab.

The available cores were investigated thoroughly via visual examination and 6 cores at different locations were chosen for petrographic analysis. It was observed that cores tagged K22-16, K23-14 showed typical signs of ASR i.e presence of white deposits which could possibly be ASR gel, intense micro-cracking and cracks propagating through aggregates. Other samples include K26-14, K27-16, K23-13 and K23-15 which showed some ASR signs. These samples were also chosen to avoid sampling bias and get an idea over different sections of the foundations.

The cores were drilled perpendicular to the top surface of the foundation slab and over the depth of the section. Each core was 100 mm in diameter with lengths varying between 500 mm to 1200 mm. The first 250 mm to 400mm of the core was covered with

brick masonry followed by reinforced concrete. The top part of the concrete in the core showed presence of steel reinforcement in both directions with a diameter of 20mm and 45mm. All the cores showed a lot of micro cracks running through the aggregates over the depth of the section. The cracks were mostly parallel to the reinforcement. However, there was no presence of major cracking.

The cores were placed in water and then dried at room temperature to reveal the surface cracks. These cracks were later marked with a help of a blue marker pen (Borsje and Swinkels, 2016).

FIGURE 3.6: Example of a concrete core. Tag Number K23-13. The micro-cracks observed in the visual expansion are marked in blue. The left hand side surface indicates the brick masonry layer on the top.

3.3 Sample preparation

Sample preparation techniques directly affect the final results. A protocol was followed to ensure a smooth sample preparation devoid of irregularities. This section talks about in-detail preparation of polished and thin sections used for microscopy investigation.

3.3.1 Preliminary measures

Petrographic studies included image analysis of polished concrete sections. The cylindrical concrete cores were cut to suitable dimensions to perform petrographic studies. The concrete cores consisting of ASR damage possess existing cracking patters. During the cutting process, these cores are subjected to mechanical loads introduced by the

sawing action which can disrupt the existing cracks and cracking patterns. Hence, some precautionary measures were followed before they were cut to the required dimensions.

Epoxy Impregnation

The impregnation of cores with low viscosity epoxy served to be a good preventive measure to preserve the integrity of the structure and protect the micro-structure from damage against mechanical sawing. The concrete cores were divided into lengths of 10 cm each and labelled serially top to bottom. This was done to fit the cores in the vacuum impregnating device. The aim was to achieve impregnation only on the surface of the cores where epoxy acts as an adhesive agent to hold the cracks together.

Each 10cm concrete cylinder used for impregnation was first tightly packed in a thick plastic bag. A plastic tube was attached to the samples inside the plastic bag. This served as an inlet for the epoxy to enter the bag. The plastic bag was then placed in a vacuum impregnating device as shown in fig 3.7.

(a) (b)

FIGURE 3.7: Impregnation process: (a) Vaccuum Impregnator (b) Sample after preliminary impregnation

1 part of epoxy was mixed with 1% w/w of fluorescent epodye. The fluorescent dye was essential for polished section analysis under UV light. This epoxy was further mixed with a hardener. Every 1800 g of epoxy was mixed with 540 g of hardener. The effect

of the 1% dye was also taken into account. Thus, a conversion factor was reached in the following way:

$$Required\ Hardener(g) = \frac{540}{1800} \times [0.99 * Epoxy(g)]$$

120 g of epoxy was found to be sufficient for impregnation of each sample.

The samples were impregnated for at least 15 minutes under vacuum to achieve a uniform surface and get rid of air voids. Epoxy resin when mixed with the hardener, results in an exothermic reaction and generates a lot of heat. To avoid this, the samples were placed in cold water for 24 hours until all the epoxy hardened completely.

3.3.2 Polished sections

Polished sections were necessary to perform point counting, image analysis and perform the Damage Rating Index (DRI) test. The sections were observed under a stereo microscope with a normal halogen light as well as with the help of Ultra Violet (UV) light. The scans of the polished section also serve as an input for the micro-structure in the lattice model. The mesh generated in the lattice model depends on the scanned image of the micro-structure as well as the image resolution.

The samples obtained after preliminary impregnation as shown in fig 3.7 was cut over the depth. It was essential to ensure that the saw cut is smooth and exactly parallel with minimal surface irregularities. Minor unevenness was corrected in the polishing stage. The final size of the sample was around 70×100 mm. The sample was later subjected to a secondary epoxy impregnation. The protocol laid down by (Jakobsen et al., 2000) was followed for the impregnation. This resulted in an impregnation up to 10 mm of the sample surface and the cracks, air voids on the sample surface were completely filled with the fluorescent epoxy. The epoxy was let to harden another 48 hours under its own weight.

The next step involved removal of excess epoxy over the surface such that only the epoxy was visible in the cracks and the air voids. This was achieved using a lap table grinding machine. A silicon carbide (SiC) grinding paper of grade FEPA 120 (125 μm) resulted in an acceptable surface evenness for stereo microscopy and a complete removal of excess epoxy on the surface. The surface was checked once again under UV light to check if any excess epoxy was still present. Otherwise the grinding step was repeated again. A visual description of the list of steps to achieve the polished section are described in fig 3.8.

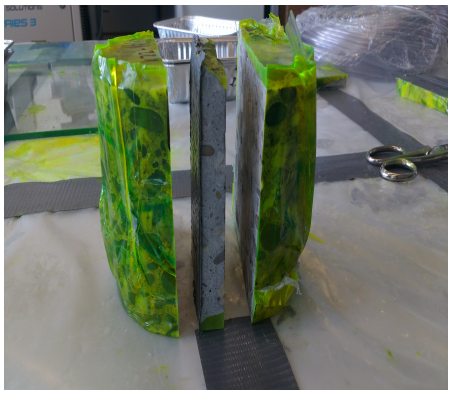

(a) sample sawn over its depth

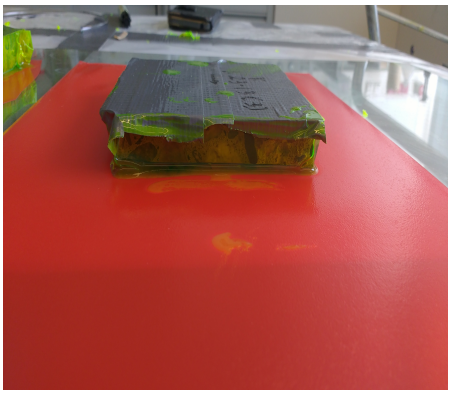

(b) Sample after secondary epoxy impregnation. Let to harden under its own weight.

(c) Grinding on a lap table using SiC paper

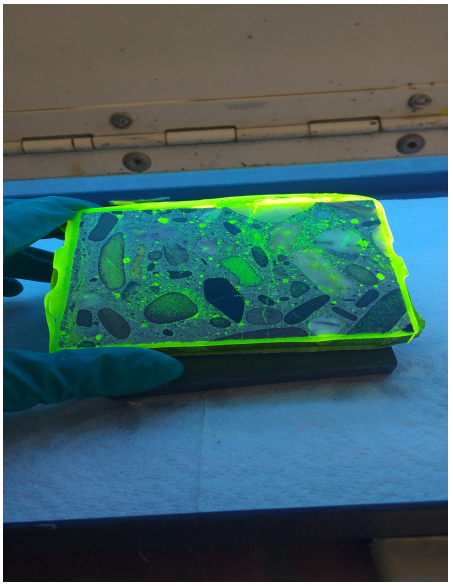

(d) Checking under the UV light for excess epoxy

(e) Final Specimen.

FIGURE 3.8: Grinding and polishing

3.3.3 Thin Sections

One of the objectives of the project was to confirm the presence of ASR. Thin section analysis proved to be a good tool to qualitatively confirm the symptoms of ASR. The typical signs of ASR were observed with the help of a compound microscope. Moreover, thin sections were also used to evaluate the mix design and the paste-aggregate ratio. Point counting was used to determine the fraction of fine aggregates and air voids present in the mortar. Mineral structure of coarse aggregates was observed and type of aggregates was determined using polarised light microscopy on thin sections.

A thin section is defined as a section with a thickness of 30 μm. The size of the thin sections used in this project was 30 $\times$ 45 mm based on the size of the reference glass. A detailed protocol for preparation of thin section has been laid down by Jakobsen et al. (2000). A similar protocol was followed in achieving uniform thin sections of approximately 30 μm thickness. A total of 8 thin sections were prepared from the same cores which were used to make polished sections. The sampling was done randomly to avoid sample bias. Each sample of 30 $\times$ 45 mm and around 20 mm in thickness was cut out from the respective impregnated concrete cores. The reference glass was glued on one side with the help of 2 part epoxy glue (plastic padding).

The entire sample preparation was carried out on an automatic thin section machine. The preparation was carried out in 2 parts. In the first part, the sample obtained after gluing the glass was then cut to a thickness of 10.5 mm using a diamond blade. A vacuum holder kept the sample in place and consequently, a uniform parallel cut was achieved. The surface needs to be as straight as possible, which was achieved using three grinding rollers from coarse to the finest grade. The sample was then impregnated with epoxy in the same way as explained in section 3.3.1.

In the second step, the excess epoxy was removed such that the thickness of the sample was back to approximately 10.5mm. This was done again using the same grinders. The obtained surface was then glued to the object glass using a UV-hardening glue. This can be considered to be one of the most critical steps in the sample preparation. One has to make sure that the glue is spread evenly. Any irregularity affects the quality of the end product. The sample, which now looked like a sandwich between the object and the reference glass was cut using the diamond blade. This time the Vacuum holder held the object glass. A thickness of approximately 1 mm or less was achieved. This was again ground using the 3 rollers in a sequential order from coarse to fine. These rollers can grind approximately 500 μm, $100 - 120$ μm and $50 - 60$ μm respectively. Finally a 30 μm thin section was obtained. The thickness was confirmed under cross

polarised light (XPL) by checking the bi-refringence of quartz grains. As per the Michel-Levy chart, quartz grains exhibit white colour at a thickness of $30\mu m$. Finally, a cover glass was glued on the surface to protect it from abrasion and environmental effects like carbonation using a transparent UV-hardening glue.

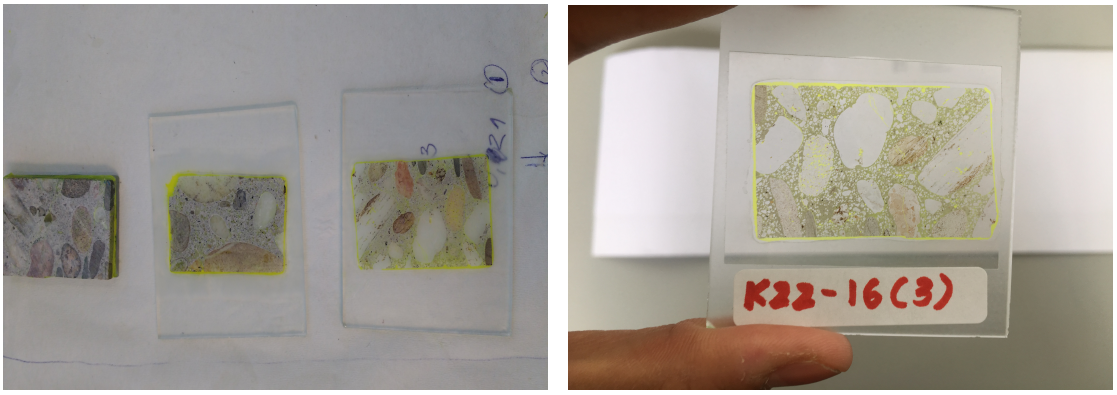

(a) (b)

FIGURE 3.9: (a) Thin sections at different grinding steps. (b) A $30\mu m$ thin section.

3.4 Quantitative micro-structural analyses

3.4.1 Quantification of coarse aggregates

The prepared polished sections were scanned using an Epson V800 photo scanner. The image resolution was set at 3175 dpi (125 pixels/mm). The method used to analyse is the 'point counting method' as described in ASTM C457. However, the method applied in this study made use of a scanned image instead of a stereo microscope. This made counting easier and human errors were minimised.

Point counting was performed using a JAVA based open source image analysing software 'ImageJ (Fiji)'. A grid of $16mm^2$ was superimposed on the image. An assumption was made that area of a coarse aggregate was $16mm^2$ as seen in fig 3.10. The points that fell on coarse aggregate were counted using a cell-counter tool within the software. The accuracy and reliability of the results depend upon the number of points that were counted and the area fraction of the component. A statistical relation is provided by (Poole and Sims, 2015, p23). In the current study, on an average 440 counts were considered per sample. The resulting error of the volumetric proportion was between 8-12 %. A detailed calculation of the point counts is provided in appendix A. The results of 12 polished sections is presented in fig 3.11.

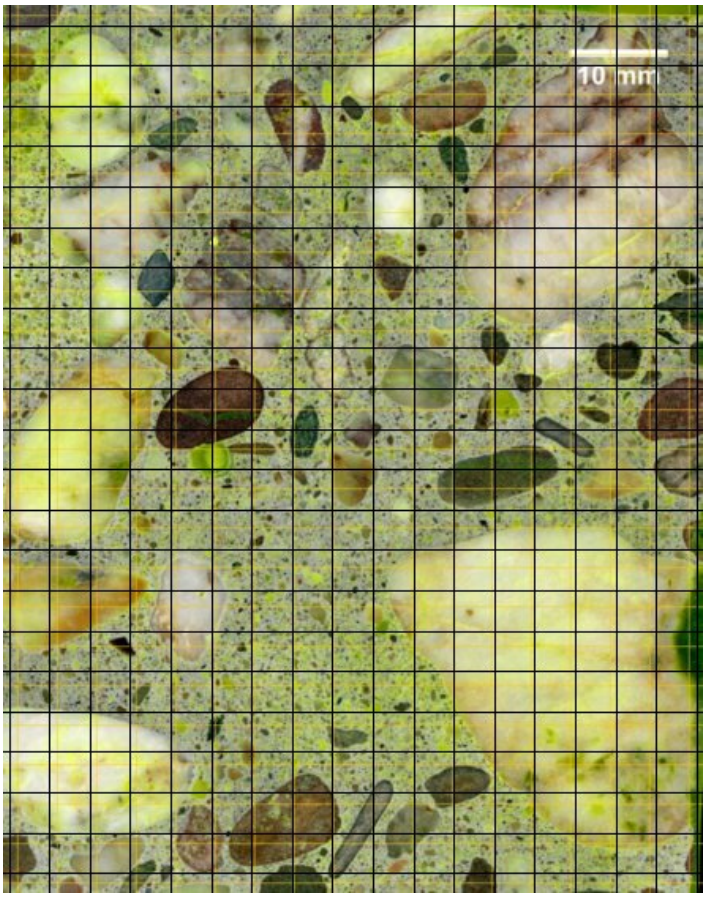

FIGURE 3.10: Example of grid overlay used for point counting in imageJ. The presented sample is K23-13(2). Note: image resolution has been scaled down in the report.

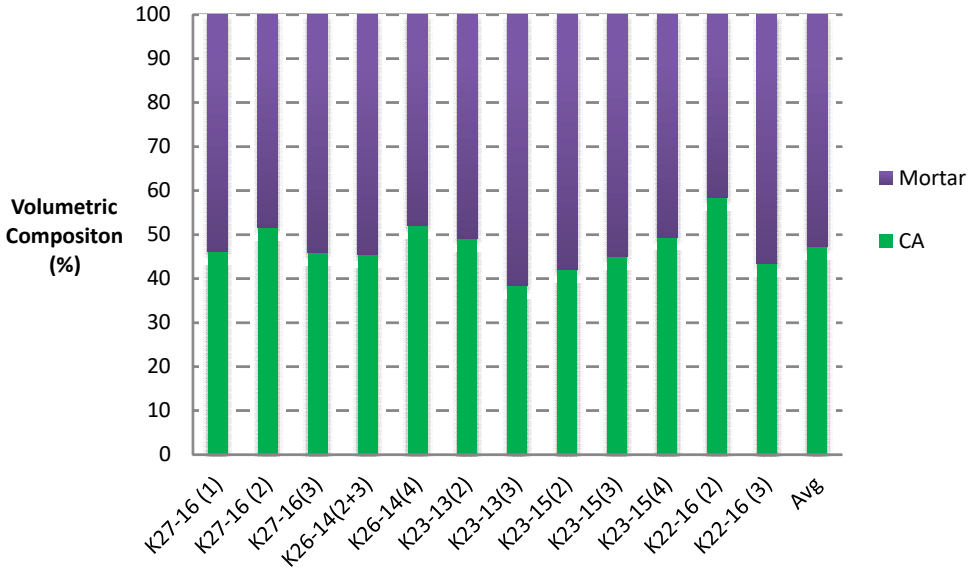

FIGURE 3.11: Volumetric proportion of coarse aggregates (CA) using point counting technique

3.4.2 Detailed quantification of mortar phase

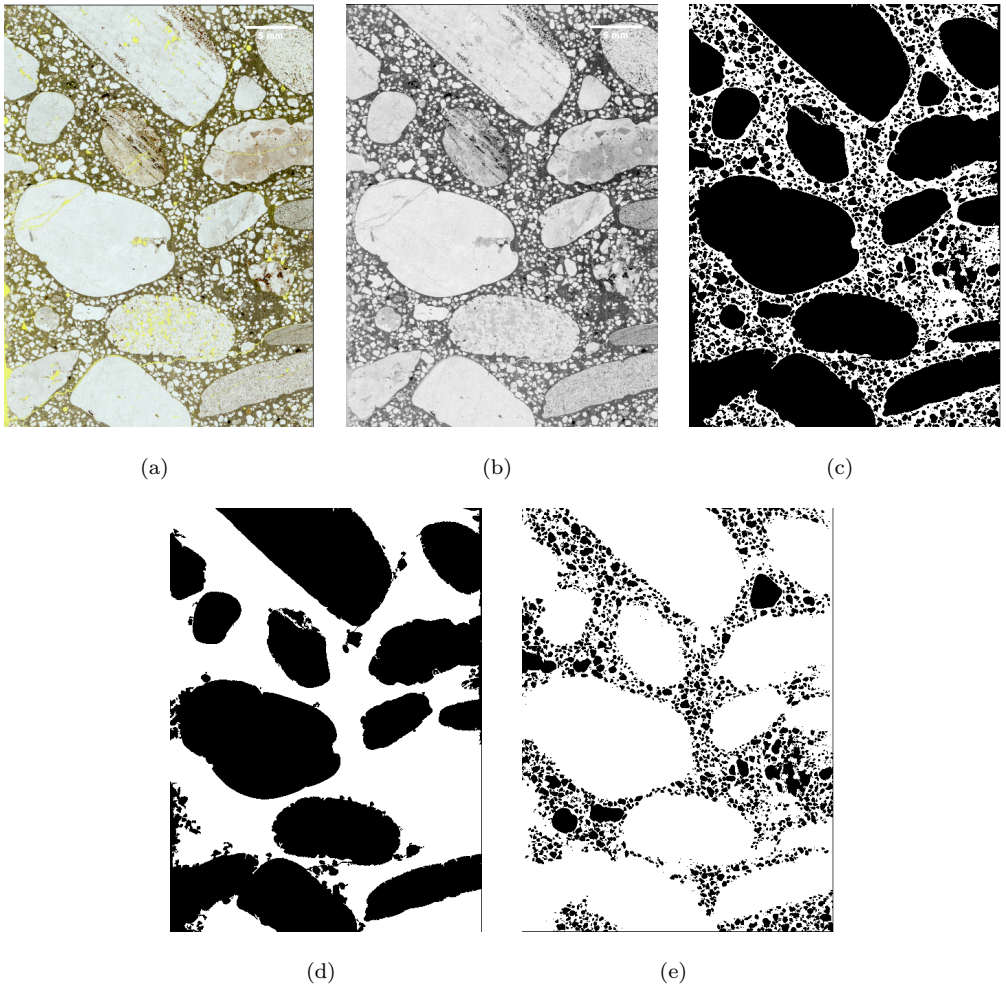

(a) (b) (c)

(d) (e)

FIGURE 3.12: K22-16(3): (a) Original PPL image in RGB. (b) 8 bit grey scale image. (c) final segmented binary image. (d) Size segmentation: coarse aggregates (e) Size segmentation: fine aggregates

Point counting technique for quantification of fine aggregates proved to be tedious and inaccurate. The main problem was because of the size of fine aggregates being less than 4mm. This required a finer grid and subsequently higher number of points to increase the probability of the points hitting the finer aggregates. Moreover, the thin sections resulted in an uniform colour of the fine aggregates which was distinct from the colour of the paste. This made thresholding and segmenting of the image easier based on the 8 bit grey colour range. Image analysis proved to be an effective method in quantifying fine aggregates, air voids and the paste on the plane polarised thin sections. This analysis provided a detailed composition of the mortar. Different image segmentation techniques were used to segment coarse aggregates, fine aggregates, paste and the air voids. Image segmentation protocols are presented in appendix B and the data pertaining to the

analysis can be found in appendix A. The example of a segmented image is presented in fig 3.12.

In total 8 sections were prepared. However, quantitative analysis was performed on 6 samples depending on the quality of the finished thin sections. Volumetric composition of samples in the thin sections was determined as seen in appendix A. This was combined with the point counting analysis of coarse aggregates. The results of these six samples are presented in fig 3.13. It is assumed that these 6 samples are representative of the concrete in question. This data is further used to estimate the original mix design of the concrete using micro-structural analysis. Moreover, with this analysis, the paste-aggregate ratio was also determined. It is presented in fig 3.14.

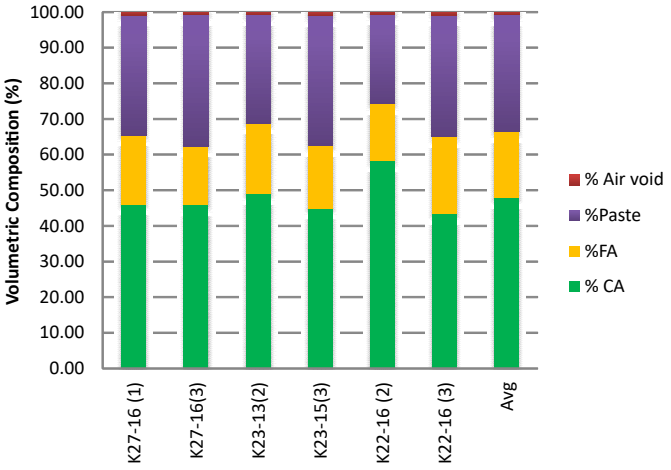

FIGURE 3.13: Complete volumetric composition of concrete cores

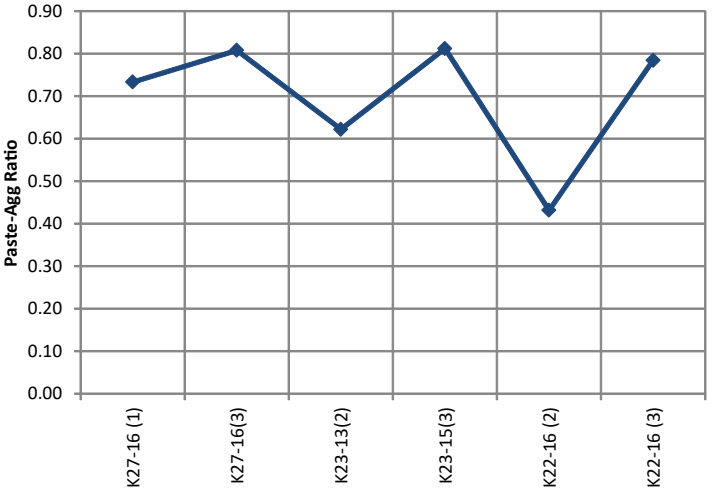

FIGURE 3.14: Estimated Paste-Aggregate volume ratio

3.5 Polarised light microscopy

Polarised light microscopy (PLM) was performed on thin section using plane polarised light and crossed polarised by means of a cross polarisation filter. PLM serves to provide a qualitative to semi-quantitative description of various micro-structural features.

3.5.1 Type of cement

Blended cements with ground granulated blast furnace slag (GGBFS) is the most common type of cement used in the Dutch building industry. The composition of GGBFS in the cement typically ranges from 36 to 95 percentage by weight as per European standards (Neville, 2011, p79). However, the structure being 80-90 years old, the possibility of using blended cements was lower. An attempt was made petrographically to identify the cement type by analysing the composition of the cement matrix. The hydration reaction of cement resulting in the formation of the matrix with ordinary Portland cement (OPC) (the most basic cement type) is idealised in the following way (Neville, 2011, p15).

$$2C_3S + 6H \rightarrow C_3S_2H3 + 3Ca(OH)_2$$
$$2C_2S + 4H \rightarrow C_3S_2H3 + Ca(OH)_2$$

However in case of GGBFS cement, the additional pozzolanic reaction takes place which consumes the Portlandite ($Ca(OH)_2$) from the above reaction to form calcium silicate hydrates ($C-S-H$) in common words the matrix. This reaction proceeds slowly in time. The reaction is idealised in the following way:

$$GGBFS + Ca(OH)_2 \rightarrow C_xS_yH_z$$

It can be assumed considering the age of the structure that the hydration of cement is nearly complete. This would imply that in presence of GGBFS, most of the Portlandite must have been utilised and hence should not visible in the obtained thin-section micrographs. The thin sections were analysed under PPL and XPL. The thin sections showed only a few grains of unhydrated cement. The cement grain can be assumed to represent ordinary Portland cement. Additional electron microscopy analysis (SEM) will be necessary to determine the chemical composition of the unhydrated clinker. Some presence of volcanic glass fragments were observed (fig 3.15(a)). They can be associated with volcanic trass which was used as a pozzolanic material in the Netherlands in the last century. No traces of GGBFS were observed in any of the thin sections. Moreover, high amount of Portlandite can be observed as a yellowish birefringent light (fig 3.15(b)).

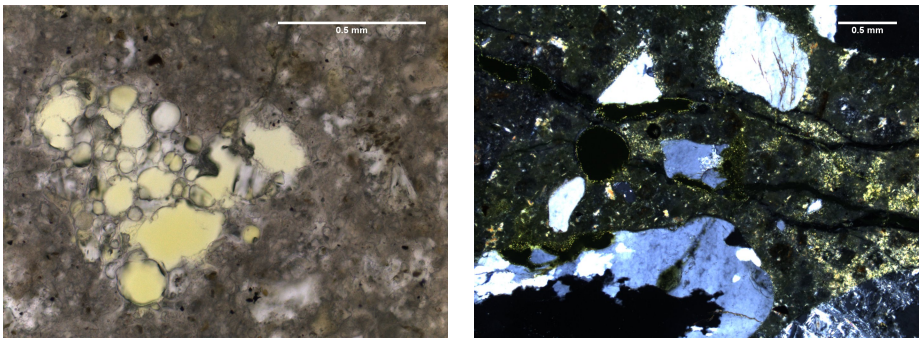

(a) (b)

FIGURE 3.15: (a) K27-16(3)(PPL): traces of Volcanic trass (100x magnification). (b)(XPL) Birefringent yellowish Portlandite observed in the matrix (40x maginfication)

Circular polarisation technique by Çopuroğlu (2016) emphasised the location of the excess Portlandite which is developed as a by-product of the OPC hydration. Knowing the birefringence value (Difference of refractive indices) of Portlandite to be 0.27 and the thickness of the thin section to be 30 μm, the presence of Portlandite was confirmed in fig 3.16. The image shows well distributed Portlandite all over the specimen. Additional micrographs are presented in appendix E.

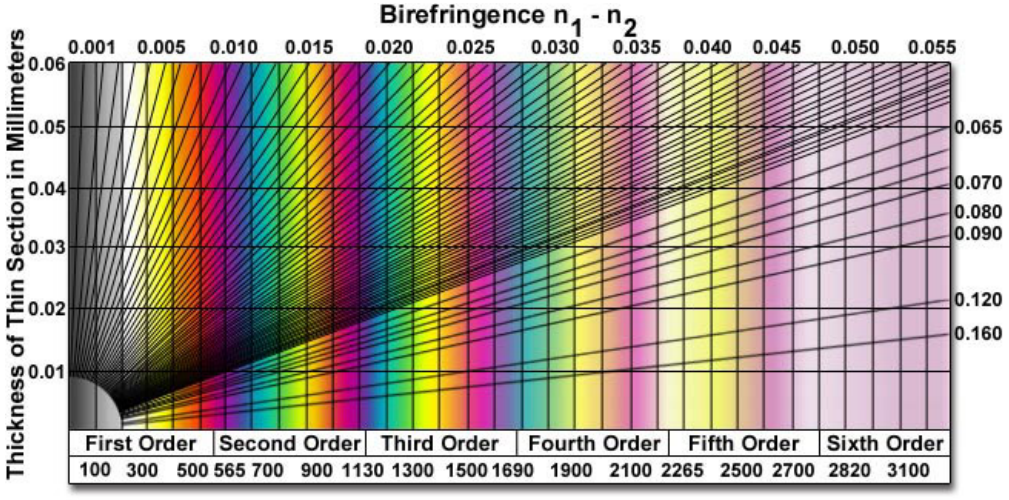

FIGURE 3.16: Michel-Levy interference chart for XPL microscopy

3.5.2 Type of aggregates

The Rilem petrographic atlas developed by Fernandes et al. (2016) along with the micrographs obtained from thin sections under PPL and XPL were used to evaluate the type of aggregates and their reactivity potential petrographically.

The most common recorded potentially reactive aggregates in Netherlands are quartzite, sandstone and porous chert. (Broekmans, 2002). Most of the aggregates obtained found in the thin section images were quartz based aggregates exhibiting different grain sizes under XPL. Most of the rocks belonged to the sedimentary type. The reactivity of the aggregates is linked to the grain size of the quartz particles as well as the type of rock minerals. The reactivity classification based on both rock type and the size of individual mineral grains has been proposed by Wigum (2006). It states that grain sizes $> 130\ \mu m$ can be considered to be innocuous whereas those $< 60\ \mu m$ can be considered to be highly reactive. A very high variation of grain sizes was observed in the same specimen

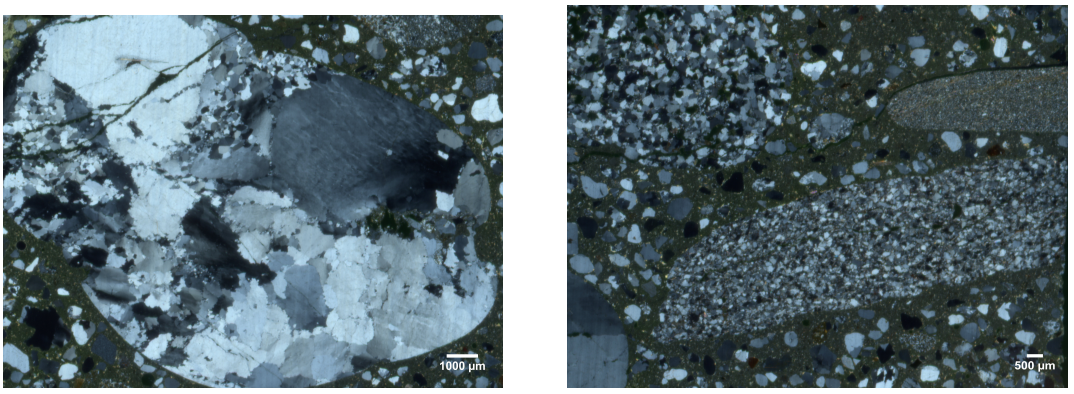

(a) Coarse grained Sandstone: Exhibiting grain sizes $> 130\mu m$

(b) Sandstone aggregates with different grain sizes under XPL

FIGURE 3.17: Variation of aggregate grain sizes

when observed under XPL as seen in fig 3.17. This implies that each aggregate behaves differently owing to different reactivity. Moreover, fig 3.17 (a) shows variation of grain sizes within the same aggregate. Most of the part of the aggregate can be considered to be innocuous in nature because of its high grain size. However, one can see that the grains are not distributed uniformly with some finer grains present in between the coarser grains. Since the grains sizes are considerably higher than the threshold value, this aggregate can be classified as a non reactive aggregate. The aggregates in fig 3.17 (b) can all be seen to be potentially reactive because of very small grain size. A higher magnification is necessary to determine the grain size of the specimen which is covered in the subsequent section.

Sandstone

Sandstone was the most common type of aggregate found in the 6 thin sections observed under both PPL and XPL. The RILEM petrography atlas (Fernandes et al., 2016) was used to identify microstructural features of the aggregates. The images have a field of view of 1.5mm along the width.

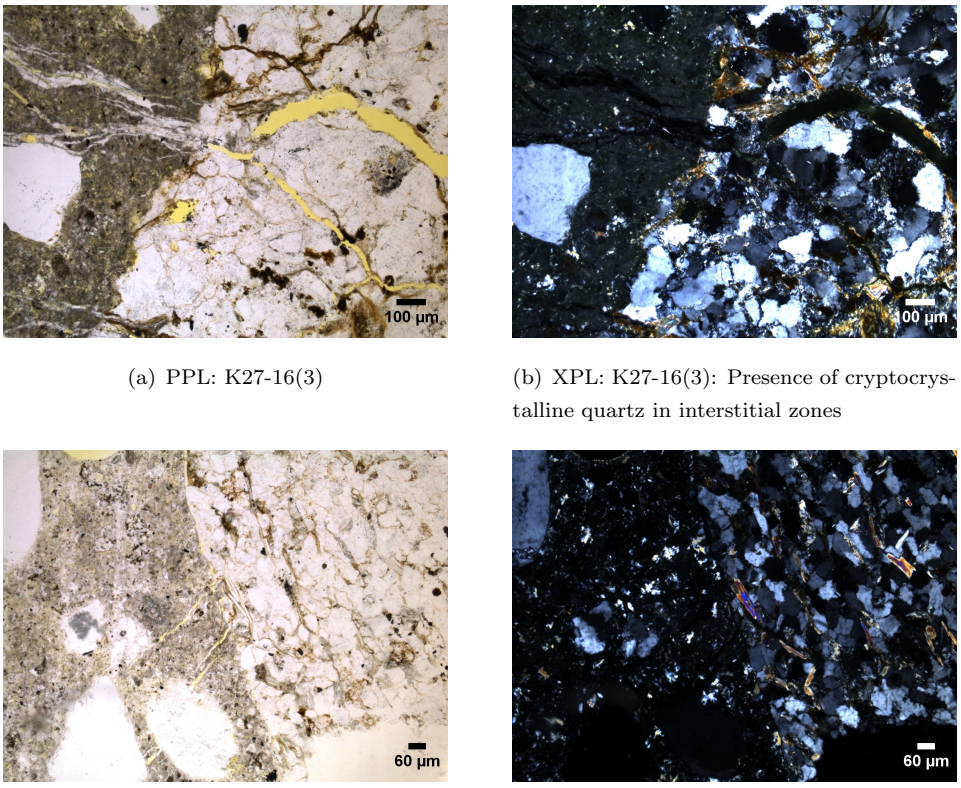

(a) PPL: K27-16(3)

(b) XPL: K27-16(3): Presence of cryptocrystalline quartz in interstitial zones

(c) PPL:K23-15(2): Well sorted quartz

(d) XPL:K23-15(2): Grain size 60 μm

FIGURE 3.18: Microstructural features of sandstone-I

Fig 3.18 (a) and (b) presents a coarse sandstone aggregate. The grains are poorly sorted giving rise to big interstitial zones. It can be seen that the interstitial zones contain presence of cryptocrystalline quartz grains < 10 μm. The potential reactivity of this aggregate could be attributed to presence of this cryptocrystalline quartz and thus classifying the aggregate as reactive. Fig 3.18 (c) and (d) present a medium coarse well sorted sandstone aggregate. The average grain size as seen in the picture is of order 60 μm *to* 130 μm classifying this aggregate as ambiguous.The interstitial zones are smaller as compared to (a) and (b), nonetheless contain poorly disordered micro to cryptocrystalline quartz grains. Some traces of sheet silicates can be observed in both the XPL images.

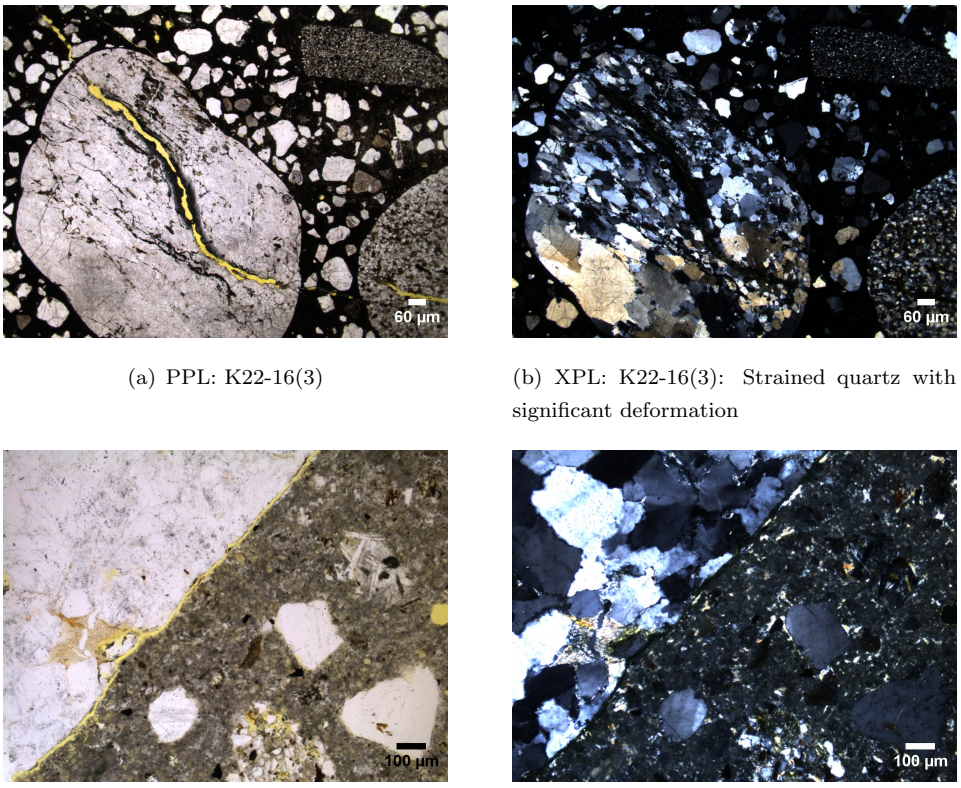

(a) PPL: K22-16(3)

(b) XPL: K22-16(3): Strained quartz with significant deformation

(c) PPL:K27-16(1): Non-reactive aggregate

(d) XPL:K27-16(1): Non-reactive coarse quartz grains

FIGURE 3.19: Microstructural features of sandstone-II

Fig 3.19 (a) and (b) are indicative of deformed state of quartz. Strained quartz has been linked as a potentially deleterious component by various researchers (Swamy, 1992). The strained zone creates wider interstitial boundaries which present a conducive environment for the reaction to proceed. In the same figure, the other coarse aggregate can be also classified as highly reactive. They are entirely made of reactive microcrystalline quartz 10 μm *to* 60 μm. On the contrary, Fig 3.19 (c) and (d) represent a coarse-grained sandstone with well sorted grains. The interstitial zones don't indicate presence of micro-crystalline quartz. This aggregate is therefore classified as innocuous.

Chert

Another common type of sedimentary rock observed in the thin sections was chert. The reactivity of chert can be attributed to very small size of grains. Most of them being cryptocrystalline in nature. The images have a field of view of 1.5 mm along the width.

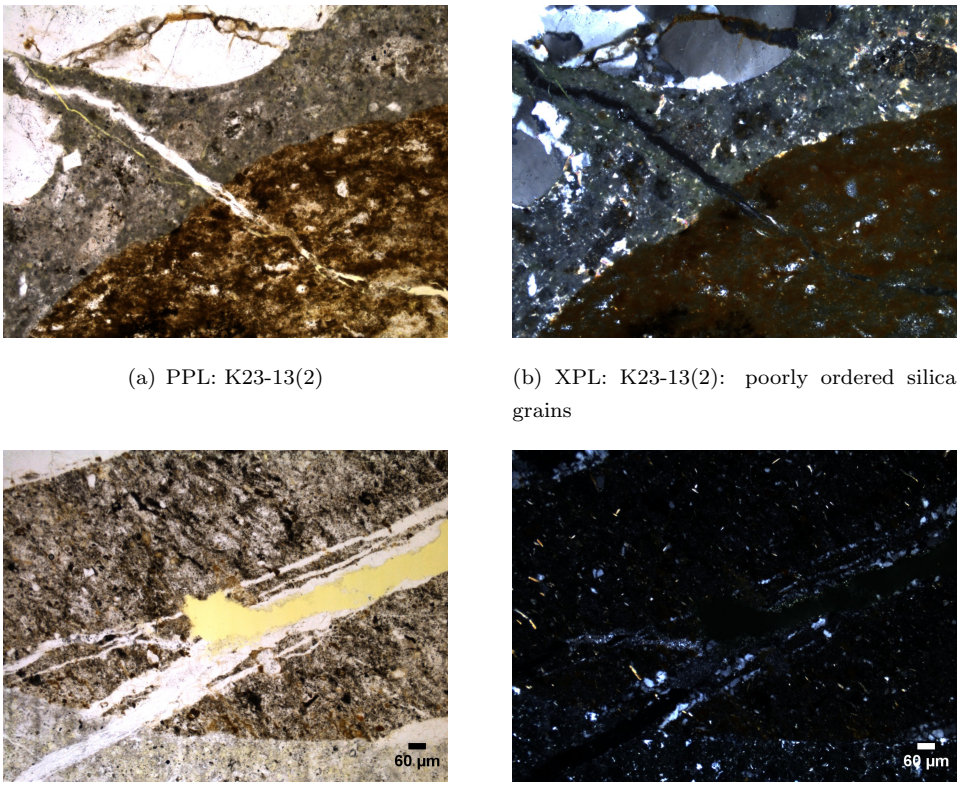

(a) PPL: K23-13(2)

(b) XPL: K23-13(2): poorly ordered silica grains

(c) PPL:K23-15(2)

(d) XPL:K23-15(2): cryptocrystalline nature

FIGURE 3.20: Microstructural features of chert-II

The chert aggregates can be considered to be highly reactive. The individual grain size of the minerals as seen in fig 3.20 (a) and (b) is so small that it is difficult to distinguish if the phase is crystalline or amorphous. In fig 3.20 (c) and (d) the grain size is of cryptocrystalline nature ($< 10\ \mu m$). (Broekmans, 2002) considers chert as the most important mineral associated with ASR reactivity in the Netherlands. The ASR reactivity in the Afsluitdijk can be attributed to these aggregates to owing to their presence in abundance in the thin sections. As per (Wigum, 2006) classification index, they can be classified as highly reactive sedimentary rocks.

3.5.3 Estimation of w/c ratio

The methodology adopted by Jakobsen et al. (2000) was used to estimate the water-cement ratio using UV light microscopy on thin sections. Three reference thin sections corresponding to known water-cement ratio of 0.4, 0.5 and 0.6 respectively were used in the process. The reference sections were standardised sections of ordinary portland cement prepared at 56 days after casting concrete.

A Leica compound microscope was used to acquire images. The microscope made use of a yellow blocking filter and a blue UV filter to produce the images. A flat field correction was applied to the images to avoid the 'vignette' effect so that an image with a uniform light intensity was obtained. Around 10 images were acquired per sample including the reference samples. The same lighting, exposure and magnification conditions were used to acquire all the images. The presence of fluorescent dye emits a fluorescent green light when the light hits the epoxy. All the images were calibrated to the green light intensity emitted by the air voids in thin-sections to get normalised histograms. All the images of a particular sample were stacked together and a cumulative histogram of the light intensity was plotted. Only the green channel of the RGB image was analysed and hence an 8-bit scale was used. The analysis was performed using the open access software 'FIJI'. The images are presented in fig 3.21.

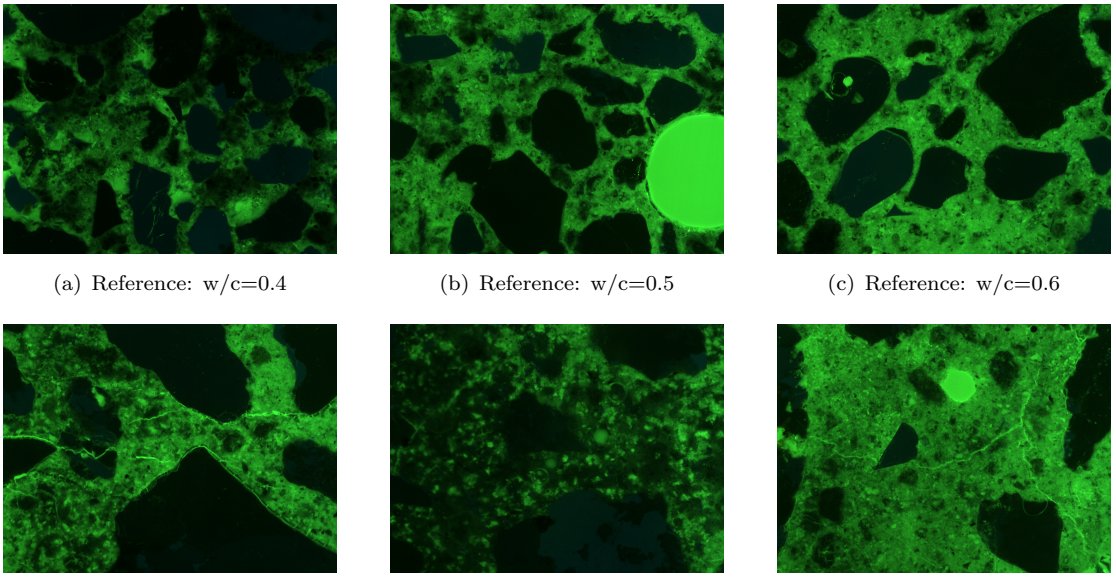

(a) Reference: w/c=0.4 (b) Reference: w/c=0.5 (c) Reference: w/c=0.6

(d) K22-16(3) (e) K23-15(3) (f) K27-16(3)

FIGURE 3.21: Image acquisition for estimating water-cement ratio

The intensity of green light is directly related to the capillary porosity in the paste and consequently it is related to the water-cement ratio. Higher the intensity of the green lights, higher is the concentration of the epoxy. This means the capillary pores are higher and hence the water-cement ratio is also higher. The reference samples in fig 3.21 clearly show the gradation in the light intensity. The histograms for all the samples with the reference samples are presented in 3.22. It can be seen that three main peaks are observed per thin section. First sharp peak corresponds to the coarse aggregates, the second well distributed peak is the mortar phase where was the third observed peak corresponds to the air voids. The mean value of the mortar phase was compared to estimate the water-cement ratio. It was observed that most of the samples lie between the reference peak of w/c=0.40 and w/c=0.50. The sample with w/c=0.60

was considered to be an erroneous sample. To be on a safer side, the water-cement ratio was assumed to be equal to 0.50. This is further used to estimate the mix design of the mix.

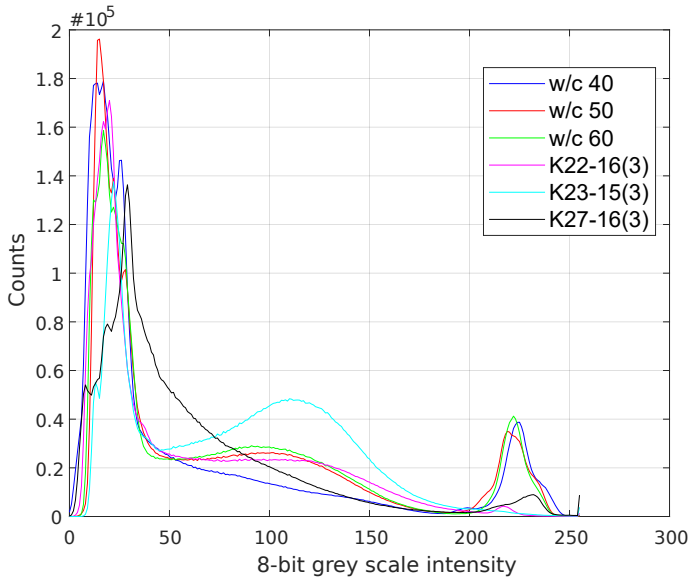

FIGURE 3.22: Histogram of 8 bit image stack for estimation of water-cement ratio

3.5.4 Micro-structural features of ASR

Typical signs and symptoms of ASR are already discussed previously. This test aims to identify the symptoms observed in the literature to confirm the presence of Alkali Silica reaction in the structure. The reaction product of ASR also called as gel can be seen as a white viscous gel through the cracks under plane polarised light. It has a distinct white colour which distinguished it from the yellow coloured epoxy. The presence of gel is confirmed by using crossed polarised light. The gel being amorphous in nature does not exhibit birefringence. The cross polarised filter being perpendicular to the polarising filter will block all the polarised light unless it is a polarised light parallel to the XPL filter which is the case only observed if the material is anisotropic in nature. Since amorphous materials tend to be isotropic, no light passes through the XPL filter and they are seen as dark objects. Hence the gel appears to be dark under XPL lighting. Some selected images of both PPL and their corresponding XPL images are presented in fig 3.23. The other micrographs can be found in appendix E.

The white ASR gel can be observed in each of the image under PPL. Fig 3.23(a) shows the typical branching nature of ASR in the cement paste. The cracks extending and propagating through the aggregates filled with reaction material can be observed in fig

3.23 (a) and fig 3.23 (g). Another common feature of ASR cracking is debonding of the aggregate or propagation of the cracks through the ITZ as seen in fig 3.23(e) and fig 3.23(f). The ITZ being a porous zone results in the formation of gel pockets and eventually cracking in the ITZ because of the development of imposed stresses when the porous zone gets completely filled by the gel. fig 3.23 (a) shows dissolution of the aggregate along the rim whereas fig 3.23 (c) shows presence of a dark reaction rim which is also a typical sign of ASR. The reactivity of the aggregates is based on the size of the mineral grains (mostly quartz). Fig 3.23(d) shows presence of cryptocrystalline quarts grains ($< 30\ \mu m$) and fig 3.23 (h) shows presence of fine quartz grains within the interstitial space of coarser quartz grains of sandstone. These finer grains provide a larger surface area for the reaction and hence can be deemed as potentially deleterious.

3.6 Estimation of original mix design

The volumetric compositions obtained earlier is converted to compositions by weight. The methodology adopted by Eden (2010) was used to calculate the weight percentage. The type of cement and the type of aggregates were chosen based on the analysis in the previous section. Their corresponding densities were borrowed from the literature.

Phase	Assumed Material	Density (ρ) (kg/m^3)
Coarse Aggregates	Sandstone	2650
Fine Aggregates	Siliceous Sand	2620
Cement	Ordinary Portland Cement	3140

TABLE 3.1: Density of individual phases

The weight fraction of individual phase for 1 m^3 of concrete was calculated in the following way:

$$W_{CA} = \frac{\%V_{CA} \times \rho_{CA}}{100} \quad kg/m^3 \tag{3.1}$$

$$W_{FA} = \frac{\%V_{FA} \times \rho_{FA}}{100} \quad kg/m^3 \tag{3.2}$$

The weight of cement was calculated using the following equation. The water-cement ratio (w/c) along with volumetric fraction of the paste was used to determine the quantity of cement. The derivation of the equation can be found in appendix D.

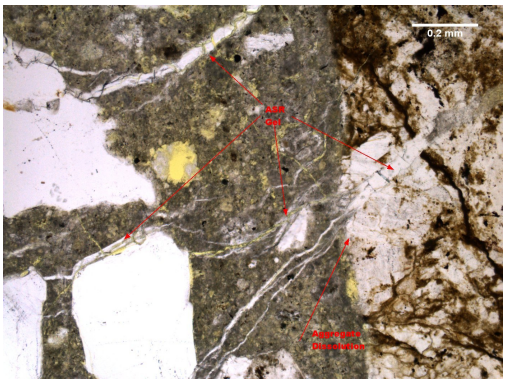

(a) K22-16(3) (PPL)

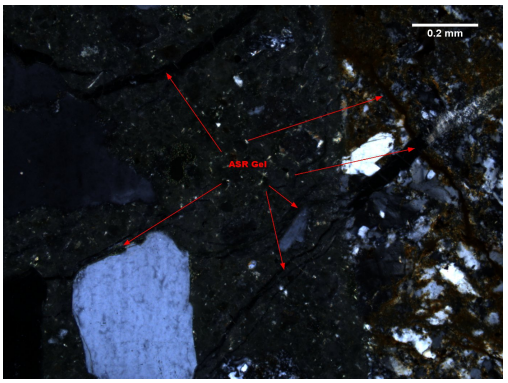

(b) K22-16(3) (XPL)

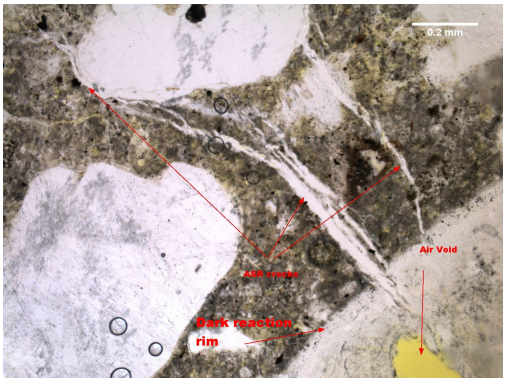

(c) K23-15(2) (PPL)

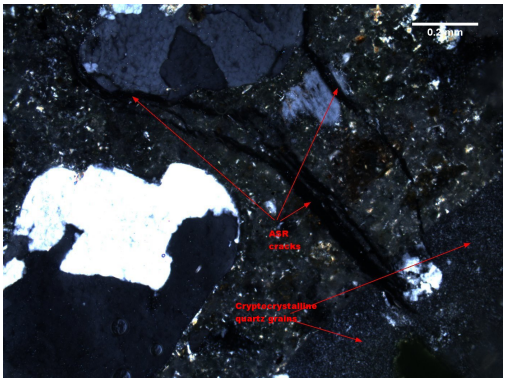

(d) K23-15(2) (XPL)

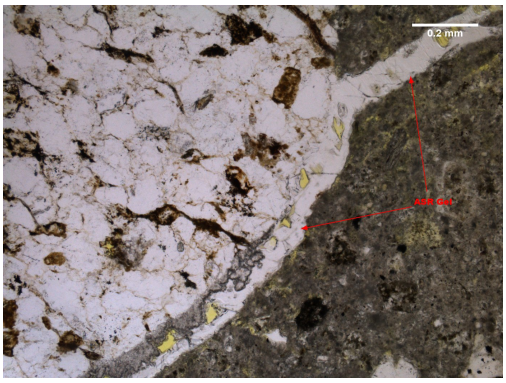

(e) K22-16(3) (PPL)

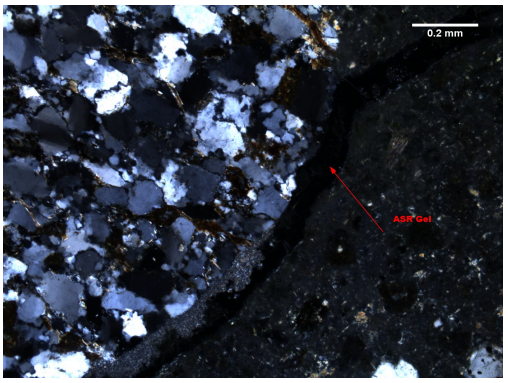

(f) K22-16(3) (XPL)

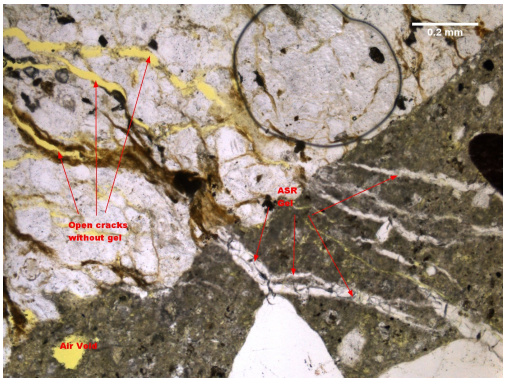

(g) K27-16(3) (PPL)

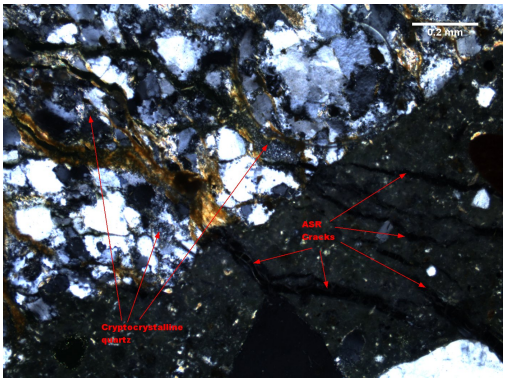

(h) K27-16(3) (XPL)

FIGURE 3.23: Typically observed ASR symptoms using Polarised light microscopy

$$W_{cem} = \frac{\%V_{paste}}{100 \times (\frac{1}{\rho_{cem}} + \frac{w/c}{\rho_{water}})} \; kg/m^3 \tag{3.3}$$

The mix design was calculated as an average value of all the samples. It is presented in table 3.2.

For 1 m^3 concrete	
Coarse Aggregates	1246 kg
Fine Aggregates	480 kg
Cement (OPC)	414 kg
Water	207 kg

TABLE 3.2: Estimated Mix Design. The quantity is calculated for 1 m^3 concrete

3.7 Damage rating index (DRI)

The method proposed by Grattan-Bellew and Mitchell (2006) was adopted to find relative physical distress at different locations of the structure. The experimental setup was modified and simplified to suit the user. The test was performed with a stereo microscope using a UV light. Yellow blocking filter was used to achieve a uniform green image without interference of other wavelengths. Cracks filled with epoxy were illuminated because of the fluorescent dye and consequently the cracks became more pronounced. The images were acquired at a magnification of 6.3x in the eyepiece with a field of view of around 12.5 x 11 mm for each image. The images were acquired in successive rows. The precision and straightness of the image was maintained by use of a state of the art computer operated moving table as shown in fig 3.25 (b). The moving table also prevented any rotation of the sample so that the sample always remained parallel to the camera lens. These images were stitched together in the same grid-wise order using the open source image editing software 'FIJI'. A sufficient overlap of 25% between two successive images increased the accuracy of stitching them together. Finally a high resolution image of the entire sample was achieved with this method as seen in fig 3.25.

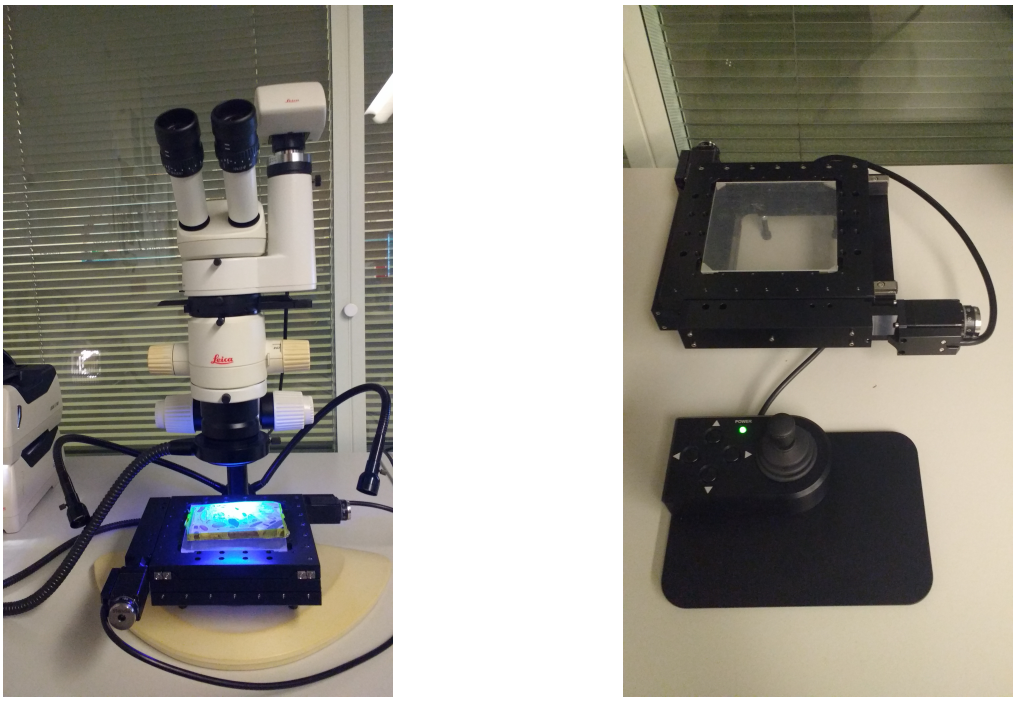

(a) Petrographic stereo microscope

(b) Moving table

FIGURE 3.24: DRI experimental setup

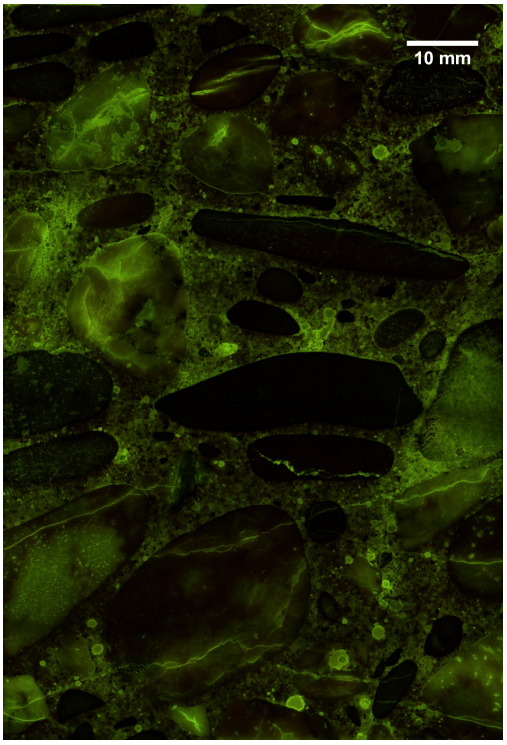

FIGURE 3.25: Example of a stitched image. Sample: K22-16(2). The image is acquired using a stereo microscope with UV light and yellow blocking filter. Exposure= 483ms

A grid of 1 cm^2 was superimposed on to the image. The same weighing factors as

introduced by Villeneuve et al. (2012) were adopted. Moreover, classifications with the same weights were combined into one class. The notations and classification features used by her were maintained in the same way. The classification and weights are listed in table 3.3. The detailed explanation of the features can be found in the same paper.

Petrographic features	Abbreviation	Weight
Closed/tight cracks in coarse aggregates	CCA	0.25
Opened cracks or network of cracks with or without reaction product	OCCA/CCAG	2.0
Coarse aggregate debonded	CAD	3.0
Cracks in cement paste with or without reaction product	CCP/CCPG	3.0

TABLE 3.3: DRI weight factors (Villeneuve et al., 2012)

The features were counted for each grid. The cell counter feature of imageJ was used to count these features. An indirect length of the cracks was obtained since the crack was counted more than once if it passed different grids (Sanchez et al., 2016). The counts were normalised to an area of 100 cm^2. These were multiplied by their respective weighing factors to get the value of DRI. The closed cracks were assigned a low factor as it is assumed that these cracks existed because of original defects and weathering mechanisms but not necessarily because of ASR. The absolute as well as weighted results are presented in fig 3.26 and fig 3.27 respectively. It can also be observed that the DRI values from the same cores have similar values indicating similar level of damage. Conclusions on relative damage can be drawn from the DRI values. However, no information regarding the mechanical properties, crack widths or crack orientation can be deduced using this method.

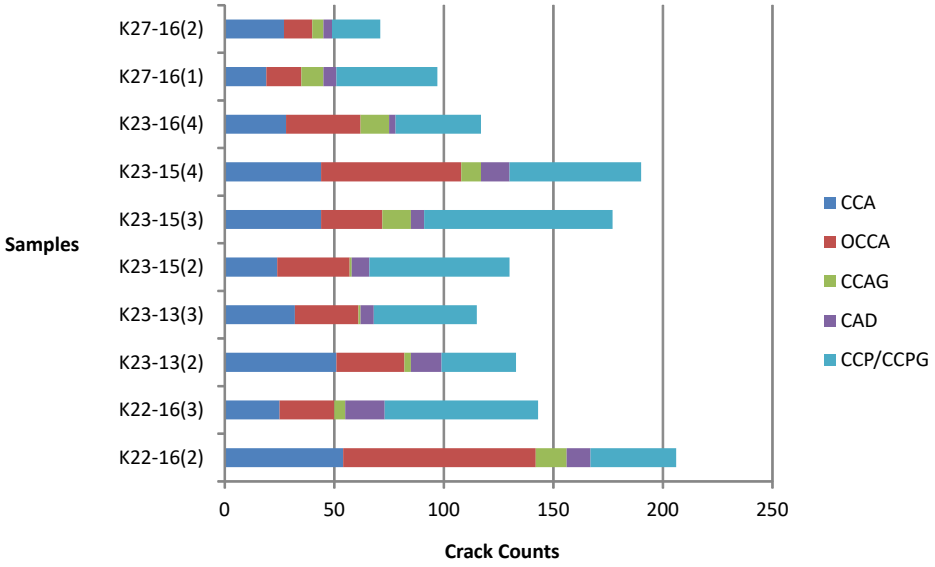

FIGURE 3.26: Damage rating index: absolute counts

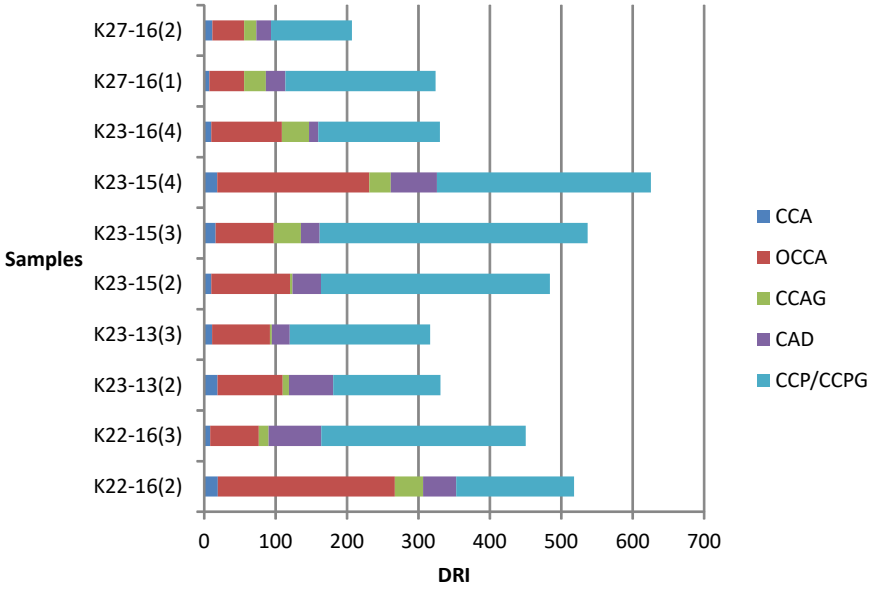

FIGURE 3.27: Damage rating index: Weighted values

3.8 Image analysis of cracks

Image analysis served to be an alternate tool to DRI to perform quantitative analysis of crack features.The image acquisition procedure was similar to DRI except the image was acquired without using the yellow blocking filter. This resulted in a prominent contrast between cracks and the porosity of capillary pores. This was particularly important to

segment the image. The image segmentation protocol is discussed in detail in appendix B. The final product of segmentation was a binary image containing only cracks. However, some minor air voids having the same intensity and a weak circularity were not filtered out. These were inadvertently included in the analysis. The image was analysed for crack densities. This data is further used to compare with the output from the lattice model.

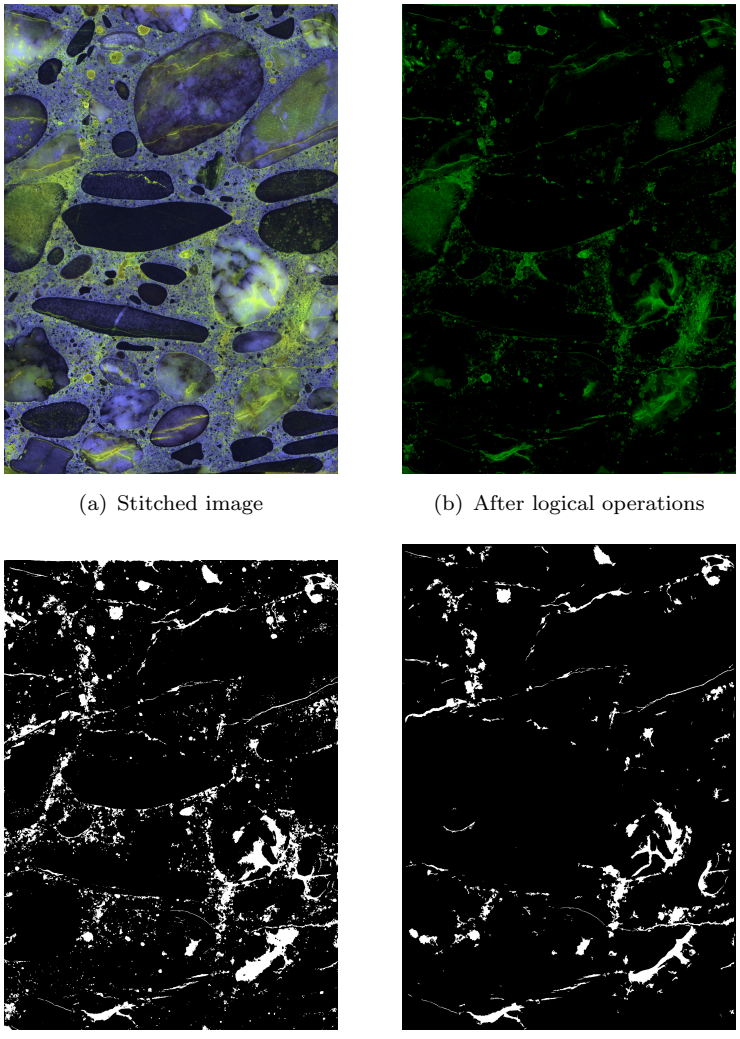

(a) Stitched image

(b) After logical operations

(c) Binary Image after manual corrections

(d) After applying circularity threshold

FIGURE 3.28: Crack segmentation at different steps

3.8.1 Calculation of crack densities

The methodology used to calculating crack densities is similar to one proposed by (Lindgård, 2013). The acquired binary image contained only 2 logical values. One value for the cracks (v=255) and other (v=0) for the rest of the sample. The values

were based on the 8 bit grey scale. The number of pixels corresponding to the crack was easily counted using the image analysis software 'FIJI'. The crack densities were calculated as a percentage value as shown in equation 3.4. The crack densities are presented in table 3.4.

$$Crack\ Density(\%) = \frac{(Number\ of\ Pixels)_{v=255} \times 100}{Total\ Pixels} \tag{3.4}$$

A correlation study was also performed to compare the obtained DRI values with the crack densities obtained from image analysis. A strong linear correlation with a coefficient of determination (R^2) value equal to 0.91 was obtained from fig 3.29. Since image analysis is a faster semi-automated method, it can result in a good estimate of the DRI value before performing the damage rating test. DRI being a more tedious method can be used later to perform a detailed analysis of crack classification if required.

Sample	Counts (Pixels)	Crack area (mm2)	Sample Area (mm2)	Avg size (mm2)	Crack Density (%)	Mean Pixel Value	Perimeter (mm)	Avg Circularity
K22-16(2)	335	292.31	7871.05	0.873	3.714	255	6.29	0.19
K22-16(3)	2275	239.64	8404.14	0.105	2.851	255	1.618	0.1
K23-13(3)	1125	107.50	7541.97	0.096	1.425	255	1.965	0.16
k23-15(2)	301	182.65	5350.92	0.607	3.414	255	9.583	0.11
K23-15(3)	544	199.35	6331.96	0.366	3.148	255	6.833	0.15
K23-15(4)	820	269.20	5725.30	0.328	4.697	255	4.628	0.17
K26-14(4)	361	99.81	7076.81	0.276	1.412	255	6.632	0.17
K27-16(1)	2101	128.39	6899.19	0.061	1.861	255	1.243	0.12
K27-16(2)	612	85.30	6648.63	0.139	1.283	255	3.621	0.15

TABLE 3.4: Image analysis of cracks

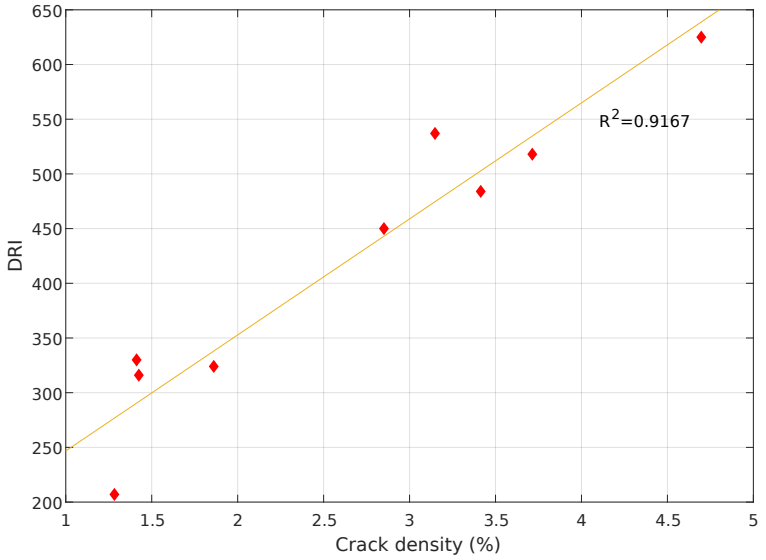

FIGURE 3.29: DRI versus Crack density

3.9 Determination of the Young's modulus

It was already observed in Chapter 2 that the Young's Modulus of concrete is a more sensitive mechanical parameter when it comes to ASR affected structures as compared to the compressive strength. Moreover, the compressive strength of ASR damaged concrete was found to remain more or less similar. Thus, the elastic modulus of the damaged cores was determined by performing mechanical tests.

Sample preparation

The test was performed on two concrete cores: K22-14 and K27-14. The standard length of the specimen as per ISO 1920-10:2010 is 40 cm. However, the specimen length was reduced to 25cm for specimen K27-14 to avoid the presence of reinforcement in the specimen. The diameter of the core was 100 mm. The ends of the cylindrical core were made flat using a hand grinder and Silicon carbide paper of FEPA 120 (125 μm) grade. 4 fixed metallic holders for Linear variable differential transformer (LVDT) sensors were glued to the core along each quadrant in the middle one-third of its length. A two-part epoxy padding was used as an adhesive to glue the holders. The spacing between the holders also known as the reference spacing was set to 12 cm.

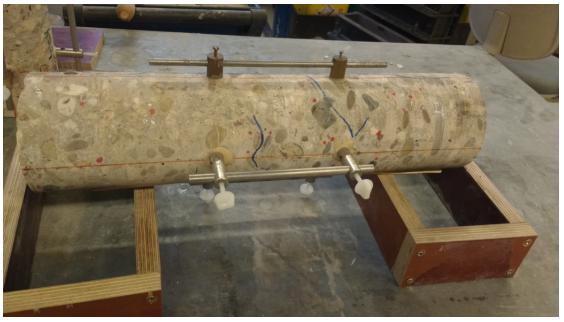

FIGURE 3.30: Gluing the LVDT holders in the middle one third of the section. The spacing between the holders was maintained at 12 cm.

Test setup

The test was performed in a universal testing machine. ISO-1920-10:2010 was used as a guideline. The samples were loaded to 30% of its compressive strength. As a reference compressive strength, the lowest test value (37.7 MPa) obtained from the investigation of Borsje and Swinkels (2016) was used to prevent the sample from being damaged. Thus, both the samples were loaded to a force of 100 kN based on the 100 mm core diameter. Three loading cycles were performed and the displacements were measured by the four LVDT sensors. Average value of the displacements recorded by the LVDT

sensors was used to compute the stress-strain relationship. The stress (σ) and strain (ε) were computed as follows:

$$\sigma = \frac{F_{recorded}}{A} \tag{3.5}$$

$$\varepsilon = \frac{L_{avg}}{L_{ref}} \tag{3.6}$$

Where, $F_{recorded}$= recorded force, A=area of cross-section of the specimen, L_{avg}= average recorded vertical displacement by the LVDTs, L_{ref}= Reference spacing. The stress-strain curve is presented in fig 3.31. The Young's modulus is determined as the slope of the linear-zone of the stress strain curve obtained from fig 3.31. This is presented in table 3.5.

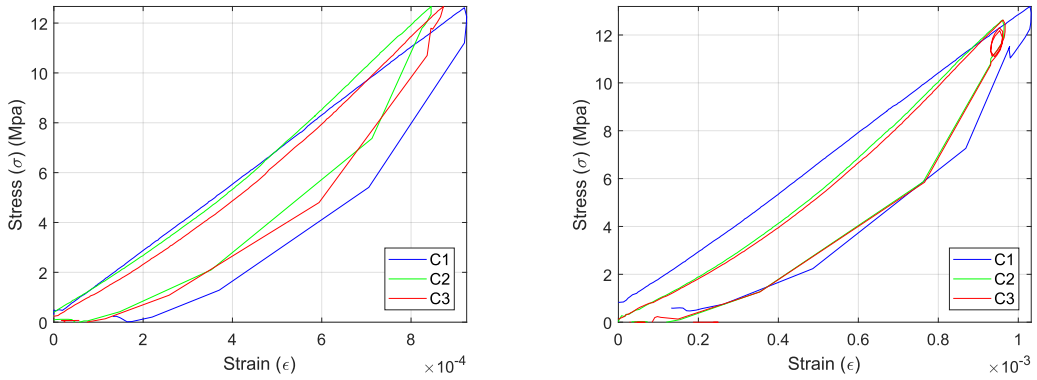

(a) K22-14 (b) K27-14

FIGURE 3.31: Stress-strain curve obtained from the mechanical test used to compute Young's modulus of the specimen. C1, C2 and C3 correspond to loading cycle 1, loading cycle 2 and loading cycle 3 respectively.

Sample	Load Cycle	Young's Modulus (E) (GPa)	Average (E) (GPa)
K22-16(2)	C1	13.65	13.84
	C2	14.17	
	C3	13.72	
K27-14	C1	13.53	14.1
	C2	14.54	
	C3	14.23	

TABLE 3.5: Result for Young's Modulus (E)

For a cylindrical compressive strength of 37 MPa, The Young's modulus can be estimated to 32 GPa as per NEN-EN 1992 1-1. Based on the findings of Swamy (1992) and Esposito et al. (2016) it can be assumed that the compressive strength is not affected significantly due to ASR. Thus, the estimated Young's modulus of 32 GPa can be considered to be the Elastic modulus of the undamaged sample. Thus, when compared with the experimental

results, a 56% reduction of the Young's modulus was obtained after 85 years. This reduction is significantly high and could have an impact on the structural behaviour. However, the data is presented only for two samples and may not be representative of the whole structure.

3.10 Chapter summary

1. Point counting analysis on polished sections and image analysis of thin sections was used to determine the composition of the existing concrete. The method of point counting was modified by using a photo-scanner and image processing software instead of a stereo microscope. This method has the potential to drastically reduce human errors and keep track of the counts efficiently.

2. The type of cement was estimated to be ordinary portland cement (CEM I) with presence of some volcanic trass.

3. The most common type of aggregate found in the analysis was sandstone with a varying degree of grain sizes. Presence of crypto-crystalline quartz, strained quartz in the the interstitial zone as well as grain size smaller than 60 μm was confirmed deeming the aggregates potentially reactive. Porous chert with micro-crystalline quartz was also confirmed. A further point counting of individual grains could provide a quantification of potentially reactive grains.

4. Thin-sectional analysis showed typical signs of alkali silica reaction and hence confirmed the presence of ASR. These signs included typical map cracking, ASR gel in the cracks, dark reaction rims and cracking through coarse aggregates.

5. The water-cement ratio was assessed petrographically and estimated to be between 0.4 and 0.5. Some limitations pertaining to the reproducibility and reliability of the petrographic test needs to be assessed in the future.

6. Based on the above data, the original mix design was estimated. This can be used to cast the same concrete and perform additional experimental research in the future.

7. Damage Rating Index (DRI) test was used to quantify micro-structural features due to ASR. The semi-quantitative test provided a good idea on relative damage between various samples. DRI seems to be a cheap method to assess existing structures and monitoring damage. It provided a good classification of various features which can prove to be a good input parameter for modelling in the future. The method in this study was modified and used an UV image opposed to an image

illuminated by normal light in the original setup. This provided better visibility of ASR features.

8. Alternatively image analysis techniques were used to analyse cracks. Crack densities were used to define the damage parameter. Image analysis proved to be a more automated method with less user bias as compared to DRI. However, the analysis considers all cracks and lacks the ability to distinguish between ASR features and other damage features. The results of the analysis also depends heavily on sample preparation and segmentation techniques.

9. A strong linear correlation between DRI and crack densities was obtained. This means that DRI can be automated to some extent in the future. Moreover, it also means DRI is reproducible at least with the same user.

10. The Young's modulus was determined by performing compression test on the concrete cores. The obtained value was significantly low in the range of 14 GPa.

Chapter 4

Lattice Model

This chapter covers the meso-scale model used in this project to study expansions and crack patterns under different boundary conditions. The Delft lattice model developed by Schlangen and van Mier (1992) is used to simulate fracture at a material level. The aim of this study is to compare the crack patterns from the simulations with the samples from the Afslutidijk structure and get an estimate on the expansions which is of importance from the point of view of structural durability. As seen from the literature survey, most of the tests performed in the laboratories including the RILEM accelerated tests does not take into account the effect of confinement. One of the hypothesis is that the confinement has a significant impact on the stress distribution and consequently on the crack patterns and expansions. Multon and Toutlemonde (2006) and Morenon et al. (2017) have already demonstrated the effect of external stresses and reinforcement confinement on ASR expansions with their 'expansion transfer' hypothesis which was already explained in Chapter 2. This model attempts to test this hypothesis using the Afsluitdijk structure as a case study. Simulations are conducted on three specimens based on their Damage Rating Indices (DRI) determined earlier. K23-15(4) had the highest DRI where as K27-16(02) had the lowest DRI. Sample K22-16(2) is also simulated which can be considered to be in between the other two simulations. Thus, the simulations considered the most affected and the least affected scenarios.

4.1 Overview of the Delft Lattice Model

The Delft Lattice model (DLM) is a small scale structural model developed at the Delft university of technology by Schlangen and van Mier (1992). This model is used to simulate fracture in quasi-brittle heterogeneous materials like concrete. DLM is a discrete model where a continuum is discretised into a system of slender structures such

as beams or trusses. It follows a linear elastic constitutive law at a local level. The effective elastic properties formulation of individual elements can be found in Schlangen and Garboczi (1997). With the stiffness formulation at a local level already known, the global stiffness matrix of the system is constructed by using rotational transformation. The model follows a simplistic fracture law in a 2D state :

$$\sigma_{eff} = \frac{N}{A} \pm \frac{\alpha \times (|M_i|), |M_j|)_{max}}{W} \geq f_t \tag{4.1}$$

where the fracture occurs when actual stress in the local element (σ_{eff}) exceeds the tensile threshold (f_t). The local elements behave like Euler-Bernoulli beams with three degrees of freedom at each node namely: two in plane translations and one in plane rotation. When the tensile threshold as per equation 4.1 is reached, the element is completely removed and the stiffness matrix is reconstructed with one element less in the system. the individual beam is assumed to have a complete brittle behaviour, meaning no softening takes place at a local level and consequently there is an instantaneous relaxation of stresses. The forces carried by the failed element are now redistributed to the neighbouring elements which result in an increase of load on the system until the next element exceeding the critical threshold value is reached. The process is repeated in the same way until the fracture energy of the system is completely released. The main advantage of this method over continuum models is that the stiffness matrix does not become singular when the stiffness of the failed element becomes zero since the new stiffness matrix is constructed without the failed element. This makes inversion of the matrix possible and a realistic fracture pattern can be obtained (van Mier, 2012).

A triangular mesh is used to discretise the continuum. The heterogeneity of stiffness in the model is obtained in two ways. In the first way, an irregular lattice mesh is chosen such that length of each element is different and in turn the geometric stiffness of the element differs. This can be achieved by defining a randomness factor to locate the position of the end nodes. This can be defined as the ratio of the length of the sub-cell (A) to the length of the lattice cell (s) as seen in fig 4.1 (b). The size of the sub-cell defines the boundaries for the random location of the end nodes. The randomness ratio is restricted between a very small value like 0.001 to a value of 0.8. A randomness of 1 can result in two neighbouring nodes to be very close to each other which may cause a problem in the stiffness matrix and lead to numerical errors (van Mier, 2012). Once the random node locations are defined, the nodes are connected to form beams using Delaunay tessellation which results in an irregular triangular mesh. A randomness of zero will result in a regular triangular mesh with all elements having equal lengths. The second way of introducing heterogeneity in the model is by assigning different elastic properties to different phases defined in the meso-scale model. This can

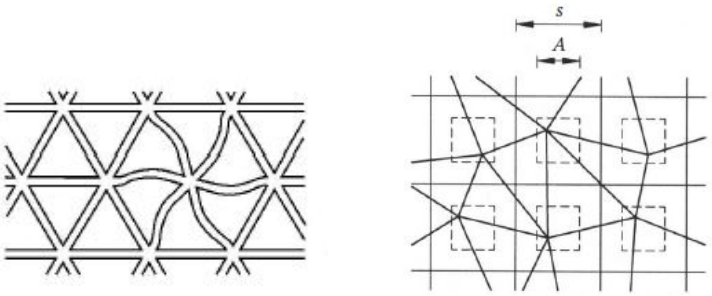

(a) Discretisation of continuum into bending beams

(b) Irregular lattice mesh

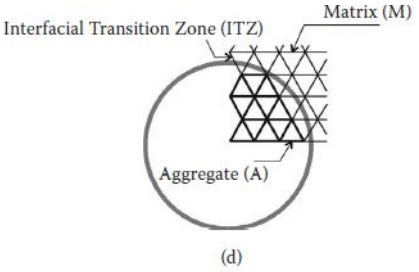

(c) Heterogeneous phases in the mesh

FIGURE 4.1: Meshing aspects of the lattice model (van Mier, 2012)

be explained by considering the fig 4.1 (c). Depending on the location of the element nodes, different phase properties can be assigned for aggregates, matrix and the ITZ. After superimposing the mesh on the microstructure, If both the end nodes lie in the aggregate phase or the matrix phase, then the phase is defined as an aggregate phase or the matrix phase respectively. If the end nodes of an element lie in both phases, then the phase is defined as the ITZ.

The Delft lattice model is based on the direct stiffness method. By imposing the boundary conditions, a set of linear algebraic equations is obtained which can be solved by analytically using the well known Gaussian elimination techniques. However, inversion of the sparse stiffness matrix (which is already quite big) results in a populated matrix which requires a significantly higher memory and consequently an extremely high computation time. As an alternative, the model solver makes use of a numerical method known as the conjugate gradient method. This is an iterative method which converges to a solution using various iterations until it reaches an acceptable residual. A detailed explanation in the solution techniques and mechanical aspects of the model can be found in Qian (2008).

4.2 Modelling approaches

The Alkali silica reaction is a complex physio-chemical process which involves relatively higher number of parameters. This makes modelling of alkali silica reaction and its effects on the material degradation a complicated process. The model chosen in this study is a simplified model. A list of assumptions is made in the process to simplify the model. These are listed in section 4.2.3.

The lattice model in this study takes into consideration only the mechanical consequences of the chemical reaction. The study does not dive into the chemical process at all. However, it considers that the chemical reaction results in localised expansions at the most likely locations in the coarse aggregates. The induced expansions also called hereafter internal local loads (LLD) initiate fracture at the location where the tensile threshold is reached. The crack propagation is based on the heterogeneity of the material properties among different phases.

4.2.1 Development of the model input

Different approaches were tried to finalise the model using trial and error as well as observations from mechanism theories from the literature. The application of internal loads is based on the two well-known mechanism theories already explained in chapter 2. The first approach follows the (Reinhardt and Mielich, 2011) theory. The coarse aggregate contains local reactive sites or existing cracks which initiate the local expansion within the aggregate. This was realised by random distribution of internal loads along the local axis of elements within the coarse aggregates. The idea of distributing the loads randomly in a spatial environment was inspired from the model by (Capra and Sellier, 2003). This also ensured that adequate tensile and compressive zones were developed within aggregate for propagation of cracks through the aggregates. It was also observed that loading all the elements of a reactive aggregate phase resulted in the aggregate elements being in compression and consequently no failure was observed within the aggregates. This method resulted in a distributed cracking pattern which was atypical of ASR unlike the localised map cracks. To overcome this, the second mechanism theory proposed by Haha (2006) was tried out. It was observed that the dissolution of the aggregates take place around the rim of the aggregates resulting in gel pockets which act as the initiation of expansion. The model assumes that not the entire rim is reactive but has localised reactive sites. This combines the Reinhardt and Mielich (2011) mechanism in a way. Various locations in the reactive rim are chosen as loading sites. These are distributed randomly only in the reactive rim. The advantage of this approach over the previous approach was that the load was localised only in the rim

zone of the aggregate (smaller area) instead of the entire aggregate. Thus, failure of the elements could follow a particular fracture path resulting in more localised and realistic crack patterns. Further the mechanical properties of the reaction rim were reduced as per the experimental findings of Çopuroğlu (2010) who also observed the dissolution of the aggregates around the rim. To make the approach more realistic, the phenomenon of gel propagation through the cracks was also attempted. It has been hypothesised that the ASR gel occupies the cracks and expands further. This imposes higher stress on the neighbouring elements of the cracks resulting in a higher overall expansion and a higher cracking density. However, the procedure proved to be not only tedious but also did not result in a significant higher expansion as it was hypothesised. The obtained crack patterns weren't realistic either and hence this approach was dropped out further. One can also consider that since ASR is a very slow reaction and takes years to manifest, the time-dependent behaviour in terms of deformation is not negligible. So an attempt to also incorporate the effect of this time-dependent behaviour was made. This part will be elaborated further in the next sub-section.

4.2.2 The finalised approaches

Two modelling approaches to develop the input parameters were finalised based on various trials performed in the previous sub-section.

Approach 1 involves modelling the load based on the dissolution theory elaborated in the previous sub-section. The model considers failure of elements in only mode 1 that is tension. Beam elements are preferred to the the truss elements. The constitutive law at the element level is linear elastic and presented in fig 4.2(a).

Approach 2 is exactly similar to approach 1 but with the inclusion of the time dependent behaviour. The constitutive law is manipulated to yield a time-dependent deformation. This model uses a bi-linear constitutive law at the element level with some softening behaviour in the second stage so that there is enough deformation in an element before it is taken out of the system and the stresses are relaxed. The law is presented in fig 4.2(b).

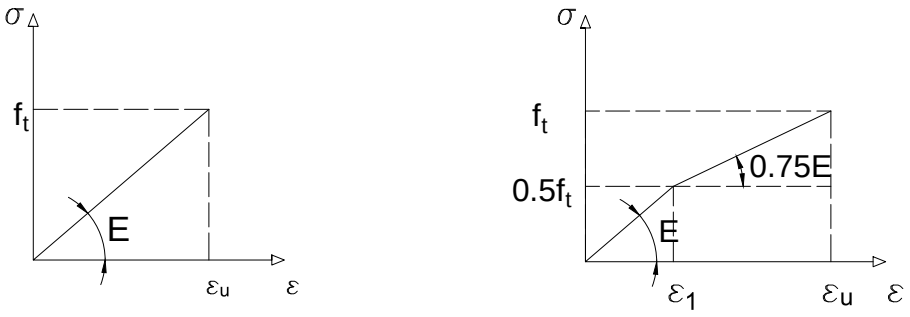

(a) Approach 1: Dissolution of aggregate rims without considering the time-dependent behaviour

(b) Approach 2: Dissolution of aggregate rims with the time-dependent deformation

FIGURE 4.2: Constitutive law of local elements

4.2.3 Assumptions

The modelling of the ASR effects is only possible by making bold assumptions. These assumptions allow to simplify the model significantly. However, one must be wary of the assumptions and consequently, the reliability of the model. These are listed below:

1. The lattice model does not take into account the physio-chemical nature of the reaction in the model but only the mechanical effect of the reaction realised as an internal expansive force. Thus, the rate of reaction is assumed to be constant which is a pessimistic case when compared to the diffusion-controlled real life situation. The applied internal load is assumed to be a static load.

2. It is assumed that all the conditions favourable for the reaction occur. The relative humidity is 100% and there is a continuous supply of alkalies.

3. The model is simplified to a 2D model. Thus, the cracks in the third dimension are ignored and consequently the expansions and strains determined are valid only for a 2D case.

4. Since the real mechanical properties of the individual phases are unknown, certain assumptions are made to input these properties. Since sandstone was the most common aggregate determined using thin-section analysis, the entire sample is assumed to contain only sandstone, the mechanical property of the aggregate is adopted from literature (Perras and Diederichs, 2014). The mechanical properties of other phases are calibrated to obtain similar mechanical properties from the calibration test conducted on the specimen.

5. The model does not take into account the properties of ASR gel or its effects. The swelling pressure exerted by the gel within the cracks is ignored. The reactive locations assumed before the simulation are the only loading points in the entire simulation.

6. It is assumed that the reaction at all the loading points occur simultaneously. The magnitude of the applied internal loads is also assumed to be the same. Since the real value of force is unknown, an arbitrary force of 1kN is applied at the reactive positions and the steps in between are calculated. The simulation is run until the force reaches 100 N. The direction of the applied load is always along the local axis of the beam and the force is always tensile.

7. It is assumed that the ASR initiates only on the rims of the coarse aggregates. The fine aggregates are assumed to be non-reactive and not considered in the model. The assumption is reasonable as although the fine aggregates are reactive, their total contribution to the overall expansion is negligible compared to the coarse aggregates. It is also assumed that only a fraction of the elements of a reactive coarse aggregate contribute to ASR. This is to prevent the entire coarse aggregate being under compression and encourage cracking within the aggregate. This fraction is assumed to be arbitrarily 20% of the total elements in the reactive zone of coarse aggregates.

8. The aggregates are labelled as reactive aggregates based only on visual examinations and crack features of corresponding coarse aggregates that were observed in the polished sections.

9. Each phase within the heterogeneous phase is considered to be homogeneous and assigned the same mechanical properties. In reality, the properties within a phase will also vary and affect the fracture. However, a homogeneous phase is considered to keep the model simple.

10. To keep things simple, the beam is assumed to fail only in tension. Every element is assumed to be perfectly brittle meaning, the fracture energy is released and the force in the element instantly drops to zero when the strength of the element is reached.

11. The model assumes two boundary conditions. The free expansion condition which is widely used in the laboratory tests and a fully restrained condition which is used to idealise the effect of confinement in the existing structure.

4.3 Input parameters

4.3.1 Mesh Properties

The mesh of the model is based on a digitally acquired scan of the actual polished sample. The same image acquired in section 3.4.1 was used for generation of the mesh. A detailed image protocol for transformation of a RGB image to a ternary image is listed in Appendix B. The image was converted to a ternary image with a distinction between the coarse aggregates, mortar and the reactive rim of the reactive aggregates. The technique described in subsection 4.1 was used for the mesh generation. The generated mesh was superimposed on the ternary image of the microstructure and different phases and mechanical properties for the elements in the mesh were defined. The entire process was performed using a primary Matlab code developed by Šavija et al. (2012) which was modified to suit the project needs. Different micro-structures and their corresponding lattice mesh are presented in fig 4.3. A closeup of the mesh as presented in fig 4.4 shows distinction between different phases. The dark blue phase represents the aggregates whereas the red phase represents the mortar. The ITZ and the reactive rim of the coarse aggregates is represented by beige and light blue respectively.

Property	Specimen		
	K22-16(2)	K23-15(4)	K27-16(2)
Specimen size (mm)	74.41 x 95.38	66.64 x 88.32	71 x 85.5
Image size (Pixels)	151 x 191	133 x 176	142 x 171
Lattice size	0.5	0.5	0.5
Randomness	0.5	0.5	0.5
Number of nodes	28841	23408	24282
Number of elements	86237	69962	72590

TABLE 4.1: Properties of mesh

(a) MicroStructure: K22-16(2) (b) MicroStructure: K23-15(4) (c) MicroStructure: K27-16(2)

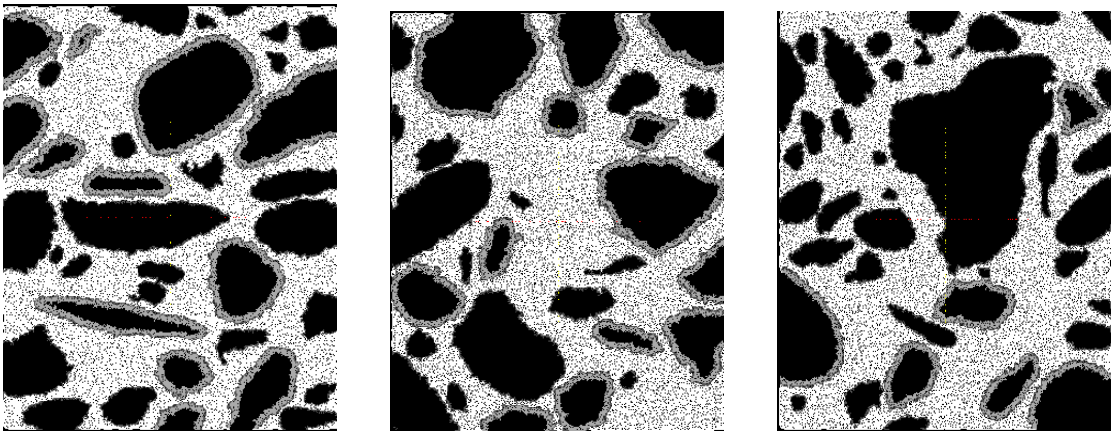

(d) Mesh: K22-16(2) (e) Mesh: K23-15(4) (f) [Mesh:K27-16(2)

FIGURE 4.3: Top row: ternary images of microstructure. Black represents the coarse aggregates, grey as the reactive coarse aggregates with a 1 mm reactive rim around them and the mortar phase is represented in white. Bottom row: corresponding mesh

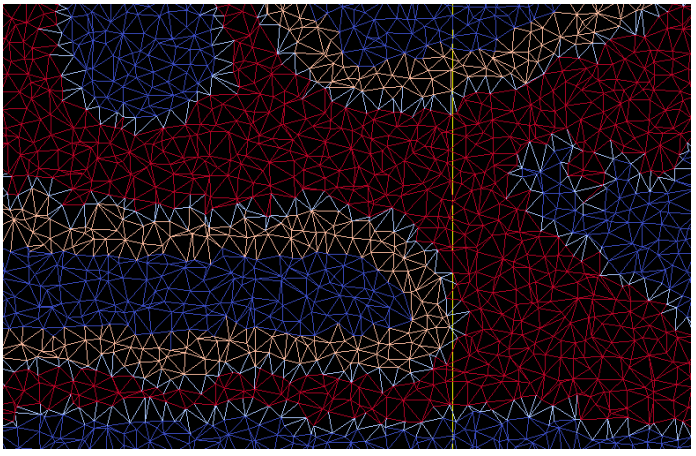

FIGURE 4.4: Close up of mesh (K22-16(2)) showing different phases. Note the colours of various phases are changed for better visibility.

4.3.2 Mechanical Properties

Each phase was defined separately when the mesh was generated. Each phase was also assigned different micro-mechanical properties. Majority of the coarse aggregates in the thin section analysis performed earlier were confirmed as sandstone, a type of sedimentary rock. To simplify the model, all the coarse aggregates were assumed to be sandstone. The mechanical properties of sandstone were adopted from the work of Perras and Diederichs (2014). Properties of other phases such as mortar and ITZ were calibrated by simulating a direct tensile test. The details of the calibration can be found in subsection 4.4.3. Moreover, properties of the reactive rim of the aggregates was assumed to dissolve and hence the mechanical properties of the aggregates were reduced as per experimental findings (Çopuroğlu, 2010).

Phase	E GPa	G GPa	f_t GPa	f_c GPa
Aggregate	70	28	0.016	0.165
ITZ	21.5	10	0.002	0.02
Paste	25	6	0.006	0.053
Reaction rim of aggregates	49	28	0.016	0.165

TABLE 4.2: Mechanical properties of individual phases.

4.3.3 Internal local load

Internal load was assumed to be a static tensile force of 1 kN. However, at each step the failure load was calculated. Thus, the simulation was run only for 100 N and the force corresponding to each failed element was calculated in between. It was further assumed that the magnitude of the tensile force is the same at all the reaction zones.

The reactive aggregates were identified by performing a petrographic analysis over the polished sections. The coarse aggregates were scanned for the most common ASR symptoms. These features were already mentioned in Chapter 2. As per the dissolution theory, only the rims of these aggregates were deemed as reactive. As per the observations this dissolution occurs based on the micro-morphology of aggregates and not the entire rim (Çopuroğlu, 2010) which gives rise to localised gel pockets within the rim Haha et al. (2007). Taking this into consideration, an arbitrary 20% of the total elements in the defined reactive rim were loaded with an expansive force of 1 kN. These elements were chosen randomly using an algorithm developed in Matlab. The location of the applied internal loads can be seen in fig 4.5. The element tag indicates the phase where tag 1

corresponds to coarse aggregates, tag 2 to ITZ, tag 3 to the rim of reactive aggregates, 4 to the mortar phase and finally 5(white) to the elements where the local load is applied.

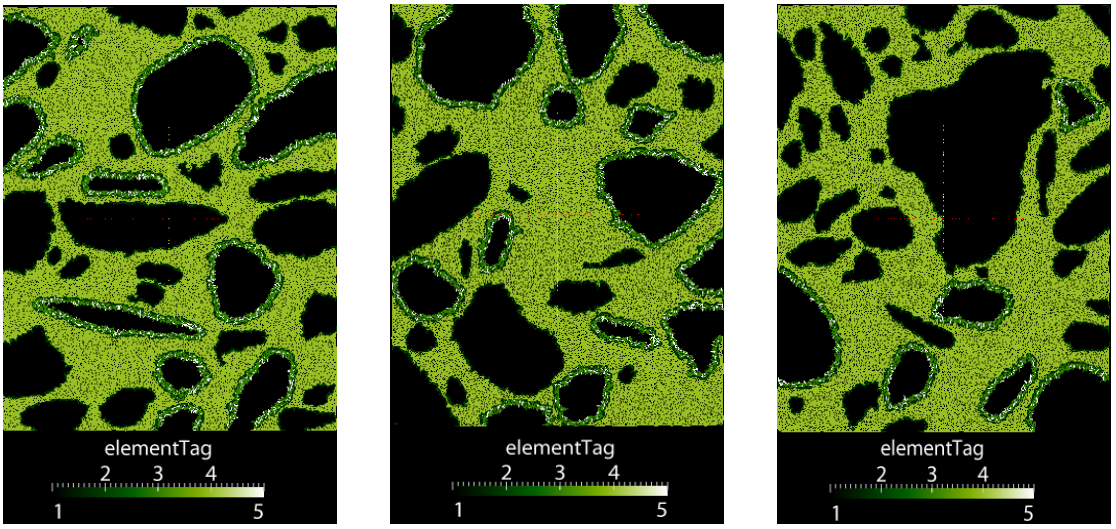

(a) K22-16(2) (b) K23-15(4) (c) K27-16(2)

FIGURE 4.5: Location of internal local loads (marked in white)

4.3.4 Boundary conditions

Two main boundary conditions were simulated using the Lattice model: free expansions and fixed edges (confinement). These can be considered to be the two extreme boundaries whereas, the most realistic boundary condition lies in between these.

The free expansion condition as the name suggests allows free expansion of all the edges in the meso-scale model. The node in the centre is not allowed to translate so as to prevent the rigid body motions. The restraints in this model are provided by the heterogeneity of different phases. The variation in stiffness of these phases results in unequal expansion of the individual elements and eventually fracture. This condition proves important since all the laboratory tests are conducted and calibrated for this boundary condition. The scheme is presented in fig 4.6 (a).

The fixed or confined boundary condition is the other extreme. In reality the specimen is not allowed to translate freely along the bending axis. The restraints are provided by the bending stresses due to existing static loads, reinforcement and the stiff neighbouring concrete elements. In this study these restraints are realised by completely confining the edges of the sample perpendicular to the bending axis whereas the less stiff edges (top and bottom) are allowed to translate and rotate. Moreover, additional restraints are provided by the variation of stiffness of different phases in the same way as free expansions. The scheme is explained in fig 4.6 (b).

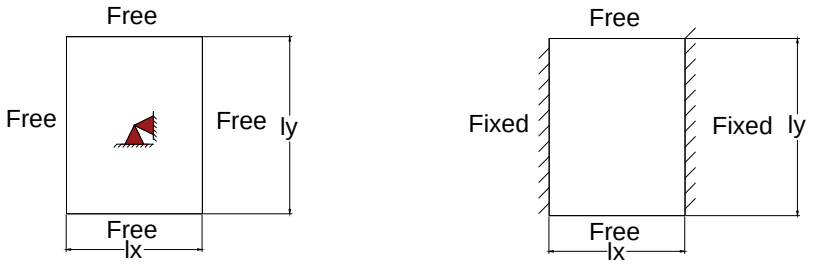

(a) Free expansions (b) Fixed (Confinement)

FIGURE 4.6: Schematic diagram for different boundary conditions

4.4 Model calibration

The stiffness of the system depends on the elastic properties assigned to the local elements as well as the geometric properties of the mesh. These properties were calibrated in such a way that the same response of the model was obtained at the global level with the input at the local level in terms of the assumed elastic properties. This was done in two steps: Calibrating the cross section of the individual elements and the calibrating the properties of the local elements to match the global stiffness of the model. A deformation controlled direct tensile test was simulated to calibrate the model.

4.4.1 Direct tensile test simulation

In the reference simulation, the model was assumed to be homogeneous and every element was assigned the same elastic properties. The compressive strength of the concrete cores was tested by Borsje and Swinkels (2016). The other mechanical properties like the young's modulus, shear modulus and the tensile strength of the core were estimated using NEN-EN 1992 1-1, clause 3.1.3 based on the mean compressive strength of the cores. The properties assumed for the concrete phase in the reference simulation can be found in table 4.3.

To simulate the direct tension test on the model, the bottom edge of the sample was provided with fixed supports. The top edge of the sample was restrained in x-direction and a prescribed displacement was applied in the y-direction such that only translation along that direction was possible to simulate a perfect direct tension test. Moreover, it was observed that the failure of elements along the top and bottom edges led to local stress concentrations and a global flexural action of the specimen which was undesirable. To avoid this, the elements at the top and the bottom edge were assigned a no failure criteria. This meant that these elements were not removed out of the system inspite of

Class: C45	
Compressive strength fcm (MPa)	53
Elastic Modulus Ecm (GPa)	36
Shear Modulus G (GPa)	15
Tensile strength fctm (Mpa)	3.8

TABLE 4.3: Properties assumed for homogeneous concrete

reaching the stress threshold . The scheme of the mechanical model is presented in fig 4.7.

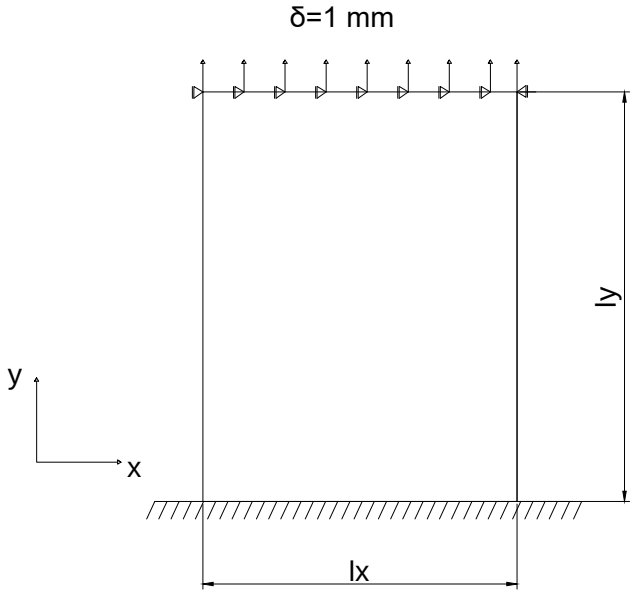

FIGURE 4.7: Mechanical model for simulating direct tension test with prescribed displacement

4.4.2 Calibrating the cross section

The local elements are defined as elements with a circular cross section. Different cross-sectional radii are assumed and the simulation is carried out using the properties mentioned in table 4.3 for each individual elements. The simulations are carried out until same non-linear stress-strain response is obtained. The Elastic modulus in the linear

zone is calculated and compared with the assumed local E-modulus assumed. The results are presented in table 4.4. Based on the results, a radius of 0.26mm seemed to give the least relative error. This was considered to be the calibrated radius.

The failure mode and the stress-strain response are presented in fig 4.8.

Tag	Radius (mm)	E (local) (MPa)	E (global) (MPa)	Error (%)
r0	0.28	36000	38447	6.79
r1	0.29	36000	40332	12.03
r2	0.25	36000	33957	-5.67
r3	0.26	36000	35461	-1.48
r4	0.27	36000	36968.92	2.69

TABLE 4.4: Calibration of the cross-sectional size of lattice elements

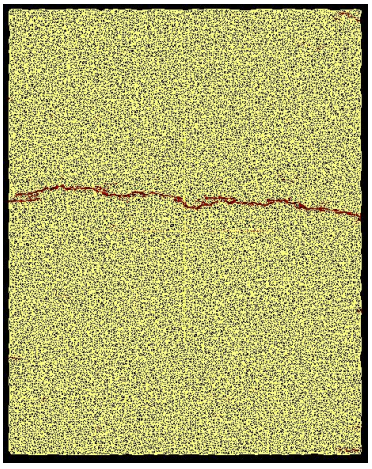

(a) Failure mode: Crack presented in red, Yellow represents the homogeneous concrete phase

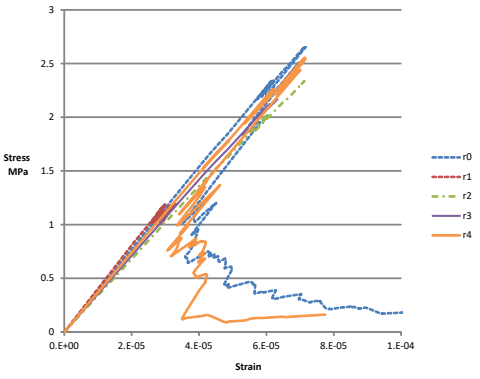

(b) Stress-strain response for different cross-sections

FIGURE 4.8: Results of cross-section calibration

4.4.3 Calibration of the material properties

The properties of the mortar and the ITZ were not known. Moreover, these properties are hard to determine experimentally especially for ITZ. Some reference mechanical properties for mortar and ITZ were assumed from (van Mier, 2012, p 75). These properties were further adjusted by simulating a direct tensile test as explained earlier albeit with heterogeneous mechanical properties to obtain a similar response obtained with the tensile test conducted on the homogeneous specimen. The test results are presented in table 4.5. Tag 'Ref' represents the mechanical properties assumed for the homogeneous

concrete specimen. A radius of 0.26mm was adopted for calibration of properties based on the previous computation results.

Tag	Phase	E GPa	G GPa	ft GPa	fc GPa	Global E GPa	Global ft GPa
Ref	Agg	36	15	0.0041	0.053	34.5	2.16
	ITZ	36	15	0.0041	0.053		
	Paste	36	15	0.0041	0.053		
P0	Agg	74.3	28	0.016	0.165	34.6	0.84
	ITZ	21.5	10	0.0018	0.02		
	Paste	22.54	6	0.0015	0.053		
P1	Agg	74.3	28	0.016	0.165	33.4	1.18
	ITZ	21.5	10	0.0018	0.018		
	Paste	25	6	0.003	0.03		
P2	Agg	74.3	28	0.012	0.165	38.51	1.18
	ITZ	21.5	10	0.0018	0.018		
	Paste	25	6	0.0035	0.03		
P3	Agg	74.3	28	0.016	0.165	38.51	1.2
	ITZ	21.5	10	0.0018	0.02		
	Paste	25	6	0.005	0.053		
P4	Agg	70	28	0.016	0.165	37.78	1.32
	ITZ	21.5	10	0.002	0.02		
	Paste	25	6	0.006	0.053		

TABLE 4.5: Variation of mechanical properties

Properties under tag P4 were chosen for further simulations. It yielded the closest young's modulus and the tensile strength among other variations. The tensile strength however, was not close to the reference properties. The reason being that the failure of the heterogeneous concrete passed through the ITZ. ITZ of different aggregates being closer to each other (Due to high packing density of aggregates) allowed propagation of the tensile crack only through the ITZ as seen in fig 4.9 (a). Thus, the tensile strength of the ITZ governed the strength of the specimen at a global level.

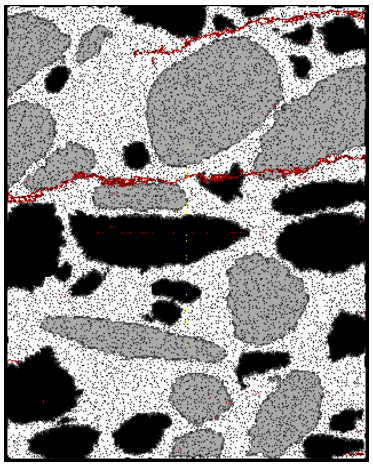

(a) Failure mode: Crack presented in red, Heterogeneous matrix can be observed in grey scale with different phases viz. Coarse aggregates, mortar and ITZ

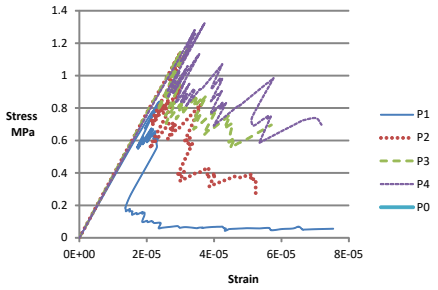

(b) Stress-strain response for different phase properties

FIGURE 4.9: Results of mechanical properties calibration for heterogeneous model

4.4.4 Calculation of the Poisson's ratio

The global effect of Poisson's ratio was calculated based on the calibrated properties. The relation for the calculation of Poisson's ratio ν of the lattice was derived by Schlangen and Garboczi (1997). It is presented as follows:

$$\nu = \frac{K - G}{K + G} = \frac{1 - \frac{12I}{Al^2}}{3 + \frac{12I}{Al^2}} \tag{4.2}$$

where, K=local bulk modulus; G= local shear modulus, A= cross-sectional area of the elements and l= length of the elements. For the assumed circular cross-section for the lattice elements, $A = \pi r^2$ and $I = \frac{\pi r^4}{4}$. Substituting in eq 4.2, the equation was reduced to:

$$\nu = \frac{1 - 3\left(\frac{r}{l}\right)^2}{3 + 3\left(\frac{r}{l}\right)^2} \tag{4.3}$$

The calibrated radius of 0.26mm was used and an average length of 0.64 mm was calculated based on the end nodes of the elements. This resulted in a Poisson's value of $\nu = 0.15$ which although on a lower side can still be considered in an acceptable range. Moreover, the equation by Schlangen and Garboczi (1997) is valid only for a regular lattice. A study by Vervuurt (1997) showed that a randomness of 0.5 resulted in the

highest possible average length of elements and a relatively low sensitivity to the variation of Poisson's ratio as compared to a regular lattice. This was used in the simulation which may result in a higher value of ν.

4.5 Results and discussions

4.5.1 Free expansion

This sub-section provides results under free expansions. The boundary condition is explained in the previous section.

Expansion strains

The expansions strains were calculated from the nodal displacements of the edge elements along both the orthogonal directions: x and y. The calculation scheme is presented in fig 4.10.

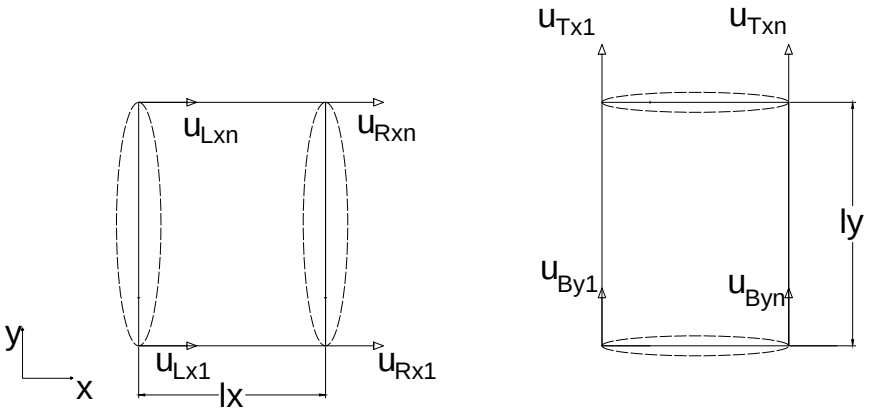

FIGURE 4.10: Scheme to calculate expansion strains from the lattice simulations.

The calculation of the average expansion strains from nodal displacements is presented below. Each node corresponds two orthogonal displacements in X and Y direction. The nodal displacements corresponding to the left edge, the right edge, the top edge and the bottom edge are denoted as $u_{\bar{Lx}}$, $u_{\bar{Rx}}$, $u_{\bar{Ty}}$, $u_{\bar{By}}$ respectively. Where,

$$u_{\bar{Lx}} = \begin{pmatrix} u_{Lx1} \\ u_{Lx2} \\ \vdots \\ u_{Lxn} \end{pmatrix} \quad u_{\bar{Rx}} = \begin{pmatrix} u_{Rx1} \\ u_{Rx2} \\ \vdots \\ u_{Rxn} \end{pmatrix} \quad u_{\bar{Ty}} = \begin{pmatrix} u_{Ty1} \\ u_{Ty2} \\ \vdots \\ u_{Tyn} \end{pmatrix} \quad u_{\bar{By}} = \begin{pmatrix} u_{By1} \\ u_{By2} \\ \vdots \\ u_{Byn} \end{pmatrix}$$

The expansion strains in the orthogonal directions were calculated by evaluating the relative displacement between the corresponding nodes.

$$\bar{\varepsilon_x} = \frac{u_{\bar{Rx}} - u_{\bar{Lx}}}{L_x} \tag{4.4}$$

$$\bar{\varepsilon_y} = \frac{u_{\bar{Ty}} - u_{\bar{By}}}{L_y} \tag{4.5}$$

Finally, mean of these strains was considered as the overall expansion in its own orthogonal direction i.e X and Y. The strains were calculated for nodal displacements obtained after every 25 steps of simulation. The strains were plotted against crack fraction. The crack fraction is defined as the ratio of number of failed elements (elements completely removed out of the system) to the total initial elements of a simulation and is expressed as a percentage. The crack fraction obtained from fig 4.12 (a) was compared with the crack densities obtained using image analysis on the actual specimens. This data is presented in the table 3.4. Both crack densities and crack fraction being dimensionless, seemed to be a plausible parameter to compare with each other. Further, the expansion strain for the corresponding crack fraction was worked out. The crack density obtained from the image analysis of the specimens was assumed to represent the present expansion strains in the simulation (i.e after 85 years of construction) due to ASR only.

It was clearly observed that approach 2 which considered the time-dependent behaviour resulted in a higher expansion for the same crack density (fig 4.11). This is a more pessimistic case and was considered to obtain the further results. It was also observed that the expansion strains in X and Y directions were similar in magnitude. This is attributed to a similar gel/force expansion in both the directions because of the lack of restraints. The gel expansion is isotropic in nature, however it depends significantly on the boundary conditions (for example geometric restraints and stress confinement) (Multon and Toutlemonde, 2006). Since the expansions in X and Y directions were almost similar, the fig 4.12 (a) only considered the results in X-direction.

The propagation of cracking resulted in a non-linear drop of stiffness. It is clearly visible in the force-displacement curve presented in fig 4.12 (b). Sample K27-16(2) shows a lesser drop in stiffness as compared to K23-15(4) which suggests that the former sample has lesser cracks as compared to the latter and hence lesser damage. This is in line with the DRI results obtained in fig 3.27. This non-linear drop in stiffness (also called as softening) is the reason for an exponential increase of strain observed for higher crack fraction in the fig 4.12.

Expansions as a function of time

The results of the expansion strains obtained from the lattice simulations shown in fig 4.12 represent the development of strains as each element fails in tension. Failure of each element in the model needs to correspond an interval in time to get an estimate of the future expansion. This was achieved by combining the response obtained from the lattice simulation with a semi-empirical model developed by Karthik et al. (2016). This research paper presents a numerical expansion model as a function of time. The model is presented in equation 4.6.

$$\varepsilon(t) = \varepsilon^{max} tanh \left\langle \frac{t - t_o}{t_r} \right\rangle \tag{4.6}$$

Where, ε^{max} is the maximum possible expansion for a specimen which remains constant. The model incorporates two empirical parameters namely t_0 and t_r. The former represents the initiation time of ASR whereas, the latter represents the time until ASR progresses linearly and can be visualised as the tangent line to the hyperbolic curve. Both these parameters are based on lab experiments in the original report. The overall function is considered to be a hyperbolic tangent to represent the diffusion behaviour of ASR. It has already been established in the literature review that the rate of reaction must slow down irrespective of the source of alkalies, silica or water as the process of diffusion becomes dominant.

In the current study the initiation time (t_0) was assumed to be 15 years based on the review by Poole and Sims (2015). Linear rise of ASR (t_r) was assumed until the first 100 years. It was assumed that alkali silica reaction proceeds at a constant rate for its nominal service life which is 100 years. The expansion strain (ε_t) corresponding to the calculated crack densities of the samples was determined using the response obtained in fig 4.12 (b). The exact values are presented in table 4.6. The present age of the specimen (t) was considered to be 85 years (time since the end of the construction). Substituting the above parameters in equation 4.6 resulted in the maximum expansion (ε^{max}) for the

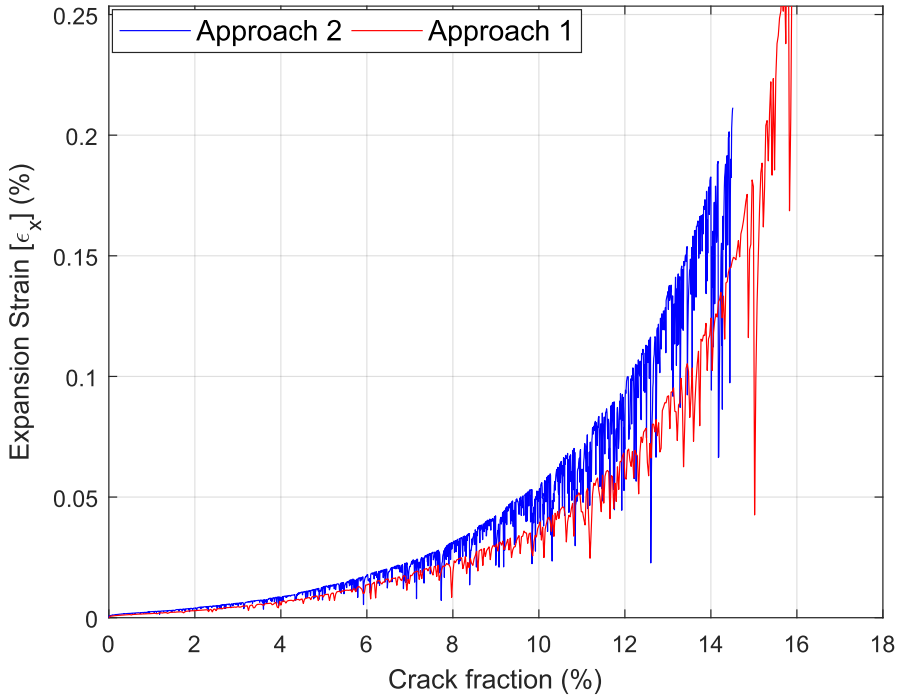

(a) Expansion strain against crack fraction along X-direction

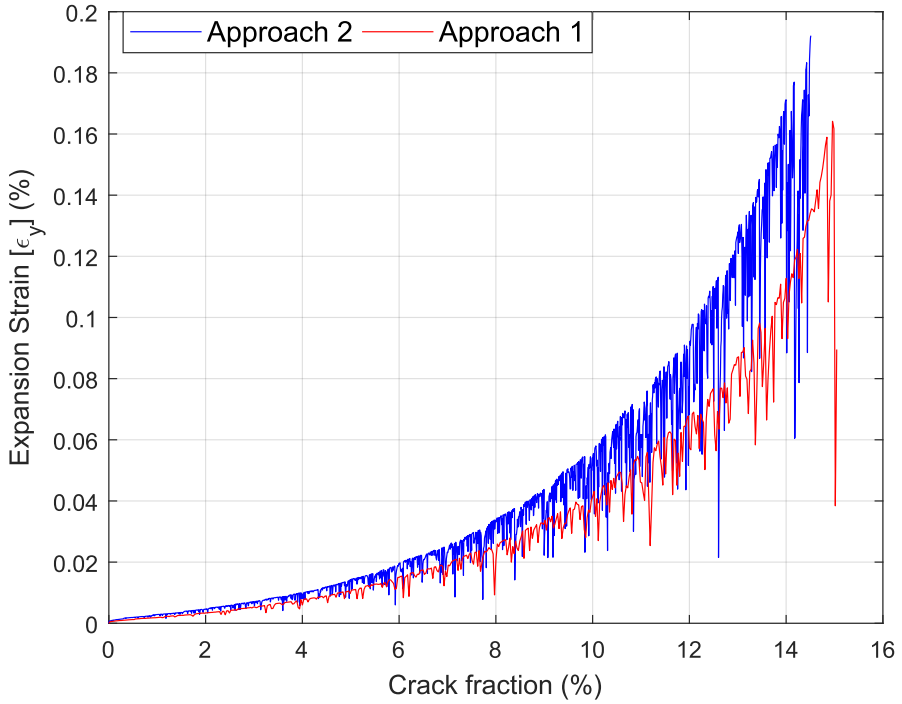

(b) Expansion strain against crack fraction along Y-direction

FIGURE 4.11: Expansion strains against the crack fraction for simulation with time dependent behaviour and and without without time dependent behaviour. The simulation is presented for sample K22-16(2) under free expansions

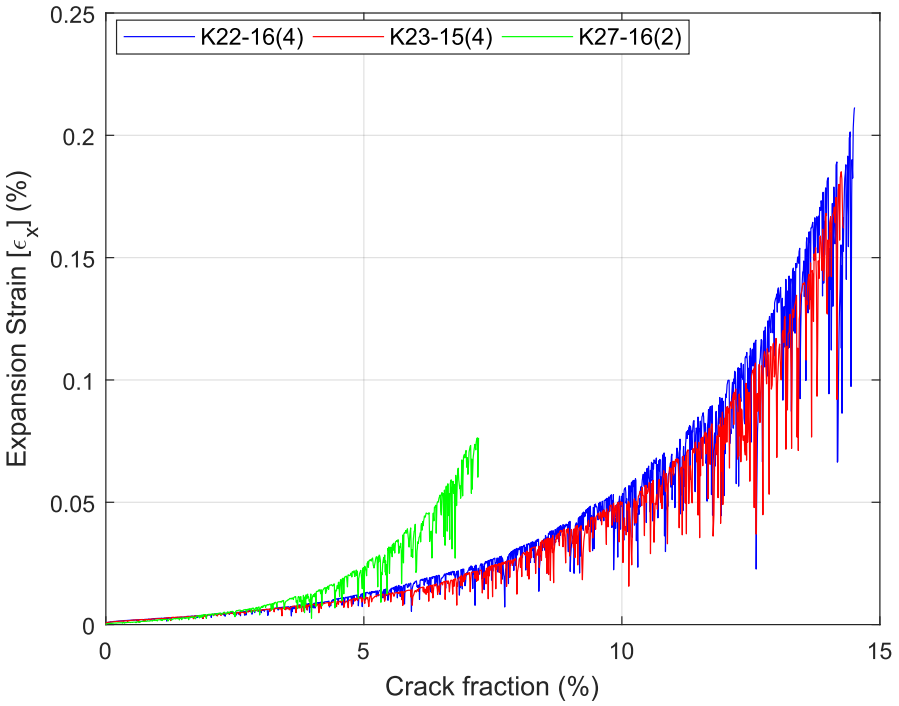

(a) Expansion strain against crack fraction

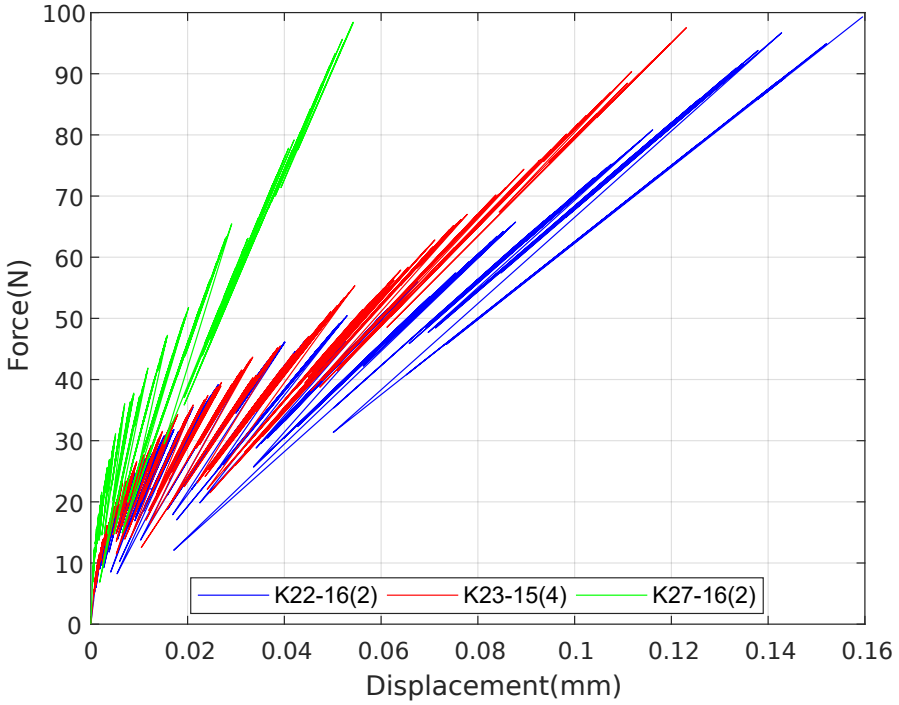

(b) Internal force versus average displacement

FIGURE 4.12: Results of the simulation under free expansions

corresponding sample. Once the ε^{max} was determined, it became possible to establish a relationship between failure of every element in the simulation and the time at which it failed. Thereby, the point in time for all the remaining expansion strains from fig 4.12 (b) was back-calculated to fit equation 4.6 and a curve representing the progress of ASR expansion in time was determined. The complex roots obtained in the process were ignored. This curve is presented in fig 4.13.

The results from the simulations fitted on the curve showed the maximum and minimum expansion strains possible for the investigated specimens. For the first 100 years the ASR was assumed to be linear after which the rate of reaction became diffusion controlled which was indicated by the drop in the rate of expansion. So, the effect of diffusion was partially considered in the time domain. As per the Norwegian accelerated test standards, the maximum permitted expansion (under free expansion conditions) in an accelerated test conducted at 38^0 C for 1 year may not exceed 0.05 % (Wigum, 2006). Similarly as per CUR 89 which are Dutch recommendations for ASR mitigation, the expansion limit is 0.04 % under similar lab conditions (Vree et al., 2005) and RILEM AAR-3 tests corresponds again to an expansion value of 0.05% (Nixon and Sims, 2016). When compared with the results obtained from fig 4.13, it was observed that the expansions were well within the permissible limits for its remainder service life. However, one must note that the crack densities obtained from the simulations are valid for free expansions which were compared with the real samples which have experienced different boundary conditions. Also, the model simulated the mechanical effect only because of ASR whereas in reality there is going to be a coupling of different degradation mechanisms which can also alter the results and the crack densities.

Sample	Crack Density (%)	Expansion strain (ε)
K22-16(2)	3.71	7.7×10^{-5}
K23-15(4)	4.70	9.7×10^{-5}
K27-16(2)	1.28	2.1×10^{-5}

TABLE 4.6: Expansion strain ε corresponding to crack densities under the free expansions. This parameter serves as a boundary condition to solve the equation of the curve 4.6

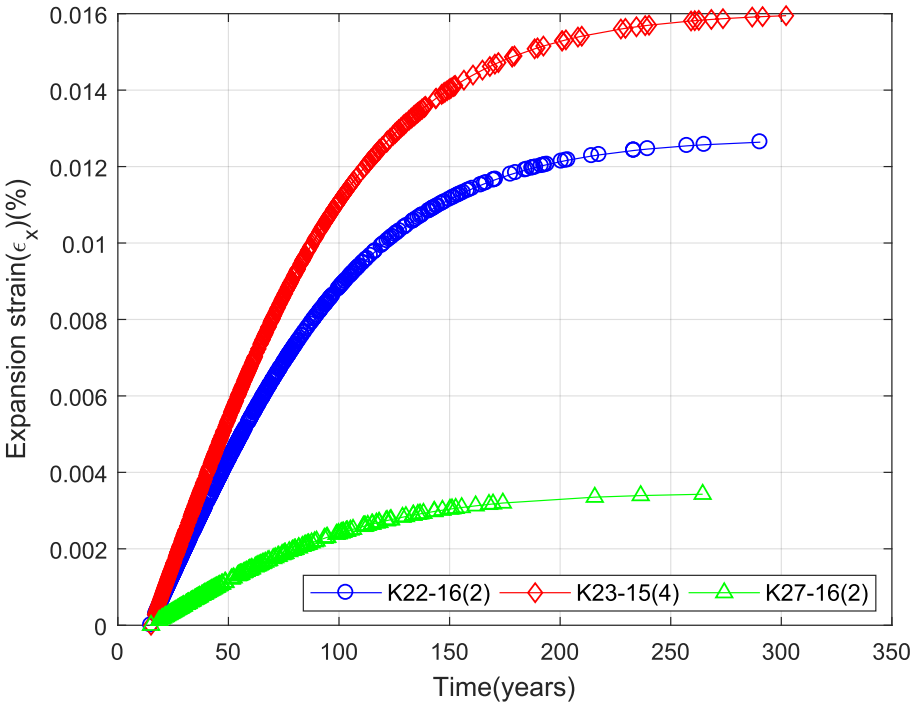

FIGURE 4.13: Progress of Expansion strains in time at the specimen level obtained by fitting lattice simulation data on the semi-empirical model by Karthik et al. (2016). Note: This result was obtained from simulations performed under free expansions only

Crack patterns

Crack patterns is a graph of failed elements plotted against its spatial coordinates. The failed elements are defined as elements that are completely removed from the system after reaching their individual tensile threshold (f_t). This is more significant for approach 2 (fig 4.2 (b)) which goes through two stages of failure. Where, only the second stage of failure is considered in the plot when the element is completely removed. The crack patterns obtained by simulating approach 1 and approach 2 are compared in fig 4.14. The difference between the crack patterns at the same failure step is the same, however approach 2 results in higher expansions due to its inherent softening included in the constitutive law further reaffirming its pessimistic nature compared to approach 1. This chapter only presents the propagation of cracks for sample K22-16(2). The crack propagation for the remaining two simulations is presented in appendix G.

A comparison of crack patterns with the actual image of the sample is presented in fig 4.15. The obtained crack pattern showcased a network of cracks which is typical of ASR. It was observed that the crack patterns obtained in simulation showed propagation of cracks in all the directions because of the lack of restraints and isotropic expansion of the gel. However,the crack pattern obtained from its corresponding UV image demonstrate

mostly cracks parallel to X direction or the direction of restraints. It is quite clear that the boundary conditions play a crucial role in propagation of the cracks and hence will affect the final expansions. Thus, it proves that free expansions which is the most common testing norm used in experimental research is not the most realistic boundary conditions and may result in erroneous results.

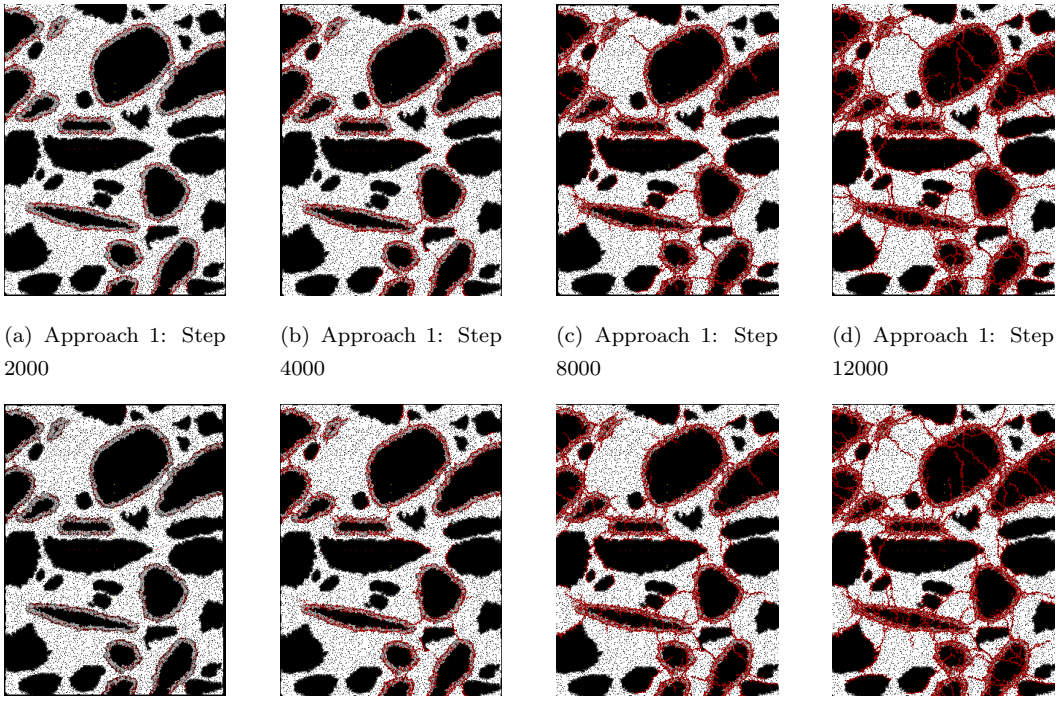

(a) Approach 1: Step 2000

(b) Approach 1: Step 4000

(c) Approach 1: Step 8000

(d) Approach 1: Step 12000

(e) Approach 2: Step 2000

(f) Approach 2: Step 4000

(g) Approach 2: Step 8000

(h) Approach 2: Step 12000

FIGURE 4.14: Comparison of crack propagation between approach 1 (top row) and approach 2 (bottom row). The comparison is done at various steps. Each step corresponds to every failed element in the lattice simulation.

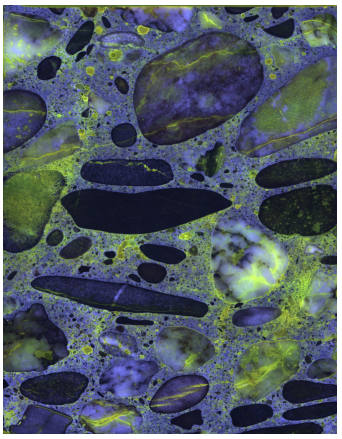

(a) K22-16(2) UV-image

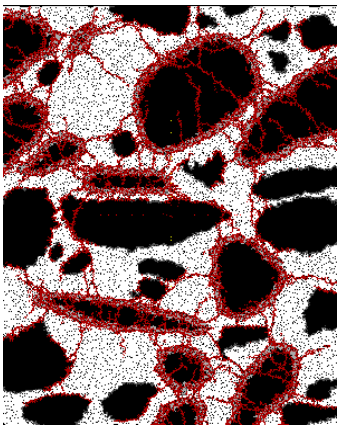

(b) K22-16(2) simulation Step 12000

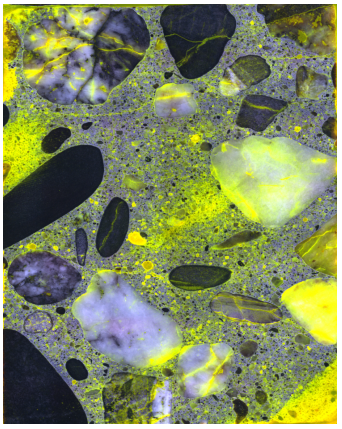

(c) K23-15(4) UV-image

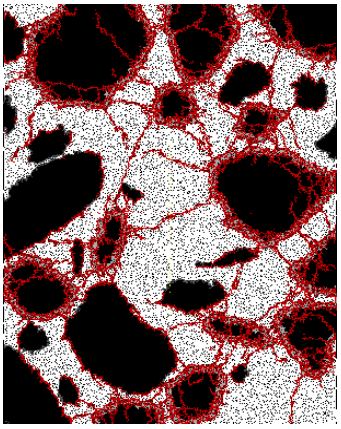

(d) K23-15(4) simulation Step 12000

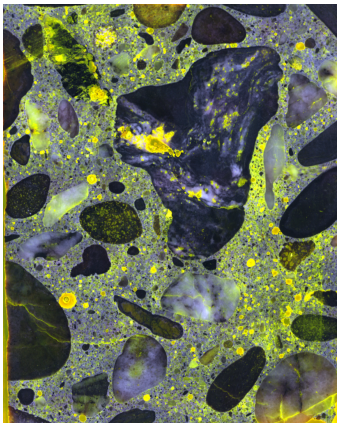

(e) K27-16(2) UV-image

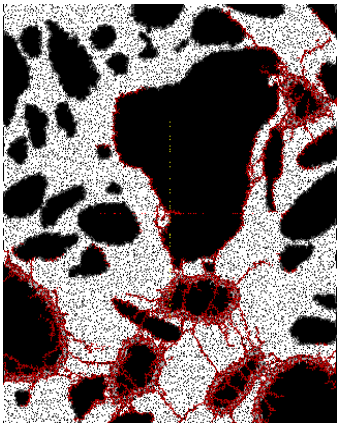

(f) K27-16(2) simulation Step 12000

FIGURE 4.15: Free expansion: Comparison of crack patterns from lattice simulations with the acquired image of the real specimens. The crack patterns are presented at a force of 100 N

4.5.2 Effect of boundary conditions

The simulations presented until now were performed under free expansions. It was already discussed in the previous part that the boundary conditions have a significant influence on the crack patterns. The simulation under free expansions already showed crack propagation in all directions which was not comparable to the actual specimens (fig 4.15) which are also subjected to confinement up to an extent. This subsection covers simulations under complete confinement as explained in fig 4.6 (b). The results and comparison between the two boundary conditions are presented in fig 4.17 and fig 4.18.

Since the model along the x-direction was completely confined, the resulting expansion strains along x-direction were obviously zero. That is the reason all the results are presented only for y-direction. It was observed in fig 4.17 (a), fig 4.17 (c), fig 4.17 (e) that the expansion strains for the fixed state was always higher than the free state for the same crack fraction. The value was approximately 15-25% higher as compared to free expansion in y direction ε_y. This is explained by means of a simplified schematic model in fig 4.16.

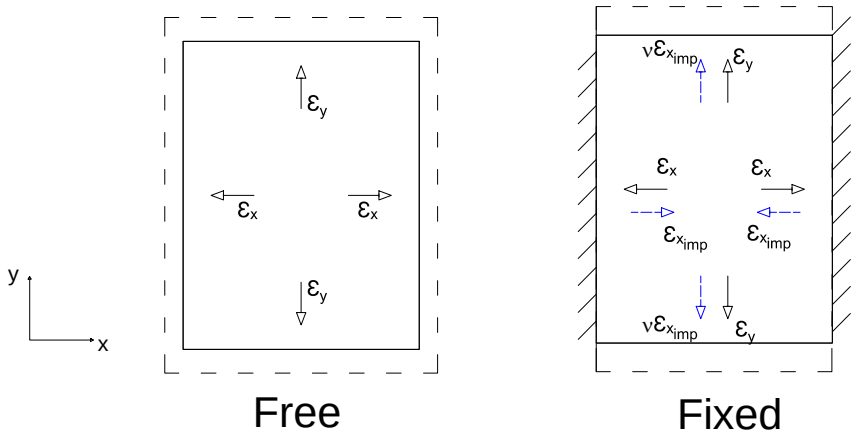

FIGURE 4.16: Schematic simplified model to explain distribution of strains for different boundary conditions. On the left the free expansion condition is presented whereas, the image on the right represents the fixed or confined state. The dotted lines indicate the likely deformed shape

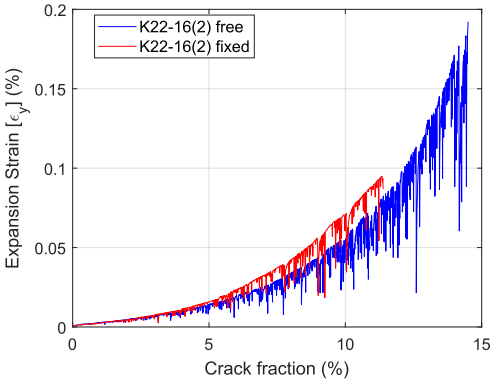

(a) K22-16(2): Expansion strain against crack fraction

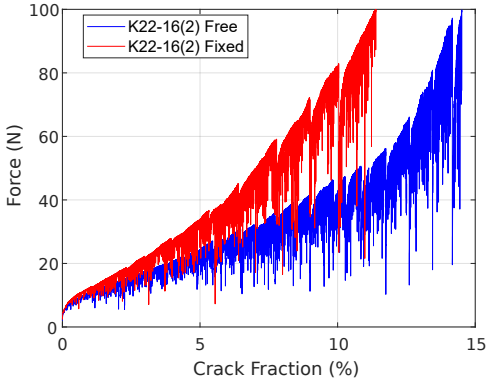

(b) K22-16(2): Force against crack fraction

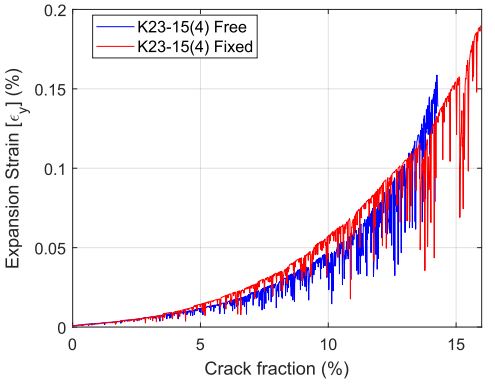

(c) K23-15(4): Expansion strain against crack fraction

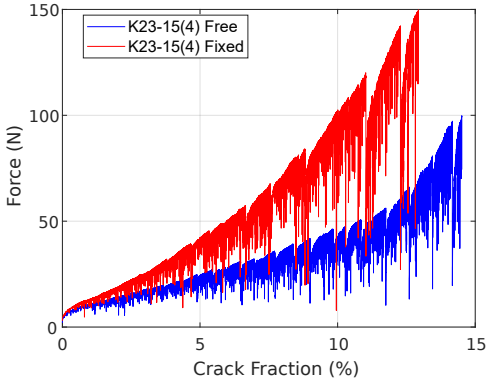

(d) K23-15(4): Force against crack fraction

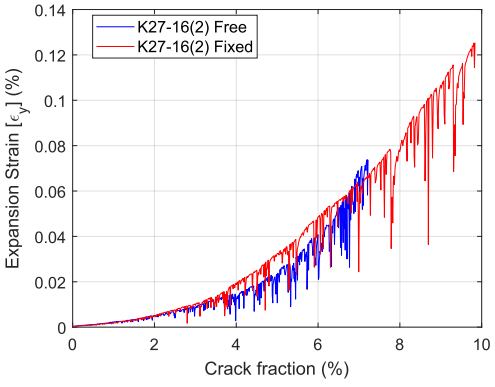

(e) K27-16(2): Expansion strain against crack fraction

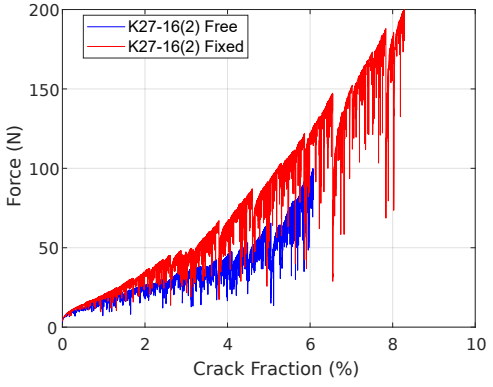

(f) K27-16(2): Force against crack fraction

FIGURE 4.17: Comparison of development of strains and forces as a function of crack fraction for different boundary conditions

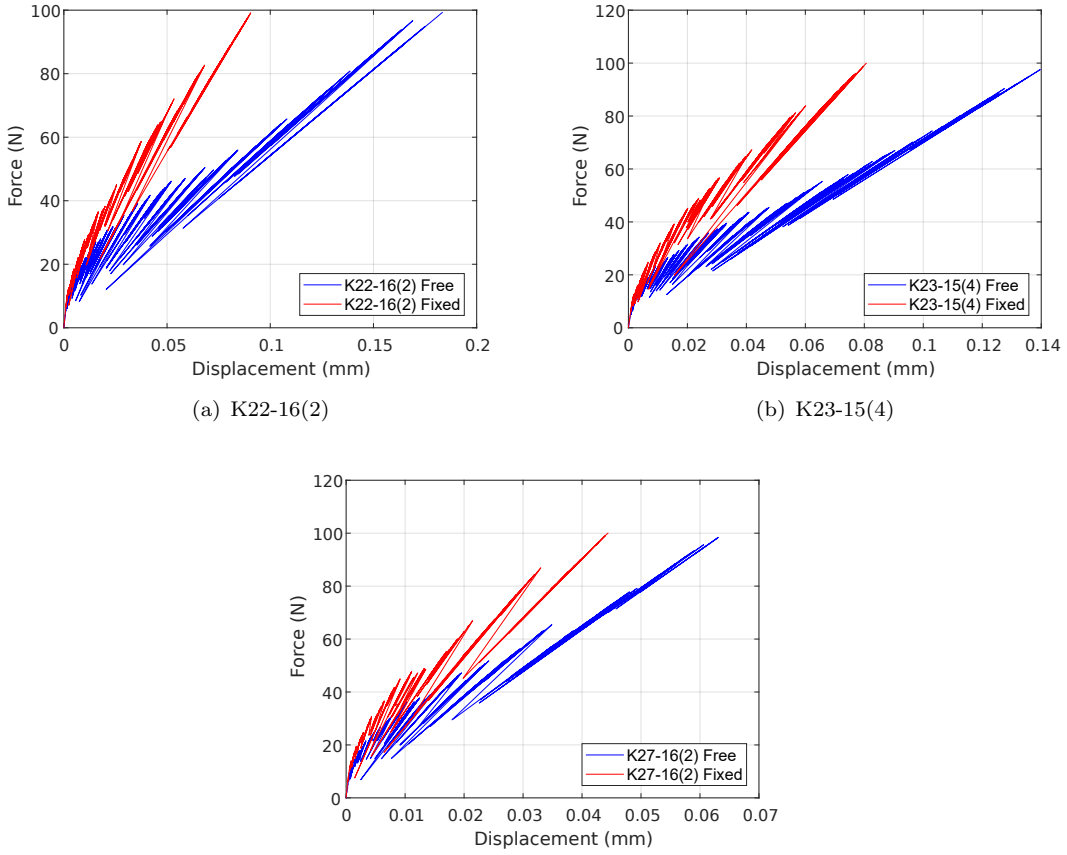

(a) K22-16(2)

(b) K23-15(4)

(c) K27-16(2)

FIGURE 4.18: Comparison of development of forces against the average displacement in the Y direction for different boundary conditions

The model in fig 4.16 is assumed to be a shell element (2D Plane stress condition). As per the model, the expansions resulted from ASR under free expansion conditions result in isotropic expansions which are represented by the deformed shape (dotted). Since the model has no restraints, it permits more or less, equal expansions in all the directions. The average expansion strains in both the orthogonal directions under this condition were also found to be similar in magnitude as seen in fig 4.11. So it can be generalised that the expansion strains in the x-direction (ε_x) and those in the y direction (ε_y) are similar in magnitude for free expansions. When the edges are completely restrained as the case is in the fixed state, the deformation in x-direction becomes equal to zero. However, the restraints give rise to an imposed strain ($\varepsilon_{x_{imp}}$) of the same magnitude as (ε_x) but the opposite direction as marked in the figure (blue). This in turn gives rise to additional expansions in the y-direction with a magnitude of $\nu \times \varepsilon_{x_{imp}}$ where ν corresponds to the Poisson's ratio of the material. Thus, the total expansion along y-direction in case of fixed boundary condition can be summed up as:

$$\varepsilon_{y_{fixed}} = \varepsilon_y + \nu \times \varepsilon_{x_{imp}} \tag{4.7}$$

For simplicity, one can assume the Poisson's ratio for concrete to be 0.2. The Delft lattice model is calibrated in such a way that it replaces the shell element to achieve the same elastic response and thus, inherently considers the Poisson's effect (van Mier, 2012, pp43-47). The Poisson's ratio depends on the area of cross-sections and the lengths of the individual elements. This was estimated to some extent using the equations provided by Schlangen and Garboczi (1997) to be 0.15. Furthermore, it was determined previously that the expansions in x-direction and y-direction were similar in magnitude. Combining all this information, the total expansion strain in the y-direction under the confined state can be reduced to $\varepsilon_{y_{fixed}} = 1.2 \times \varepsilon_y$. i.e 20% higher than free expansions for one particular crack density.

Although the expansion strains for fixed state are higher than free expansions for the same crack fraction as observed in fig 4.17, it does not imply that the damage is higher for fixed conditions as compared to free expansions. One has to observe that the evolution of forces is completely different for different boundary conditions (fig 4.17 (b), fig 4.17 (d), fig 4.17 (e)). It is evident that a higher force is necessary in case of fixed conditions to attain the same crack density. This can be explained by considering the same scheme presented in fig 4.16. Application of the same force for both boundary conditions on the presented scheme would contribute equal expansions in x and y-direction for the free expansion condition whereas, zero expansion in x-direction and merely a 20% increase in the expansions along the y-direction for the fixed state. Thus, the overall volumetric strain for free expansion will be much higher than the volumetric strain for the fixed state under the effect of the same load. Since crack fractions are directly proportional to volumetric strains, the crack fraction will also be much higher. Thus, this infact implies that under the same loading conditions, a higher damage is inflicted under the free expansion conditions as compared to fixed conditions. This is further evident in the results presented in fig 4.18. The loss of stiffness which can be determined from the slope of the force-displacement curve is much higher in case of free expansions as compared to fully restrained boundary conditions.

Fixed boundary conditions: Expansions as a function of time

The same semi empirical model by Karthik et al. (2016) was used to fit every step corresponding to every fractured element in the simulation in the time domain. The underlying assumption that each point in time corresponds to only one failed element was used again to make the fit. In the previous section, a crude assumption was made that the crack densities obtained in the free expansion simulation correspond to the present condition evaluated using image analysis. The assumption was unrealistic as the concrete cores used in this study were not subjected to free expansion. In this

section, it was assumed that the present condition of the actual specimens correspond to the simulations obtained using fixed boundary conditions. This can be considered as the upper limit of the boundary condition. In reality, even the full confinement does not exist. However, since it was difficult to estimate and execute the most realistic boundary conditions, a range between the extreme boundary conditions i.e fixed and free was simulated.

Equivalent free expansions

The expansion thresholds set by RILEM AAR-3 (Nixon and Sims, 2016), Norwegian test for ASR (Wigum, 2006) as well as the Dutch CUR recommendations (Vree et al., 2005) are valid only for laboratory tests conducted under free expansions. Hence the expansions obtained using fixed conditions cannot be directly compared with these thresholds. Thus, in order to find a comparable relation, the concept of equivalent free expansion was introduced in this study. Equivalent free expansion is defined as a parameter which determines the fictitious expansion under free boundary conditions when the same magnitude of load is applied under fixed boundary conditions.

It was explained previously that the forces required to generate the same crack fraction under different boundary conditions were different. By making the assumption that the crack densities evaluated using image analysis (refer table 3.4) represent the present condition of the structure under fixed boundary conditions, the total force generated for the fixed boundary condition was evaluated using fig 4.17 (b), fig 4.17 (d), fig 4.17 (f) for samples K22-16(2), K23-15(4) and K27-16(2) respectively. This force was used to evaluate their corresponding equivalent crack densities under free expansions using the same graphs. Equivalent crack densities for free expansions are nothing but the intersection of the generated force under fixed conditions and the response of force versus crack densities under free conditions for the specimen in question. Finally, knowing the equivalent crack densities for free expansions, their corresponding equivalent free expansion is calculated using fig 4.17 (a), 4.17 (c), 4.17 (e). The procedure is explained visually by taking example of K22-16(2) in fig 4.19. The complete data of equivalent free expansions for all the samples is presented in table 4.7. The expansion vs time curve was fitted in the exact same way as done for free expansions using the parameters from this table.

Sample	CD (%) (Fixed BC)	Force (N)	CD_{eq}(%) (Equivalent free expansion)	ε_y (Fixed BC)	$\varepsilon_{y_{eq}}$ (Equivalent free expansion)
K22-16(2)	3.71	26.02	5.61	9.9×10^{-5}	1.5×10^{-4}
K23-15(4)	4.70	37.37	8.6	1.24×10^{-4}	3.5×10^{-4}
K27-16(2)	1.28	23.65	1.71	2.7×10^{-5}	3×10^{-5}

TABLE 4.7: Data for equivalent free expansion and expansion under fixed conditions. These parameters are necessary to fit the expansion-time relation proposed by Karthik et al. (2016)

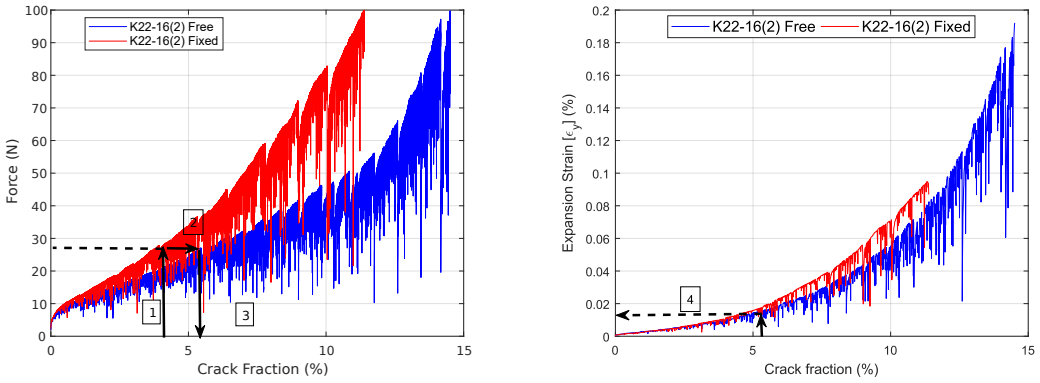

(a) K22-16(2): Force against crack fraction

(b) K22-16(2):Expansion strain against crack fraction

FIGURE 4.19: Procedure to calculate equivalent free expansions from fixed state. The procedure is highlighted using black arrows and their step numbers. step 1: Observed crack densities to force developed under fixed boundary conditions. Step 2,3 (left): Equivalent crack densities under free expansion for the same force. step 4 (right): Equivalent free expansion under free expansion for the equivalent crack densities evaluated in step 3.

The results presented in fig 4.20 serve as a predictive model for estimating the future expansion. These results are presented for the fixed boundary conditions. It showed that the expansions obtained by considering fixed boundary conditions were relatively on the lower side. This is reasonable as the restraints delay cracking and damage. However, the accelerated test standards are calibrated for the free expansions condition only and hence expansions under fixed conditions cannot be compared with the thresholds. Thus, the equivalent free expansions were calculated as a comparative parameter which are also presented in the same plot. It was observed that the worst affected sample K23-15(4) would reach the expansion threshold at 110 years (year 2042) according to CUR 89 recommendations and 190 years (year 2122) according to RILEM recommendations. Exceeding the expansion threshold value means that the aggregates are deemed to be

deleterious in terms of ASR damage but this does not necessarily mean a structural failure. Moreover, the presented results are valid for the most extreme boundary condition i.e full confinement. The realistic boundary condition lies somewhere between free and fixed and hence the equivalent expansion would decrease in that case. Thus, these results provide the most pessimistic scenario when it comes to boundary conditions.

The study of boundary conditions also goes to show that although the observed damage under confined state is not really visible, the force due to imposed deformations must be considered in the analysis to arrive at a right result. Alternatively, the standard tests must be modified to consider the effect of confinement by making the permissible expansion limits stricter for existing structures. One must also note that the coupling of other mechanisms was not considered in the study which could affect the results in an unpredictable way.

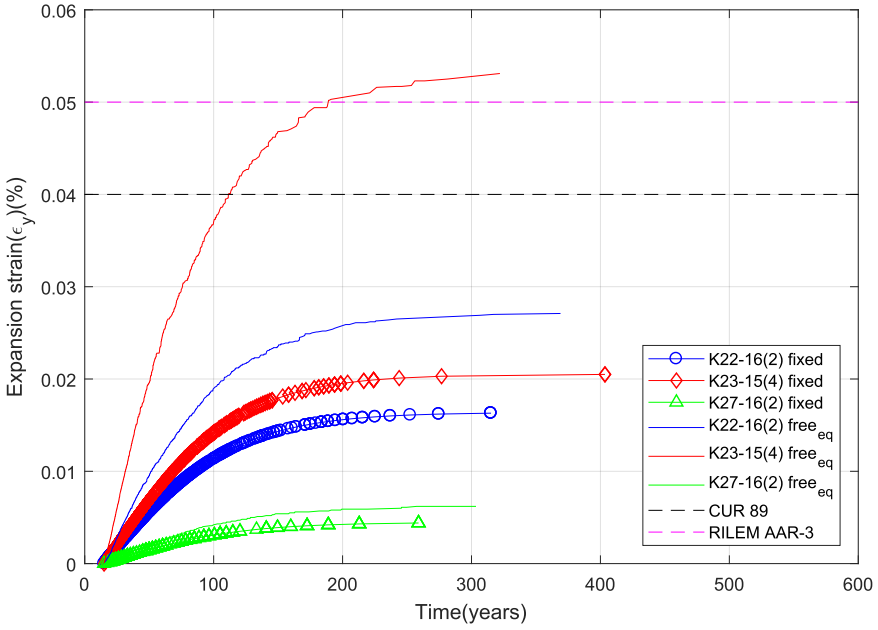

FIGURE 4.20: Progress of Expansion strains in time at the specimen level obtained by fitting lattice simulation data on the semi-empirical model by Karthik et al. (2016).The results are presented for expansion development under fixed boundary conditions and its equivalent free expansion. The permissible expansion thresholds from accelerated tests are also presented with dotted lines

Comparison of crack patterns

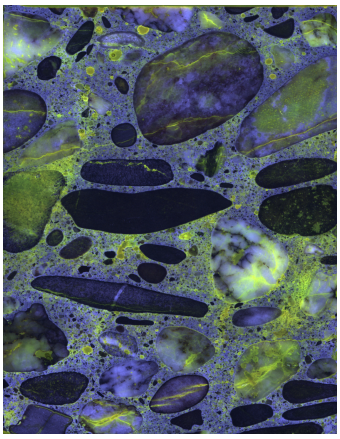

(a) K22-16(2) UV-image

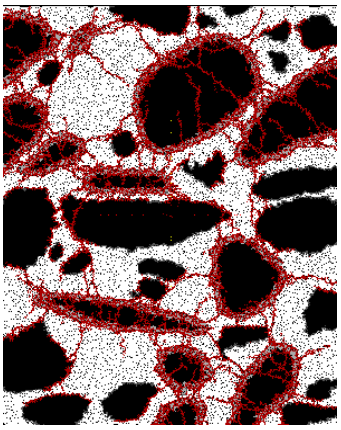

(b) K22-16(2), Free, Simulation Step 12000

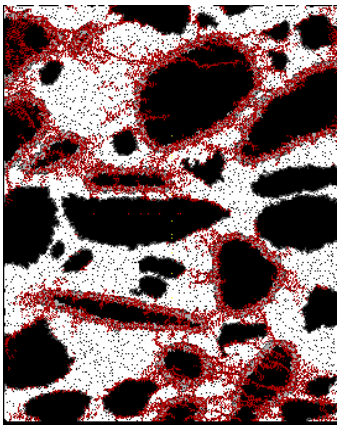

(c) K22-16(2), Fixed, Simulation Step 9800

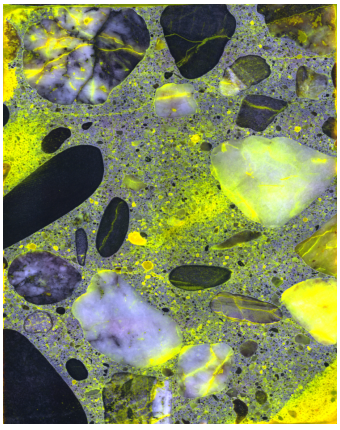

(d) K23-15(4) UV-image

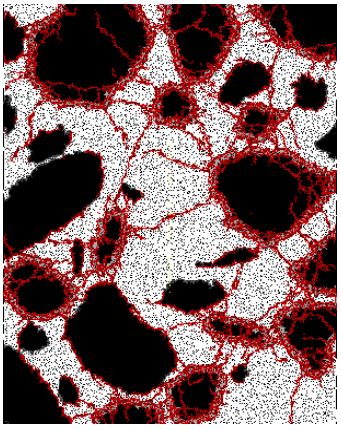

(e) K23-15(4), Free, Simulation Step 12000

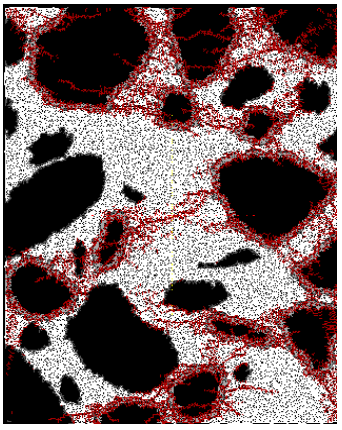

(f) K23-15(4), Fixed, Simulation Step 8000

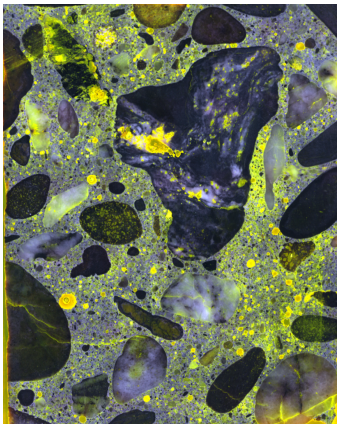

(g) K27-16(2) UV-image

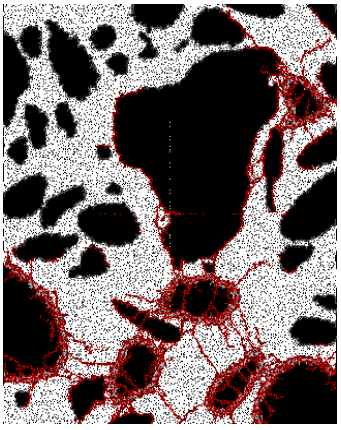

(h) K27-16(2),Free simulation Step 5425

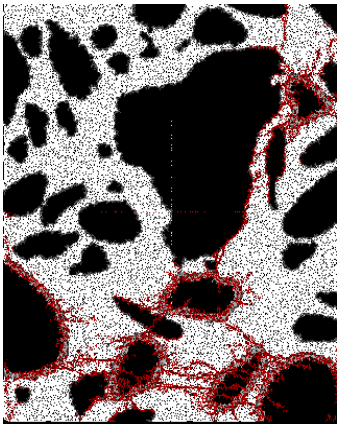

(i) K27-16(2), Fixed, Simulation Step 4000

FIGURE 4.21: Comparison of crack patterns produced using different boundary conditions against the UV image of the specimen.

The crack patterns for different boundary conditions is presented in fig 4.21. They are presented at a force of 100 N for both fixed and free boundary conditions. The propagation of cracks at different simulation steps for all the samples is presented in appendix G.

It was evident from fig 4.21 that the boundary conditions affected the crack propagation. The isotropic nature of cracking under free expansion against the anisotropic crack pattern was a characteristic observation. The presence of restraints on the vertical edges of the samples resulted in more cracks parallel to the horizontal axis. The cracks developed under the fixed conditions were more realistic as compared with free expansion. Thus, it implied that the fixed boundary condition was a more realistic boundary condition.

A lot of cracking was observed along the reactive rim which was not observed in the real sample. This was mainly due to the model assumption and the nature of loading associated with it. Furthermore, additional heterogeneity within the individual phases might result in more realistic crack patterns.

4.5.3 Mesh sensitivity

The dependence of the size of lattice mesh on the crack fraction (crack densities) was studied. A lattice mesh size of 1 mm, 0.5 mm and 0.25 mm was considered in the study. The study was performed on sample K22-16(2) for free expansions as free expansions were faster to compute. The radius of the mesh was calibrated for different sizes again using the same method described in the earlier subsections to adjust the elastic response. The mesh properties are presented in table 4.8. All the other parameters were kept constant.

Property	Lattice size		
	1 mm	0.5 mm	0.25 mm
Specimen size (mm)	74.41 x 95.38	74.41 x 95.38	74.41 x 95.38
Image size (Pixels)	75 x 95	151 x 191	302 x 380
Radius (mm)	0.54	0.26	0.11
Randomness	0.5	0.5	0.5
Number of nodes	7125	28841	114760
Number of elements	21003	86237	343991
Computational time	106 min	797 min	6.25 days

TABLE 4.8: Mesh properties for different lattice sizes

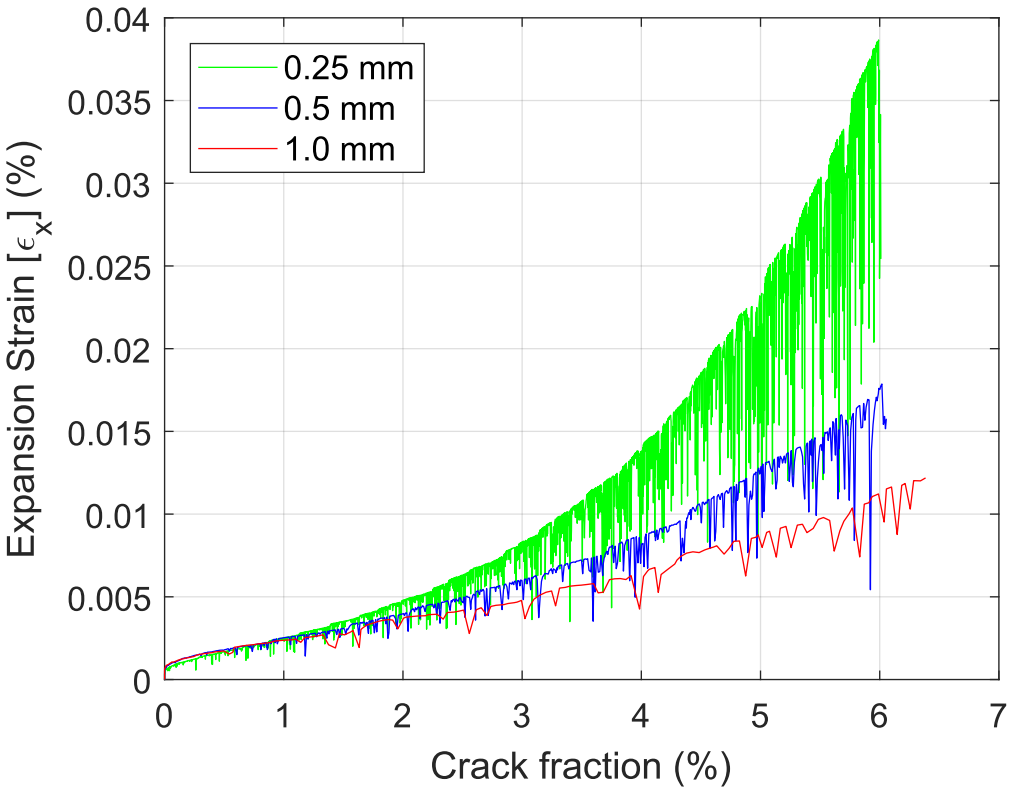

FIGURE 4.22: Sensitivity of mesh to crack fraction and expansions

It was clearly observed in fig 4.22 that the crack densities showed dependence on the mesh size. One of the reasons for this can be because of the way the mesh is generated and the interface (ITZ) in between defined. The aggregate and the mortar phase is scaled down with the same aspect ratio where as the ITZ always has a maximum width of one element for any mesh size. Thus, it is obvious that as the mesh size changes the phase fraction of individual phases also change. As the mesh grows finer, the relative phase fraction of the aggregates and the mortar increase whereas that of the ITZ decreases. Thus, for a coarser mesh, the size of ITZ occupies an unrealistically higher fraction in the model. ITZ being the weakest zone, plays a significant role in the fracture process as fracture processes start in this zone. However, its contribution to the relative stiffness is lower. Thus, a failed element in the interface contributes to lesser nodal displacements than a failed element in an aggregate or the mortar and consequently affects the expansions. This can be explained using fig 4.23. It is seen for the same crack fraction the sample with the coarsest mesh (1mm) consists of cracks only in its interface region. Whereas for the finest mesh (0.25mm), cracks are propagated in the mortar as well as the aggregates for the same crack fraction.

Furthermore, it was found out that for the same expansion strains, a comparable crack pattern was obtained for all the analysed mesh sizes. This is presented in fig 4.24. When

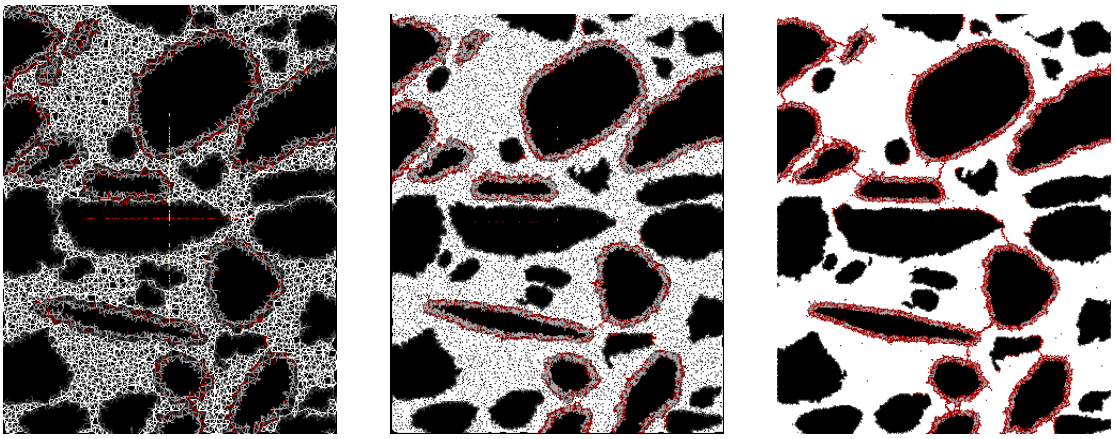

(a) Lattice size: 1 mm (b) Lattice size: 0.5 mm (c) Lattice size: 0.25 mm

FIGURE 4.23: crack patterns at 3% crack fraction for different mesh sizes

the expansion strains were compared, the percentage composition of the phases of the failed elements for different mesh sizes were also similar. This shows, that the mesh size is independent of the expansion strain values. Ideally, the expansion strain is the best comparable parameter between the model and the experiment. However, it is impossible to evaluate the expansions of the already damaged concrete cores without knowing its initial state. Therefore, another comparable parameter similar to crack density which can correlate with the expansions must be used.

Another reason for this sensitivity is also the way the crack fraction is calculated in this project. The crack fraction is always based on the number of damaged elements relative to the initial lattice. Different mesh sizes have different number of nodes. Addition of each node for a finer mesh results in addition of three new elements. For the crack fraction to remain constant, all the three elements must fail which is not generally the case. This leads to different crack patterns for the same crack fraction and consequently different expansion values. Since the crack patterns for the same level of expansion strains were similar, length of the cracks for the crack pattern might also be comparable. Thus, as an alternative, the deformed length of the failed elements (length of cracks) might prove to be a less sensitive parameter in relation to the mesh size. However, this parameter will still be mesh-dependent to an extent because of the effect of the ITZ size as explained earlier.

4.6 Model limitations

1. The lattice model is limited to only the mechanical effects of ASR. It does not consider the physio-chemical parameters involved in the reaction. The diffusion

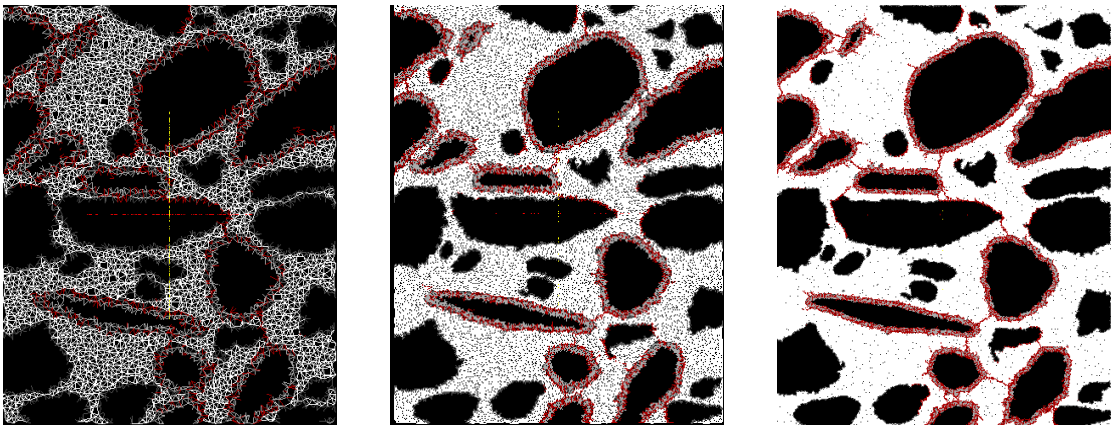

(a) Lattice size: 1 mm (b) Lattice size: 0.5 mm (c) Lattice size: 0.25 mm

FIGURE 4.24: crack patterns at expansion strain of 0.01% for different mesh sizes

controlled behaviour is only partially considered through the semi-empirical numerical model. Thus, the model does not provide true information on the reaction kinetics.

2. The model does not consider coupling of other degradation mechanisms like corrosion due to chloride ingress, freeze-thaw, Delayed ettringite formations etc. As seen from the literature, usually it is the coupling of various mechanisms along with ASR responsible for the failure of structural durability where ASR acts more or less as a catalyst.

3. The model is limited to expansions only at a material level. Up scaling the model to a structural level is another challenge in itself.

4. The model is restricted only to 2D expansions. However, the cracks also propagate in the third dimension contributing further to the expansion of the specimen. A complete 3D model though possible, will require very high computational processing.

5. The effect of restraint provided by the reinforcements is not considered in the simulations. However, the simulations provide information on the most extreme boundary conditions and thus covers the entire spectrum.

6. The model does not consider the swelling pressure exerted by the ASR gel inside the cracks. This quasi-static condition could result in higher expansion strains.

7. The model is limited to only petrographic features as a comparative parameter. The main reason being the unavailability of expansion data in time. Moreover, the parameter crack fraction was found to be mesh dependent.

4.7 Prospective study for the future

A preliminary analysis was performed to relate the expansion-time curve to the degradation of mechanical properties. Such a study could provide an input for models at a structural level and help in upscaling the model. Since fixed boundary condition was found to be more realistic, the expansion-time curve obtained from the fixed boundary conditions as seen in fig 4.20 was used in this subsection. The expansion corresponding to a time period of 85, 100, 150 and 200 years was considered to observe the degradation of Young's modulus under ASR loading. The step corresponding to the expansion at these data points was determined and using this as the initial lattice a direct tension test as explained in section 4.4.1 was simulated. The elastic modulus was calculated in the same way as explained in section 4.20. The degradation of elastic modulus was compared with the results obtained from the test performed in Chapter 4. The results are presented in fig 4.25.

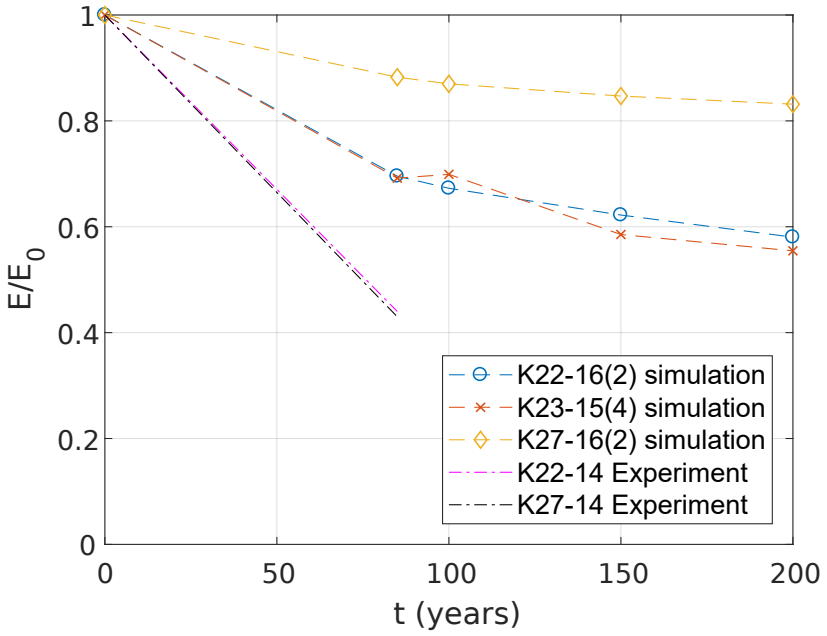

FIGURE 4.25: Decay of Young's modulus (E) in time. The graph is normalised for better visibility.

It can be seen that the results from the experimental don't conform to the results from the model simulations. There are a number of reasons for the discrepancy. The primary reason being the mesh-size sensitivity. This indicates that the current mesh size may not be the appropriate size. However, other parameters like length of the cracks may result in a better conformation of the results. The number of data points and test results are also limited and thus, the model cannot be validated with the given data set. With a

better experimental programme and the recommended adjustments to the model could make this a promising study.

4.8 Chapter summary

1. Alkali silica reaction was realised in the lattice model by making use of local internal tensile forces randomly distributed over reactive rim of the aggregates.

2. Approach two using the bi-linear constitutive law to simulate time-dependent behaviour resulted in higher expansion strains compared to the linear-elastic model. The obtained crack patterns were also comparable to each other.

3. The model was able to simulate localised cracks. The observed crack patterns had isotropic directions for the case of free expansion simulations instead of horizontal parallel cracks observed in actual samples. This can be attributed to the lack of restraints (along the boundaries only) allowing expansions in all directions. Moreover, it proved that the crack patterns depend significantly on the boundary conditions.

4. Crack densities were used to compare the simulations with the actual samples. Initially, it was assumed that the crack densities calculated from the actual samples were comparable to the crack densities obtained from the simulations under free expansions. However, this was not realistic as it was already seen that the crack patterns and force distribution depend on the boundary conditions. Thus, the study was extended to include fixed boundary conditions to draw better conclusions.

5. Simulations under fixed conditions resulted in more realistic crack patterns as compared to the actual specimen. Observed crack patterns were horizontal and parallel to the direction of the reinforcement.

6. Study of boundary conditions also revealed how the internal force varied for different boundary conditions. For the same crack fraction, the expansion generated in the less compressed side of the simulations with full restraint was higher than that of free expansions along the same direction. This was attributed to the effect of Poisson which reiterated the 'expansion transfer' concept proposed by Multon and Toutlemonde (2006). It was also revealed that a significantly higher force was required for the fully restrained state to reach the same crack fraction as that of free expansions. This implied, that the overall cracking was delayed because of the effect of confinement. This was further evident in the load-displacement curves which showed lower damage for the fixed state as compared to the free expansions.

7. The expansion vs time curves were plotted for free expansion as well as the fixed state. For the later, a comparable parameter called 'equivalent free expansions' was introduced since the accelerated tests are only calibrated for free expansions. It was realised that assuming free expansions as the real boundary condition led to erroneous and optimistic results. The equivalent free expansions obtained from the fixed boundary conditions were mostly within the expansion thresholds except for the most damaged sample. This indicated that the aggregates used in the Afslutidijk are potentially deleterious.It is to be noted however, the mesh size considered to draw this conclusion was 0.5 mm which was chosen based on computational feasibility. However the sensitivity of crack fractions discussed in the next point prove these results to be unreliable.

8. The size of mesh was found to influence the crack fractions and expansions. Thus the result obtained for 0.5 mm cannot be considered to be reliable. A thorough sensitivity is necessary in future to draw better conclusions on an optimum size of the mesh. Alternatively, crack lengths could prove to be a less sensitive parameter.

Chapter 5

Conclusions and Recommendations

5.1 Conclusions

Based on the petrographic investigation and numerical modelling some conclusions were drawn. They are presented below in two separate parts.

Materials characterisation

1. Polarised light microscopy confirmed damage in the existing concrete cores due to expansions caused by Alkali-Silica reaction even though no macro-cracks were visible. The study confirmed presence of potentially reactive coarse aggregates (for ASR) and provided information on their relevant mineralogy.

2. Microscopic techniques prove to be good forensic tools to investigate the type of cement and quantify the proportion of various phases in concrete. These techniques can be further used to estimate the original mix design of hardened concrete.

3. The technique used to estimate water-cement ratio in hardened concrete showed great deal of variation and depends to great extent on lighting and exposure conditions as well as sample preparation. This technique must be investigated further to provide uniform results.

4. Damage rating index test using UV light is a cheap and an effective tool to quantify damage features for ASR in existing structures. It provides an easy alternative to distinguish between relative degree of damages at different locations and classify various ASR micro-structural features to know how the damage is propagating. It

is essentially a simple tool to monitor damage propagation due to ASR for existing concrete structures.

5. Crack quantification using image analysis which is an alternative tool to DRI proved to be more automated and involved relatively lower user bias. However, it fails to distinguish between ASR affected cracks and other type of cracks making its use limited. Moreover, it was found that the analysis depended to a great extent on preparation of sample surface, exposure conditions and image segmentation techniques.

6. There was a strong correlation between DRI and crack densities using image analysis. This shows that both the methods in spite of having their own drawbacks, are able to quantify relative damage in a similar range.

ASR expansion model

1. The ASR expansion model is a simplistic model which tries to correlate the damage (physical distress) from petrographic investigation to expansion strains. This model approach attempts to make an estimate over potential future expansions at a material level which could be useful to plan maintenance activities.

2. The model is able to simulate localised network of cracks which are typical of ASR. Full confinement provided more realistic crack patterns.

3. The propagation of cracks and expansion strains depend to a great extent on the boundary conditions. Appropriate boundary conditions must be considered to estimate realistic strain values.

4. The expansion model executed to study expansions in the Afsluitdijk resulted in strains below the permitted threshold for all the samples considering the present condition. Whereas, for the most damaged sample, the expansion strains were predicted to surpass the permissible expansion limit deeming the aggregates to be deleterious for ASR. This study was performed for a mesh size of 0.5mm which may not be realistic due to mesh sensitivity discussed in the next point.

5. A mesh-sensitivity study revealed the dependence of crack fraction on the size of the mesh. This affected the expansion strains which would eventually influence the expansion-time curve. The variation of the phase fraction of the ITZ to other phases and the method of calculating crack fraction based on the initial lattice were cited to be the main reasons for this effect. Thus, to conclude crack fraction may not be the best comparable parameter.

5.2 Recommendations

1. Although the model established that the present condition of the structure in terms of ASR damage is sound (when compared to expansion thresholds), the aggregates were deemed to be deleterious in the future. Moreover, the mesh sensitivity study revealed that the results of the model may not be reliable. Additionally, the Young's modulus determined from the test results was significantly low. Thus, preventive steps like monitoring of the damage must be undertaken. The damage rating index method proves to be an inexpensive method which can be used every several years to analyse the extent and rate of crack propagation. This would serve to make better decisions for the Asset owners.

2. Since a linear correlation between image analysis and DRI was obtained, a study can be undertaken to automate DRI using image analysis which would make the whole procedure faster.

3. The estimated mix design of concrete could be used in the future to cast the concrete and perform accelerated tests. This could provide more data points in the expansion-time curve to validate the model and adjust the parameters.

4. Since boundary conditions played an important role in the expansions, The guidelines should consider their effect when it comes to assessing existing structures. Since, performing laboratory tests on different boundary conditions is not easy, the concept of equivalent free expansion could prove to be useful in adjusting and calibrating the laboratory tests and current standards for the assessment of ASR affected structures.

5. Presence of reactive aggregates is a concern for structural durability since the coupling of mechanisms is not considered. A future study to combine various mechanisms and considering physio-chemical parameters like the effect of temperature, moisture, alkali concentration and diffusion would enhance the existing model.

6. In future, a study to take into account the effect of restraints provided by the reinforcement instead of a full restraint could help to fine tune the model and make it more realistic.

7. A thorough mesh sensitivity study must be performed to draw conclusions on the dependence of crack fraction on the mesh size. Parameters like length of the cracks can prove to be a better alternative as compared to crack fractions in terms of mesh-size dependency.

8. After addressing the limitations of the model mentioned earlier a study could be conducted in the future to predict the change in the elastic properties due to ASR. This could prove to be a good input for structural modelling.

Appendix A

Point counting and image analysis data

Coarse aggregates

The total counts of coarse aggregates in the sample were counted manually using an overlaid grid as per ASTM C457. In case of any discrepancy in determining whether the point (marker) hits the aggregate on the grid, a general rule was defined before the counting. For instance, if the boundary of the coarse aggregate lay on either the right or the bottom side relative to the location of the marker in question for that particular square grid then the point was recorded as a coarse aggregate. This rule was maintained throughout the process to maintain consistency, minimise counting errors and improve the reliability of the results. The results are presented in table A.1

The average value was calculated as a global value representative of the chosen structure. Average value was calculated by considering the total counts calculated per sample as its weight.

$$\%Coarse\ aggregates_{Avg} = \frac{\sum Total\ counts \times \%Coarse\ aggregates}{\sum total\ counts}$$

Sample	Area (mm^2)	Total counts	counts/area	Course Aggregates (Counts)	Coarse Aggregates (%)	Mortar (Including voids) (%)
K27-16 (1)	6586.2206	425	0.0645	199	45.98071	54.01929
K27-16 (2)	6112.9586	396	0.0648	204	51.51515	48.48485
K27-16(3)	7833.8448	513	0.0655	238	45.76513	54.23487
K26-14(2+3)	9051.48	589	0.0651	267	45.33107	54.66893
K26-14(4)	6828.543	450	0.0659	234	52	48
K23-13(2)	6388.09	414	0.0648	206	49.01208	50.98792
K23-13(3)	7080.2667	456	0.0644	175	38.37719	61.62281
K23-15(2)	5726.438	384	0.0671	161	41.92708	58.07292
K23-15(3)	6420.3564	391	0.0609	179	44.84248	55.15752
K23-15(4)	5891.1935	391	0.0664	193	49.36061	50.63939
K22-16 (2)	7226.0034	456	0.0631	270	58.19566	41.80434
K22-16 (3)	6282.225	408	0.0649	180	43.36147	56.63853
Average	6282.225	408	0.0649		47.12	52.88

TABLE A.1: Point counting-Coarse aggregates data

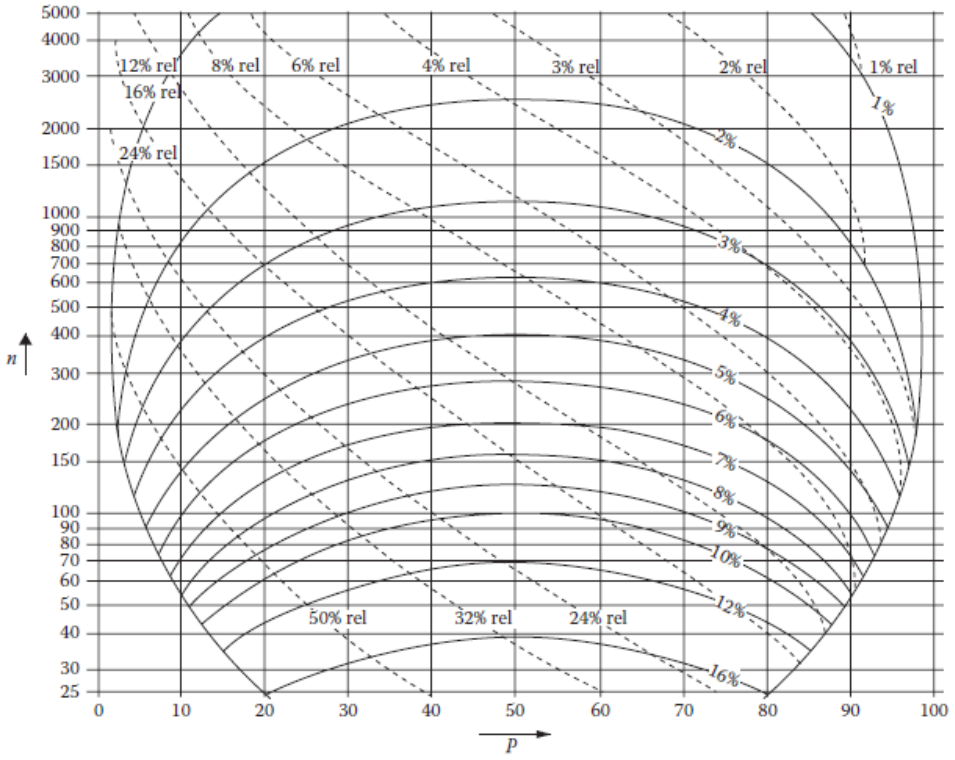

FIGURE A.1: "Chart for estimation of error in point counting.The total number of points n counted on the specimen is shown on the y-axis and the percentage P of a component on the x-axis. At the intersection point of n and P, the relative error is read from the dotted lines and standard deviation at 95% probability from solid curved lines" (Poole and Sims, 2015)

Fine aggregates, paste and air voids

The area fractions of different phases was worked out using image analysis on separately segmented images. The table A.2 shows in detail the data obtained from image analysis. The images were scaled to the actual size of the samples and the area occupied by the pixels was automatically converted to mm^2 by the image analysis program. However, these values were true only for the thin section. These values were later normalised to the actual concrete composition worked out in table 3.11.

	Image Analysis of thin sections								Normalised Values	
Sample	Total Area (mmˆ2)	FA (%)	Area FA (mmˆ2)	CA (%)	Area CA (mmˆ2)	Air Void (%)	Air Content (mm2)	Mortar (%)	FA (%)	Paste (%)
K27-16 (1)	1350	17.695	236.327	51.46	688.143	1.80	24.65	48.54	36.45	63.55
K27-16(3)	1350	16.43	239.3	46.862	682.921	1.36	18.29	53.14	30.92	69.08
K23-13(2)	786.9	23.105	181.84	41.23	324.439	1.50	11.80	58.77	39.31	60.69
K23-15(3)	1261.3655	11.75	148.21	63.977	806.984	2.05	25.83	36.02	32.62	67.38
K22-16 (2)	995.4	18.985	188.953	51.2	503.591	1.71	17.06	48.80	38.90	61.10
K22-16 (3)	1232.301	18.483	227.766	52.516	647.191	1.71	20.71	47.48	38.92	61.08

TABLE A.2: Composition of thin sections

The mortar phase in the thin sections is worked out in the following way. Mortar is composed of fine aggregates and paste.

$$Mortar(\%) = 100 - CA(\%) \tag{A.1}$$

With this information, the absolute value obtained from thin section is normalised to 100 in the following way:

$$FA_{Normalised}(\%) = \frac{FA(\%) \times 100}{Mortar(\%)}; \tag{A.2}$$

$$CA_{Normalised}(\%) = 100 - FA_{Normalised}(\%) \tag{A.3}$$

Finally, knowing the composition for a small area of thin sections and assuming that the thin section area is representative of its corresponding polished section, this composition is extrapolated to the polished section based on the initial composition worked out in table 3.11. Air voids are calculated in a similar way. The final set of results at the level

of polished sections is presented in table A.3. The paste-aggregate ratio is also worked out based on the volumetric compositions.

Sample	Area (mm^2)	Air void (%)	CA (%)	FA (%)	Paste (%)	Paste/Agg
K27-16 (1)	6586.2206	1.8	45.98	19.34	33.71	0.73
K27-16(3)	7833.8448	1.4	45.77	16.54	36.96	0.81
K23-13(2)	6388.09	1.5	49.01	19.74	30.48	0.62
K23-15(3)	6420.3564	2.0	44.84	17.62	36.41	0.81
K22-16 (2)	7226.0034	1.7	58.20	15.98	25.10	0.43
K22-16 (3)	6282.225	1.7	43.36	21.67	34.00	0.78
Avg	6789.4567	1.7	47.86	18.48	32.78	0.70

TABLE A.3: Volumetric composition of the concrete cores

Damage Rating Index

	Absolute Values								Weighted Values						
Sample	CCA	OCCA	CCAG	CAD	CCP/CCPG	Total	Area(cm^2)	Normalised counts	CCA	OCCA	CCAG	CAD	CCP/CCPG	DRI	Crack Density (counts/cm^2)
K22-16(2)	54	88	14	11	39	206	71	290	19.01	247.89	39.44	46.48	164.79	518	2.14
K22-16(3)	25	25	5	18	70	143	73.37	195	8.52	68.15	13.63	73.60	286.22	450	1.61
K23-13(2)	51	31	3	14	34	133	67.92	196	18.77	91.28	8.83	61.84	150.18	331	1.21
K23-13(3)	32	29	1	6	47	115	71.8	160	11.14	80.78	2.79	25.07	196.38	316	1.16
K23-15(2)	24	33	1	8	64	130	59.93	217	10.01	110.14	3.34	40.05	320.40	484	1.77
K23-15(3)	44	28	13	6	86	177	68.72	258	16.01	81.49	37.83	26.19	375.44	537	1.94
K23-15(4)	44	64	9	13	60	190	60.13	316	18.29	212.87	29.94	64.86	299.35	625	2.43
K23-16(4)	28	34	13	3	39	117	68.81	170	10.17	98.82	37.79	13.08	170.03	330	1.29
K27-16(1)	19	16	10	6	46	97	65.67	148	7.23	48.73	30.46	27.41	210.14	324	1.19
K27-16(2)	27	13	5	4	22	71	58.38	122	11.56	44.54	17.13	20.55	113.05	207	0.75

TABLE A.4: Damage rating index counting data

Appendix B

Image segmentation protocols

Segmentation of paste, fine aggregates and coarse aggregates

The distinct contrast between aggregates and paste in a plane polarised thin section image made image segmentation not only accurate but reproducible. A flow chart is presented in fig to provide the protocol used to segment the image.

The 8 bit image contains grey-scale values between 0 and 255. The histogram as shown in fig B.2 produced 2 prominent peaks. One indicative of the mortar phase and other of the aggregates phase (Fine as well as coarse aggregates). A grey scale value was therefore chosen to create a binary image. In the example presented in fig B.2, a grey scale value of 149 was chosen to create a binary image. The created binary image had minor faults. These included small holes in between the aggregates due to variation of colours, connected aggregates etc. These were corrected by means of inbuilt binary functions. These included 'fill holes', 'dilation' and 'erosion'. The process was continued until a binary image devoid of these faults was obtained. Finally, smooth masks were created for quantification.

The second part of the segmentation was based on size of the aggregates defined as area. An aggregate was considered to be a fine aggregate if the area occupied by its mask was less than 12.5 mm^2 (Assuming the particle to be a circle with a diameter of 4mm). The remaining masks were considered as coarse aggregates. Particle analysis was then performed separately on coarse and fine aggregates.

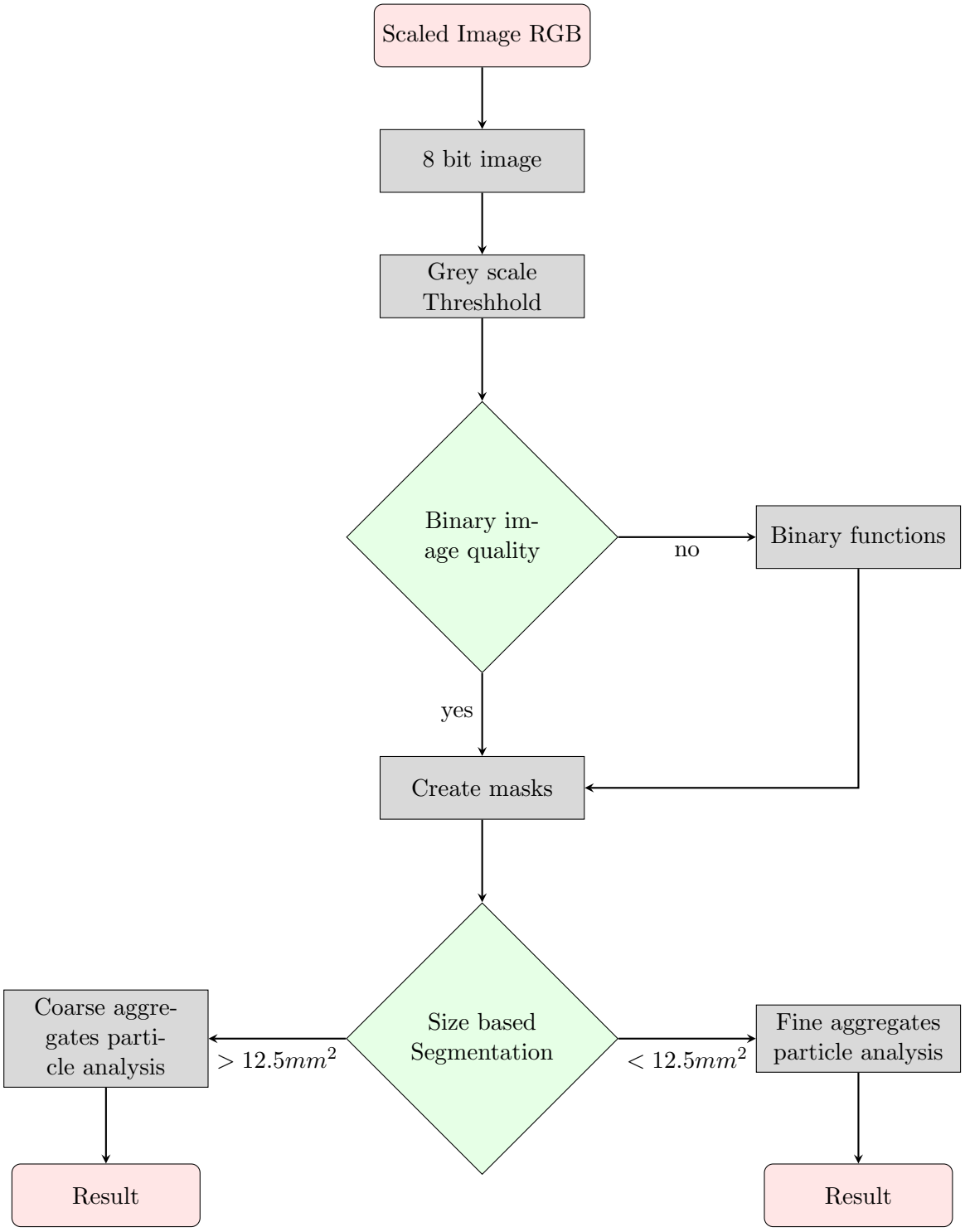

FIGURE B.1: Image Segmentation protocol to determine area compositions

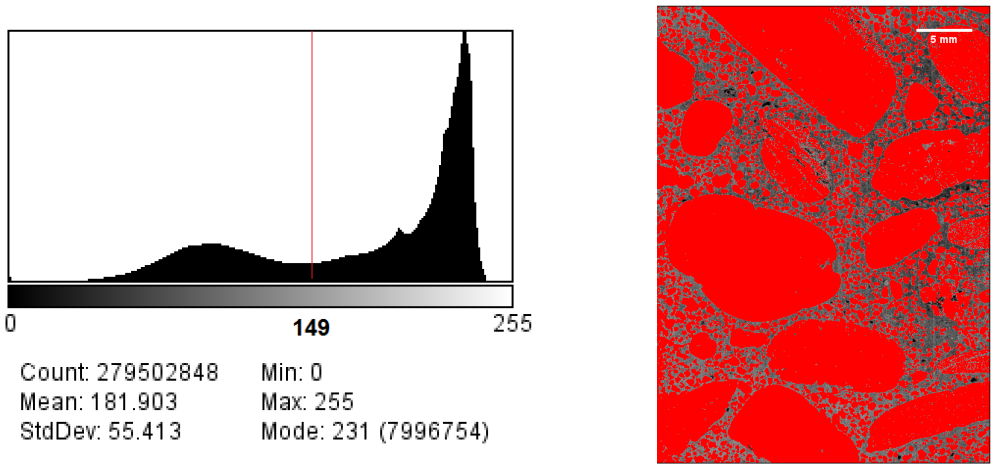

(a) (b)

FIGURE B.2: K22-16(3): (a) Histogram of grey scale image. (b)Thresholding based on the normal distribution

Segmentation of air voids

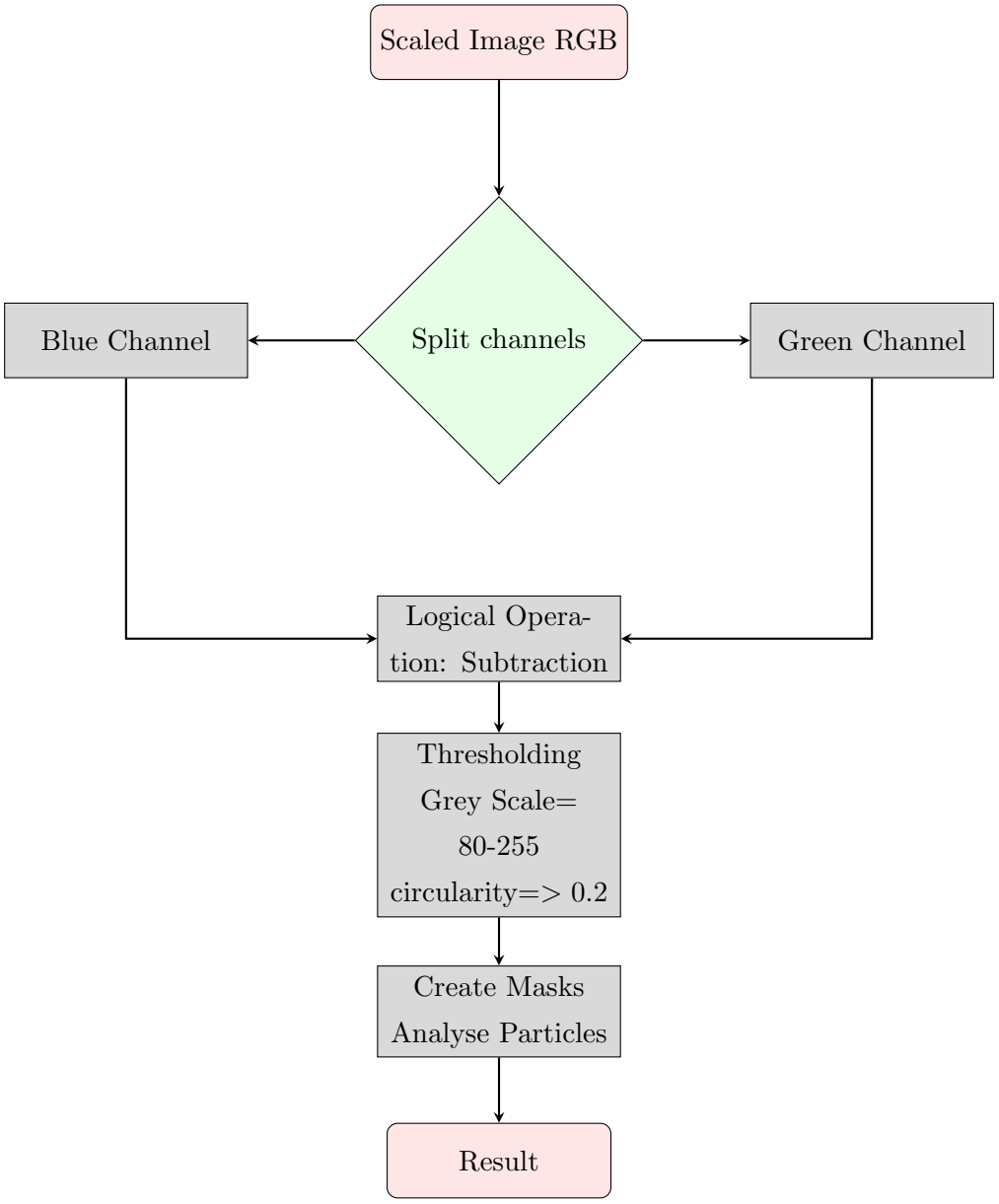

FIGURE B.3: Image segmentation protocol for air voids

The voids and cracks in the polished section were distinct as compared to the matrix since they were always filled with yellow coloured epoxy. The yellow colour was effectively segmented by subtracting the green channel from the blue channel. The cracks were further distinguished from the voids based on the circularity of the masks. A circularity of 1 represents perfectly rounds masks whereas a circularity of 0 represents a completely elongated shape. It was found that a circularity of > 0.2 could effectively separate out cracks from voids.

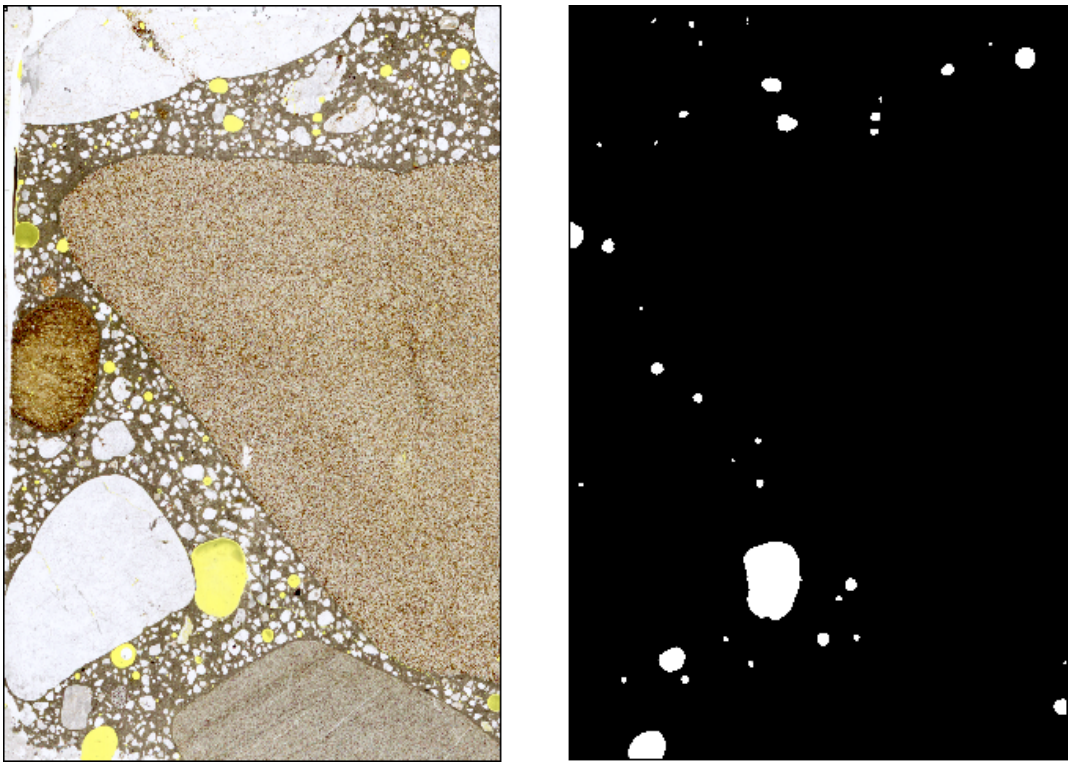

(a) (b)

FIGURE B.4: K23-15(3) (30x45mm): (a) PPL image in RGB. (b)Segmented Binary image showing air voids

Segmentation of Cracks

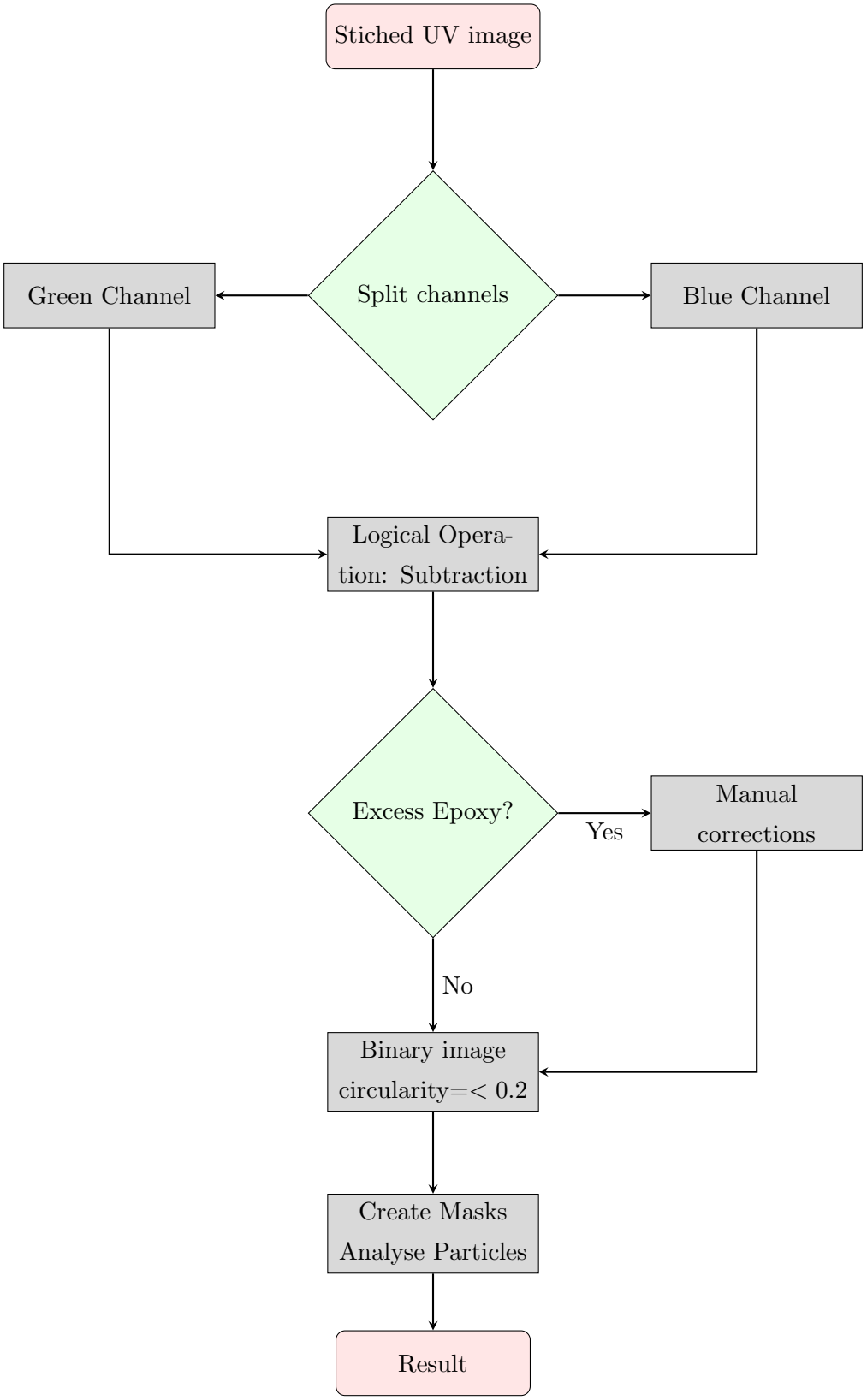

FIGURE B.5: Image segmentation protocol for cracks

The quality of segmentation depended on the evenness of sample preparation. The better the polishing and removal of excess epoxy, better is the final segmented image. As the epoxy within the cracks and the excess epoxy due to unevenness of the sample surface had similar intensity of the colour, thresholding the image became difficult. Some manual corrections were applied to remove the excess epoxy in the image. This was achieved using blow/lasso tool and wand tool. Instead of a conventional mouse, a 'Wacom-Bamboo' digital sketchpad yielded better accuracy in choosing the required areas. Using the flood tool, these areas were changed to the colour of the matrix.

Segmentation protocol for lattice microstructure

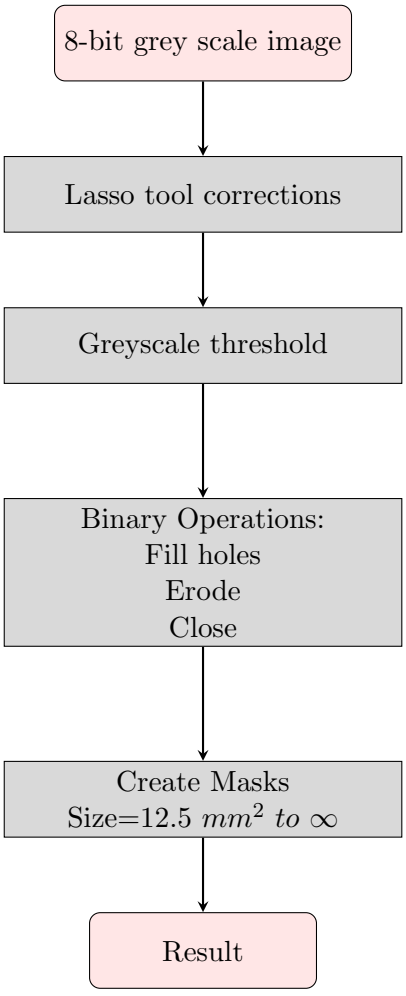

FIGURE B.6: Segmentation to create lattice microstructure

The image segmentation protocol for obtaining the microstructure was quite linear. An 8-bit grey scale image had aggregates of varying intensity. Some exhibited grey scale intensity lower than the mortar phase, while others were higher than the mortar phase making it impossible to threshold the image automatically. Thus, 8-point connected

Lasso tool was used to convert the lighter aggregates to a pixel value corresponding to intensity of black. This manipulation made it possible to apply a threshold. The obtained binary image had undesirable features like small holes in the aggregates, connected aggregates etc. Binary operations like 'fill holes', 'erode' and 'close' were used to get over these features. Finally the aggregates were masked and a size filter of 12.5 mm^2 was applied to get rid of fine aggregates.

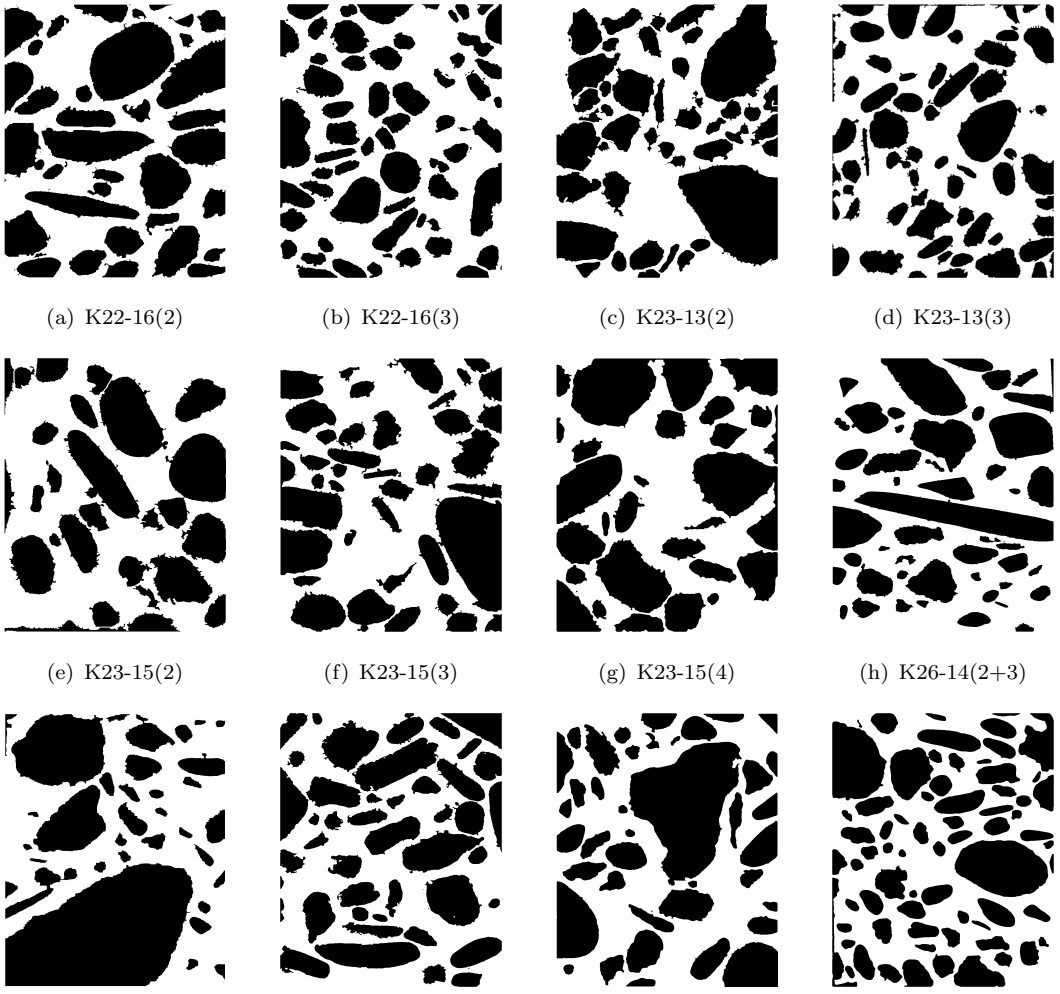

(a) K22-16(2) (b) K22-16(3) (c) K23-13(2) (d) K23-13(3)

(e) K23-15(2) (f) K23-15(3) (g) K23-15(4) (h) K26-14(2+3)

(i) K26-14(4) (j) K27-16(1) (k) K27-16(2) (l) K27-16(3)

FIGURE B.7: Binary images obtained after using the segmentation protocol. These are used as an input to the lattice model

Appendix C

Matlab codes

Distribution of internal loads randomly

```
%Assigning LLD only to reactive rim of aggregates (tag 3)
% Originally script by CANER ANAC % 26-02-2014
% Revised 18/05/17 By Ameya Kamat
% Creating new Initial LLD file with Given number of loading elements based
% All the reactive zones be assigned an internal expansion force,
% Edge elements not loaded for better convergence. Set the margin.
%
rw=0;
clear ;
Def=1;                  % Force for reactive phase (INPUT HERE) in kN
ReaFac=0.2;             %factor of reactivity (Here 20%=0.2)
disp('Creating  LLD file')
Margin=2;    %Draw a margin for the load to be applied, avoid load on edges
lx=75;       %size of model x
ly=95;       %size of model y

%Read data from ELE file
%Change the columns for approach 2.
fid4=fopen('example.ele','r');          % load Element (ELE) file
elements=fscanf(fid4,'%f',[19 inf]);    % Assign all to Matrix elements
elements=elements';                     % Transpose Elements
initial=elements;
ElementNodes=elements(:,2:3);          %Extract element nodes;
elementTAG=elements(:,19:19);           %Extract element tags
elementNO=elements(:,1:1);
fclose(fid4);                           % Close ELE file
%-------------------------------------------------------------------------
%Read NOD file
fid9=fopen('example.nod','r');
Nodes=fscanf(fid9,'%f',[5 inf]);        % Assign all to Matrix elements
Nodes=Nodes';                           % Transpose nodes
fclose(fid9);
% NoE=length(D);                       % enter the number of elements
% i=1;
```

```
 tgc1=1;
 EleNo_Tag=horzcat(elementNO, elementTAG);  %vector with element no. and tag
 NoE=length(EleNo_Tag)  %Numbe of elements
% Sort out only the reactive phase (tag 3)
 for i=1:NoE
 if(EleNo_Tag(i,2)==3)
     RA(tgc1)= EleNo_Tag(i,1);
     tgc1=tgc1+1;
 end
 disp(i/NoE*100);
 end
RA=RA';
ReaEle=round(length(RA)*ReaFac,0) % total number of reactive locations (20%)
%Start of random distribution algorith
O=ones(length(RA),1);
O=O*Def;                              %create a vector with force magnitude
LLD=RA;
DummyR1 = randn([length(LLD)],1);    %Create random numbers
LLDRnd=sortrows([RA,DummyR1],2);     %arrange the elements randomly
% Avoid loading on edges by giving them pseudo force of 10kN and then
% sorting them out of the system
LLDRnd=sortrows(LLDRnd,2);
for i=1:length(LLDRnd)
if Nodes(ElementNodes(LLDRnd(i,1),1),2)<Margin
    LLDRnd(i,2)=10;
elseif Nodes(ElementNodes(LLDRnd(i,1),1),2)>(lx-Margin)
    LLDRnd(i,2)=10;
elseif Nodes(ElementNodes(LLDRnd(i,1),2),3)<Margin
    LLDRnd(i,2)=10;
elseif Nodes(ElementNodes(LLDRnd(i,1),2),3)>(ly-Margin)
    LLDRnd(i,2)=10;
end
end
disp('Tag 3 Sorted');
LLDRnd=LLDRnd(1:ReaEle,:); %Only choose the reactive locations from the vector
w=1;
q=1;
for q=1:ReaEle

LLDrnd1(w)=LLDRnd(q,1);
w=w+1;
end
LLDrnd1=LLDrnd1';
LLDrnd1=sortrows(LLDrnd1,1)
%End of random distribution algortihm
%---------------WRITE TO FILE-----------------------------------------------

fid7=fopen('aftot.lld','w');
for i=1:length(LLDrnd1)

            fprintf(fid7,'%.8g %f',LLDrnd1(i,1),Def);
            fprintf(fid7,'\n');
end
fclose(fid7);
disp('LLD file Generated');
```

```
90
91 %clear
```

Computation of expansion strain and strain fields

```
1  %By Ameya Kamat (23/06/17)
2
3  %Computing strains and displacements for all steps
4  %
5  %
6  rw=0;
7  clear ;
8  %%INPUT PARAMETERS%%
9  %Copy all the dpf files from output in the post-processing folder, note down the
       end step.
10 %Enter size of the model in x and y. (size of the picture in pixels)
11 %ALways run the damaged elements file before if interested in a damaged
12 %elements plot.
13 lx=151; %size in pixels in x direction
14 ly=191; %size in pixels in y direction
15 NOE=86237; %Number of elements
16 Lattice_Size=0.5; %Size of mes
17 %Enter the last step
18 end_step=40475; %Final step in the simulation (Check dpf files)
19
20
21 p=25;
22 in=2;
23
24 str1='aftot_';
25 str3='.dpf'
26 for p=25:25:end_step  %Change the interval of steps based on your output.
27
28 str=strcat(str1,num2str(p),str3);
29 fid4=fopen(str,'r');                    % load displacement field (dpf) file
30 disp_field=fscanf(fid4,'%f',[8 inf]);  % Assign all to Matrix elements
31 disp_field=disp_field';                 % Transpose Elements
32 initial=disp_field;
33
34 %%%%%%%%%%%%%%%%%%%%%%%%%%%%%%%%%%%%%%%%%%%%%%%%%%%%%%%%%%%%%%%%%%%%%%%%%%%%%%%
35  fclose(fid4);                           % Close DPF file
36  i=lx;
37  j=1;
38  tgc1=1;
39  tgc2=1;
40  tgc3=1;
41  tgc4=1;
42 %  EleNo_Tag=horzcat(elementNO, elementTAG);
43  NoN=length(disp_field) ;
44 % %Extract only the right edge nodes
45   for i=lx:lx:NoN
46      Right_Edge(tgc1,:)=disp_field(i,:);
```

```
47        tgc1=tgc1+1
48  %
49    end
50
51    % %Extract only the left edge nodes
52
53    for j=1:lx:NoN
54       Left_Edge(tgc2,:)=disp_field(j,:);
55       tgc2=tgc2+1
56  %
57    end
58    %% %Extract only the tope edge Nodes
59    TN=Left_Edge(length(Left_Edge),1);
60    k=TN;
61     for k=TN:NoN
62       Top_Edge(tgc3,:)=disp_field(k,:);
63       tgc3=tgc3+1
64  %
65     end
66
67     %% %Extract only the bottom edge Nodes
68     l=1;
69     for l=1:lx
70       Bottom_Edge(tgc4,:)=disp_field(l,:);
71       tgc4=tgc4+1
72     end
73   % Compute strain fields x dir
74  Displacement_xx=Right_Edge(:,3)-Left_Edge(:,3);
75  Strain_xx=Displacement_xx/(lx*Lattice_Size);
76  Avg_strain_xx(in)=sum(Strain_xx,1)/length(Strain_xx);%Average strain
77   % Compute strain fields y dir
78  Displacement_yy= Top_Edge(:,4)-Bottom_Edge(:,4);
79  Strain_yy=Displacement_yy/(ly*Lattice_Size);
80  Avg_strain_yy(in)=sum(Strain_yy,1)/length(Strain_yy);%Average strain
81
82  Steps(in)=p;
83  in=in+1;
84   disp(p/end_step*100);
85
86  end
87
88  Avg_strain_xx=Avg_strain_xx';
89  Avg_strain_yy=Avg_strain_yy';
90  Steps=Steps';
91  %Write to a text file
92  Strain_field=horzcat(Steps,Avg_strain_xx,Avg_strain_yy);
93
94  fid7=fopen('Strain_field.txt','w');
95   for i=1:length(Strain_field)
96
97                fprintf(fid7,'%.8g %g %f ',Strain_field(i,:));
98               fprintf(fid7,'\n');
99
100   end
101 fclose(fid7);
```

```
%%

fid5=fopen('dam_ele.txt','r');              % load Element (ELE) file
dam_elements=fscanf(fid5,'%f',[2 inf]);
dam_elements=dam_elements';
Damaged_steps=dam_elements(:,2);
fclose(fid5);

Crack_Per_dam=Damaged_steps/NOE*100;        %crack fraction

%-------Strain vs damaged elements only----------------------------
% Only for approach 2
% plot(Damaged_steps,Avg_strain_xx*100,'b',Damaged_steps,Avg_strain_yy*100,'r');
% grid on;
% box on;
% xlabel('Damaged Elements');
% ylabel('Strain (%)');
% legend('Strain xx','Strain yy');


%-------Strain vs % Cracks--------------------
plot(Crack_Per_dam,Avg_strain_xx*100,'b',Crack_Per_dam,Avg_strain_yy*100,'r');
grid on;
box on;
xlabel('Crack fraction (%)');
ylabel('Expansion Strain (%)');
legend('\epsilon_{xx}','\epsilon_{yy}');
disp('Strain field created');

%----------Write it to a text file-----------------
%% For Comparing plots with other cases.
str4='.txt';
str67='_for_plot';
strA=strcat(str1,'_for_plot',str4);
for_plot=horzcat(Crack_Per_dam,Avg_strain_xx*100,Avg_strain_yy*100);
fid8=fopen(strA,'w');
 for i=1:length(for_plot)

              fprintf(fid8,'%f %g %f ',for_plot(i,:));
             fprintf(fid8,'\n');

 end
fclose(fid8);
```

Appendix D

Calculation of cement content

The Volumetric fraction of paste wass used as an input to determine the cement content of the concrete. The paste being the hydration product of cement, water-cement ratio was an essential parameter. Once that was known, the cement content was calculated in the following manner:

The phase diagram shown in fig D.1 represents volume of 1 m^3 concrete. The individual phases are shown as a fraction of volume expressed in percentage.

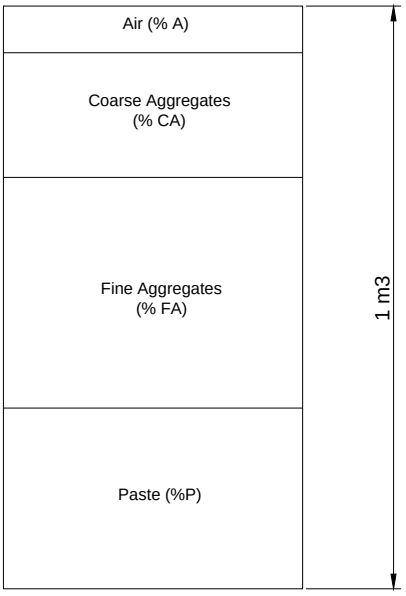

FIGURE D.1: Volumetric Phase diagram of concrete

The Paste consists of water and cement. Knowing their densities, mass content of individual phases of cement and water were determined.

$$\% \ P = \frac{W_{cem}}{\rho_{cem}} + \frac{W_{water}}{\rho_{water}}$$

Knowing the water-cement ration the equation can be modified in the following way:

$$\% \ P = \frac{W_{cem}}{\rho_{cem}} + \frac{W_{cem} \times (w/c)}{\rho_{water}}$$

Eventually the cement content was worked out:

$$W_{cem} = \frac{\%P}{100 \times (\frac{1}{\rho_{cem}} + \frac{w/c}{\rho_{water}})} \ Kg/m^3 \tag{D.1}$$

Sample	CA kg/m^3	FA kg/m^3	Cement kg/m^3	w/c ratio	Water $litre$
K27-16 (1)	1218.49	506.66	411.85	0.50	205.93
K27-16(3)	1212.78	433.40	451.55	0.50	225.77
K23-13(2)	1298.82	517.32	372.38	0.50	186.19
K23-15(2)	1111.07	455.22	497.25	0.50	248.62
K23-15(3)	1188.33	461.72	444.79	0.50	222.40
K22-16 (2)	1542.18	418.80	306.71	0.50	153.35
K22-16 (3)	1149.08	567.71	415.40	0.50	207.70
Average	1245.82	480.12	414.28	0.50	207.14

TABLE D.1: Composition by weight

Appendix E

Micro-graphs from thin sections

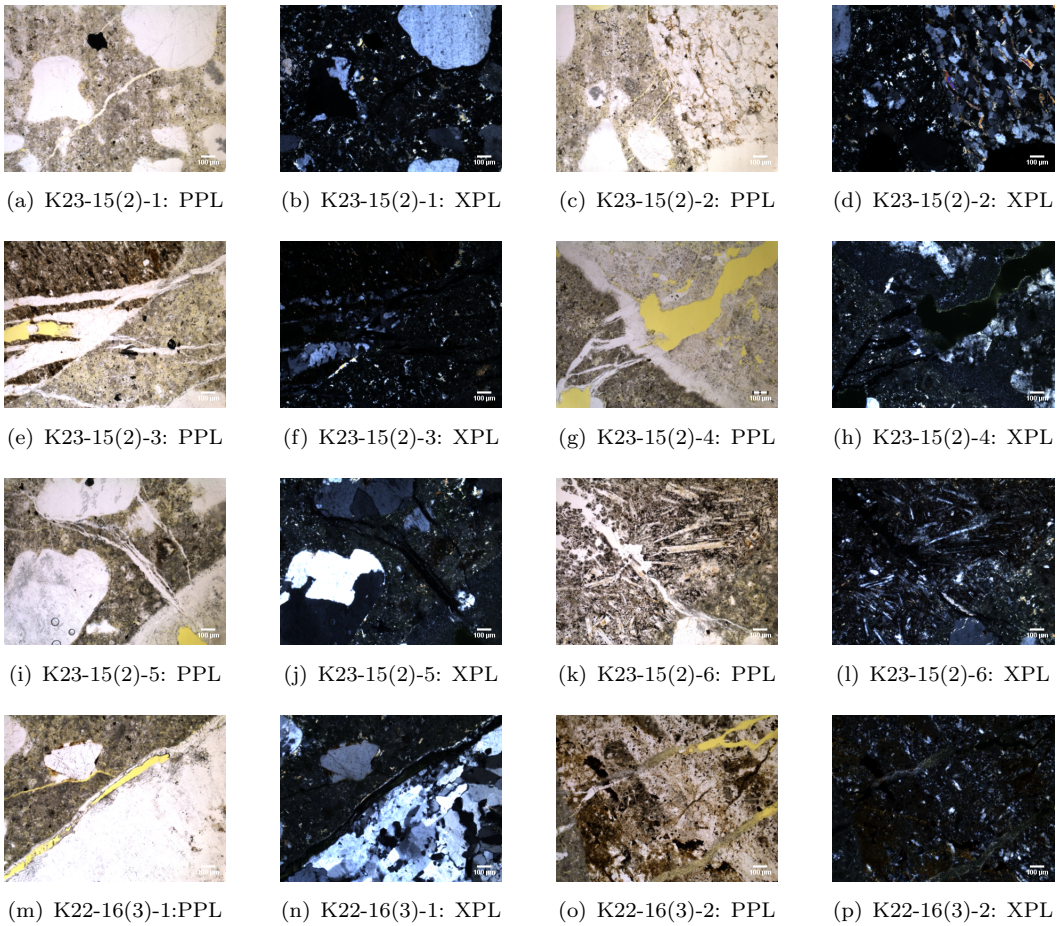

(a) K23-15(2)-1: PPL (b) K23-15(2)-1: XPL (c) K23-15(2)-2: PPL (d) K23-15(2)-2: XPL

(e) K23-15(2)-3: PPL (f) K23-15(2)-3: XPL (g) K23-15(2)-4: PPL (h) K23-15(2)-4: XPL

(i) K23-15(2)-5: PPL (j) K23-15(2)-5: XPL (k) K23-15(2)-6: PPL (l) K23-15(2)-6: XPL

(m) K22-16(3)-1:PPL (n) K22-16(3)-1: XPL (o) K22-16(3)-2: PPL (p) K22-16(3)-2: XPL

FIGURE E.1: Micro-graphs of thin sections showing ASR features-1. Field of view=1500 μm

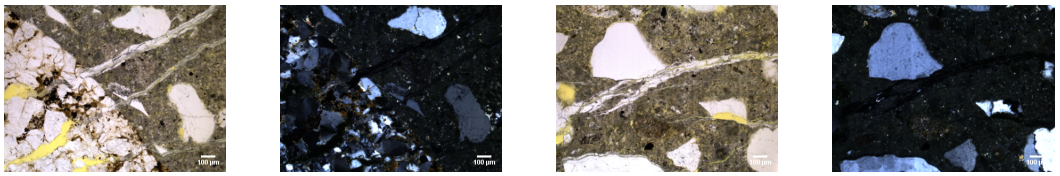

(a) K22-16(3)-3: PPL (b) K22-16(3)-3: XPL (c) K22-16(3)-4: PPL (d) K22-16(3)-4: XPL

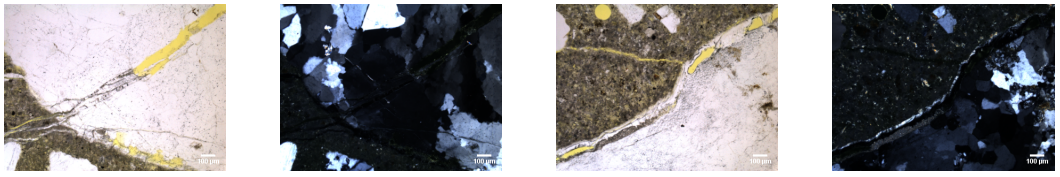

(e) K22-16(3)-5: PPL (f) K22-16(3)-5: XPL (g) K22-16(3)-6: PPL (h) K22-16(3)-6: XPL

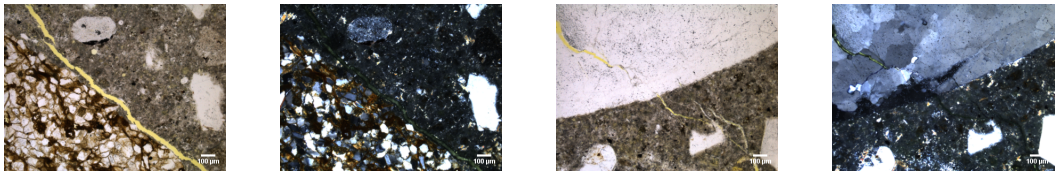

(i) K23-15(3)-1: PPL (j) K23-15(3)-1: XPL (k) K23-15(3)-2: PPL (l) K23-15(3)-2: XPL

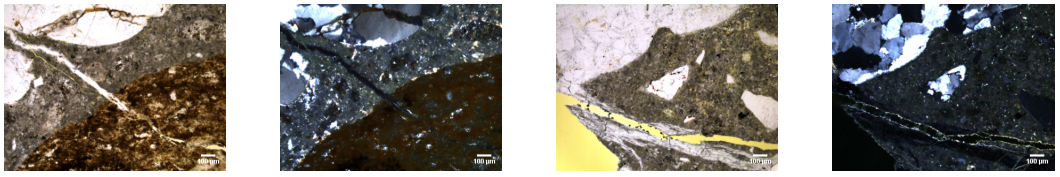

(m) K23-15(3)-3: PPL (n) K23-15(3)-3: XPL (o) K27-16(3)-1: PPL (p) K27-16(3)-1: XPL

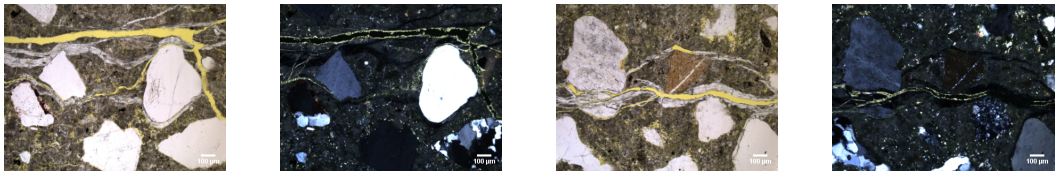

(q) K27-16(3)-2: PPL (r) K27-16(3)-2: XPL (s) K27-16(3)-3: PPL (t) K27-16(3)-3: XPL

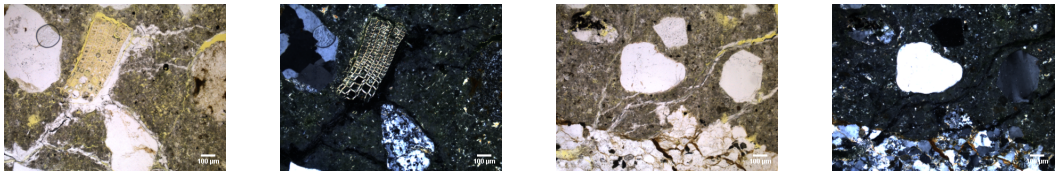

(u) K27-16(3)-4: PPL (v) K27-16(3)-4: XPL (w) K27-16(3)-5: PPL (x) K27-16(3)-5: XPL

FIGURE E.2: Micro-graphs of thin sections showing ASR features-2. Field of view=1500 μm

Appendix F

Images used for crack analysis

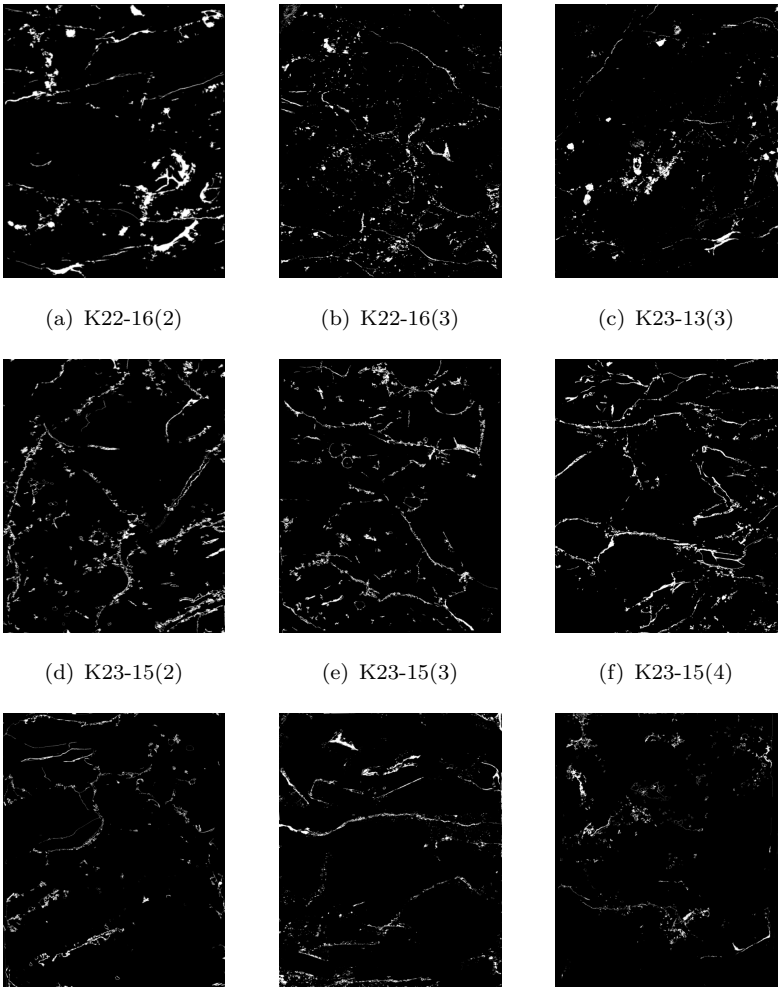

(a) K22-16(2) (b) K22-16(3) (c) K23-13(3)

(d) K23-15(2) (e) K23-15(3) (f) K23-15(4)

(g) K26-14(4) (h) K27-16(1) (i) K27-16(2)

FIGURE F.1: Images used for crack analysis

Appendix G

Crack patterns

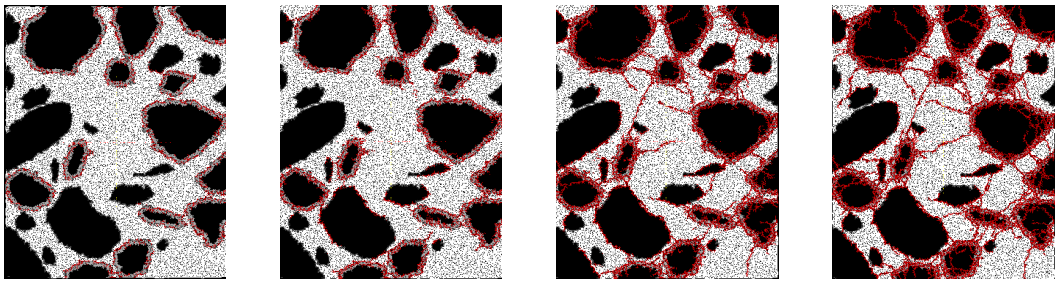

(a) K23-15(4): Step 2000

(b) K23-15(4): Step 4000

(c) K23-15(4): Step 8000

(d) K23-15(4): Step 12000

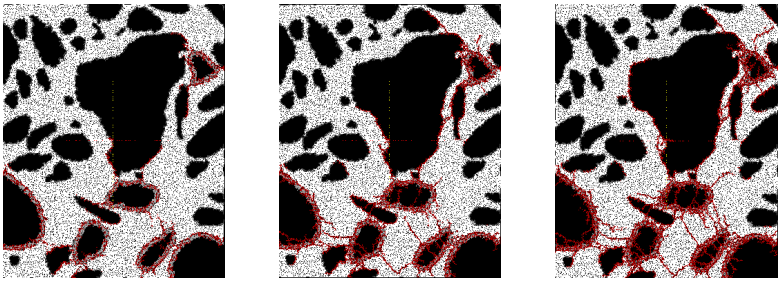

(e) K27-16(2): Step 2000

(f) K27-16(2): Step 4000

(g) K27-16(2): Step 5425

FIGURE G.1: Propagation of cracks at different stages in the simulation. Boundary Condition: Free expansions

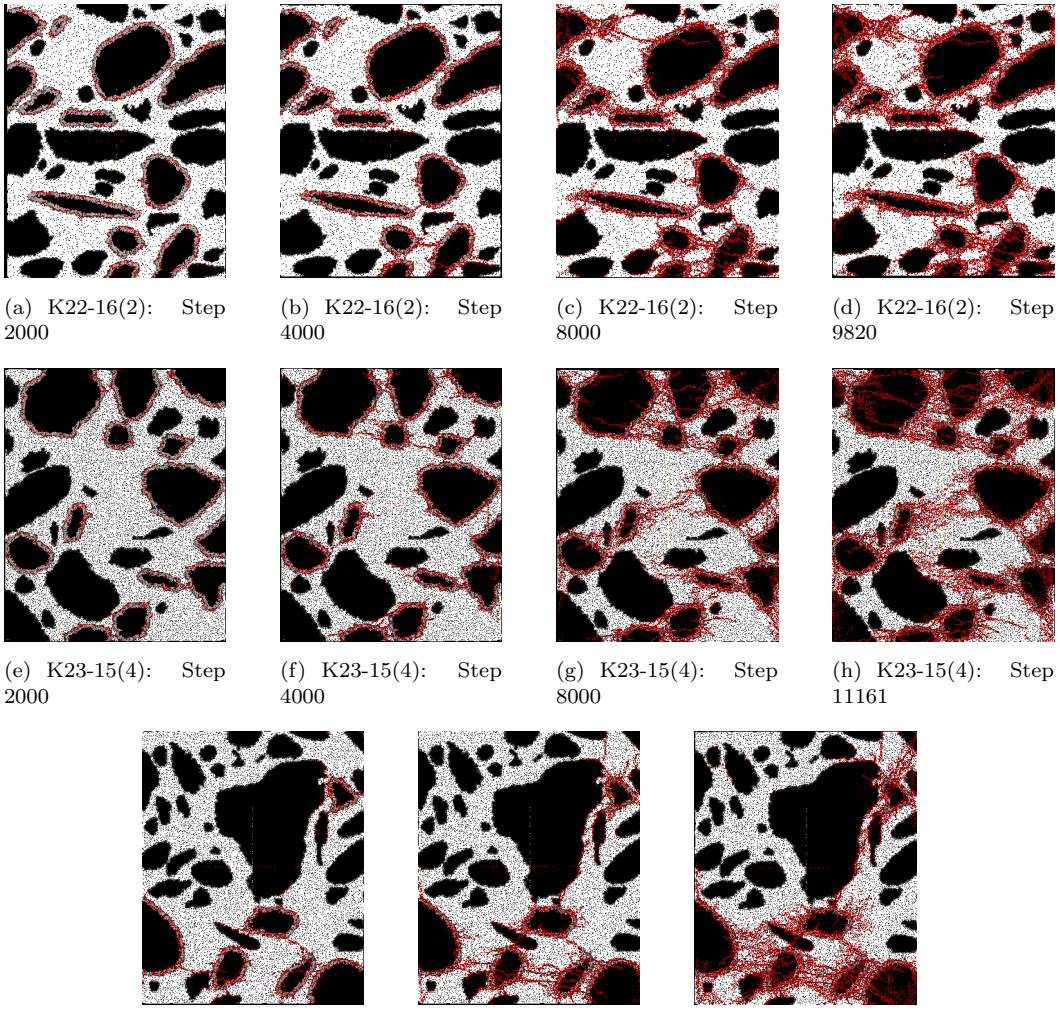

(a) K22-16(2): Step 2000

(b) K22-16(2): Step 4000

(c) K22-16(2): Step 8000

(d) K22-16(2): Step 9820

(e) K23-15(4): Step 2000

(f) K23-15(4): Step 4000

(g) K23-15(4): Step 8000

(h) K23-15(4): Step 11161

(i) K27-16(2): Step 2000

(j) K27-16(2): Step 4000

(k) K27-16(2): Step 7146

FIGURE G.2: Propagation of cracks at different stages in the simulation. Boundary Condition: Fixed edges (Full restraint)

Appendix H

Additional information

Conceptual model to estimate strains of the original sample using image analysis.

Image analysis techniques can be used to work out the expansion (strains) of the already damaged sample by calculation of the crack widths. The samples from Afsluitdijk are already eighty years old and possess a certain degree of expansion. The crack widths from the visible cracks in the image can be calculated and subsequently the original length of the samples can also be determined. This will eventually provide the strains or the expansion. This new method could prove to be useful to quantify the damage in terms of expansion and and prove to some extent more reliable than the known crack-densities method.

The method involves first extracting the binary image as obtained in 3.28(d) in a matrix form such that each cell of the matrix corresponds to one pixel of the image. Each pixel in the binary image has either of the two values: '255' which represents the crack and '0' which represents the rest. The method is explained with a help of a simple model presented in fig H.1. The model consists of a simple square specimen of size $Lx \times Ly$. The specimen is divided in smaller cell which represent each pixel having one numerical value. The specimen has two parallel vertical cracks (in red). Consider one row of the specimen as shown in the right part of fig H.1. The number of pixels corresponding to cracks (v=255) and the total number of pixels in the row can be easily computed. The algorithm for the model is written in Matlab.

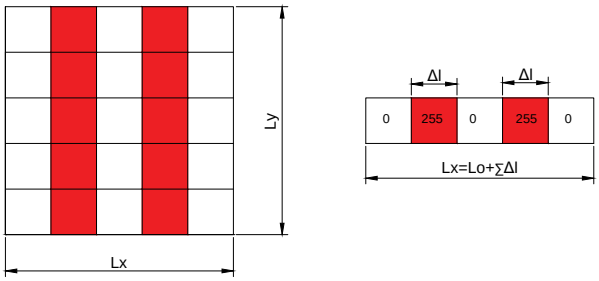

FIGURE H.1: Simple model to evaluate existing strains

Total displacement corresponding to each row corresponds to the to the total number of pixels with a pixel value equivalent to that of the cracks.

$$\delta_l = \sum \Delta l \tag{H.1}$$

The original length of the sample (undamaged state) can be calculated in the following way:

$$L_o = Lx - \delta_l \tag{H.2}$$

Knowing the displacements and the original length of the row, the total expansion (strain) of that particular row is computed:

$$\epsilon_{xx} = \frac{\delta_l}{L_o} \tag{H.3}$$

The strains of the remaining rows in the matrix are worked out in the same way and finally an average value of strains in the x direction is computed:

$$(\epsilon_{xx})_{Avg} = \frac{\sum \epsilon_{xx}}{Ly} \tag{H.4}$$

The strains in the y direction are computed in the same way:

$$(\epsilon_{yy})_{Avg} = \frac{\sum \epsilon_{yy}}{Lx} \tag{H.5}$$

The same principle is applied to the binary image created in fig 3.28 (d).

Limitations

The model can be used only if the cracks are present in one direction. The model algorithm at the moment is not able to distinguish between different crack orientation to calculate their contribution to expansions in a particular direction. However, This model can be improved upon in the future. The Matlab code is added below for reference.

```
1
2  %Estimation of expansions in damaged samples using image analysis.
3  %By Ameya Kamat
4
5  clear;
6
7  %%%Enter image dimensions in pixels%%%%
8  x=3296;                          %pixels in x
9  y=4800;                          %pixels in y
10 fid1=fopen('Crack analysis.txt'); %Open the text-image.
11 img=fscanf(fid1,'%d',[x inf]);    %Extract the image data into matlab
12 fclose(fid1);                    %matrix
13 img=img';
14 %%%%%%%For eyy%%%%%%%%%%%%%%
15 for j=1:x
16      k=0;
17      disp(j/x*100);
18 for i=1:y
19
20     if img(i,j)==255                    %255 corresponds to pixel value
21         k=k+1;                          %of cracks
22         count_y(1,j)=k;
23     else
24         count_y(1,j)=k;
25     end
26
27 end
28
29 end
30 Ly=ones(1,length(count_y))*y;
31 Lo_y=Ly-(count_y);
32 eyy=count_y./Lo_y;
33 eyy=eyy';
34 Avg_eyy=sum(eyy,1)/length(eyy);     %Average strain in y-direction
35 %%%For exx%%%%%%%%%
36 for i=1:y
37      k=0;
38      disp(i/y*100);
39 for j=1:x
40
41     if img(i,j)==255
42         k=k+1;
43         count_x(i,1)=k;
44     else
45         count_x(i,1)=k;
46     end
47
```

```
48 end
49
50 end
51
52 Lx=ones(length(count_x),1)*x;
53 Lo_x=Lx-(count_x);
54 exx=count_x./Lo_x;
55 Avg_exx=sum(exx,1)/length(exx);   %Average strain in x-direction
56
57 %----------------------END-------------------------------------
```

Bibliography

Ahmed, T., Burley, E., Rigden, S., and Abu-Tair, A. I. (2003). The effect of alkali reactivity on the mechanical properties of concrete. *Construction and Building Materials*, 17(2):123–144.

Anaç, C. (2016). *Assessment of damage due to alkali silica reaction in concrete structures (Draft)*. Doctoral thesis, Delft University of Technology.

Andiç-Çakir, Ö., Poole, A. B., and Ideker, J. H. (2016). ICAAR 1974 2016 conferences for examination of AAR in concrete. *Construction Materials*, 169(CM3):119–127.

Bažant, Z., Zi, G., and Meyer, C. (2000). Fracture mechanics of ASR in concretes with waste glass particles of different sizes. *Journal of Engineering Mechanics*, 126(3):226–232.

Borsje, H. and Swinkels, M. (2016). Integrale rapportage van het westelijk deel van de spuisluizen te Kornwerderzand (Lorentzsluizen). Technical report, TNO and SGS Intron, Delft.

Borsje, H. and Zwarthoed, J. M. (2008). Lock complexes in the Afsluitdijk (IJsselmeer dam) Study of the residual lifetime of the concrete parts Sub-report 04 - Structural design of the lock complexes. Technical report, TNO and SGS Intron, Delft.

Boutz, M., Borsje, H., and Zwarthoed, J. M. (2008). Lock complexes in the Afsluitdijk (IJsselmeer dam) Study of the residual lifetime of the concrete parts Sub-report 05 - Knowledge status for alkali-silica reaction (ASR). Technical report, TNO and SGS Intron, Delft.

Broekmans, M. A. (2002). *The Alkali-Silica Reaction: Mineralogical and geochemical aspects of some Dutch concretes and Norwegian mylonites*. Doctoral thesis, University of Utrecht.

Capra, B. and Sellier, A. (2003). Orthotropic modelling of alkali-aggregate reaction in concrete structures: Numerical simulations. *Mechanics of Materials*, 35(8):817–830.

Charpin, L. and Ehrlacher, A. (2012). A computational linear elastic fracture mechanics-based model for alkali-silica reaction. *Cement and Concrete Research*, 42(4):613–625.

Chatterji, S. (2005). Chemistry of alkali-silica reaction and testing of aggregates. *Cement and Concrete Composites*, 27(7-8):788–795.

Comby-Peyrot, I., Bernard, F., Bouchard, P. O., Bay, F., and Garcia-Diaz, E. (2009). Development and validation of a 3D computational tool to describe concrete behaviour at mesoscale. Application to the alkali-silica reaction. *Computational Materials Science*, 46(4):1163–1177.

Çopuroğlu, O. (2010). Effect of Silica Dissolution on the Mechanical Characteristics of Alkali-Reactive Aggregates. *Journal of Advanced Concrete Technology*, 8(1):5–14.

Çopuroğlu, O. (2013). Microanalysis of crystalline ASR products from a 50 year-old concrete structure. In *14th Euroseminar on Microscopy Applied to Building Materials*, Helsingør, Denmark. International Cement Microscopy Association.

Çopuroğlu, O. (2016). Revealing the Dark Side of Portlandite Clusters in Cement Paste by Circular Polarization Microscopy. *Materials*, 9(3):176.

Çopuroğlu, O. and Schlangen, E. (2007). Modelling of Effect of ASR on Concrete Microstructure. *Key Engineering Materials*, 348-349:809–812.

Dent Glasser, L. S. and Kataoka, N. (1981). The chemistry of 'alkali-aggregate' reaction. *Cement and Concrete Research*, 11(1):1–9.

Diamond, S. (1989). ASR Another look at mechanisms. *In Proceedings of the Eight International Conference on Alkali Aggregate Reaction in Concrete*, pages 83– 94.

Eden, M. A. (2010). A code of practice for the petrographic examination of concrete. Technical Report July.

Esposito, R., Anac, C., Hendriks, M. A., and Copuroglu, O. (2016). Influence of the alkali-silica reaction on the mechanical degradation of concrete. *Journal of materials in civil engineering*, 28(6):13.

Federal Highway Administration (2012). Alkali-Aggregate reaction workshops for engineers and practioners. Technical Report November, US Department of Transportation.

Fernandes, I., Ribeiro, M. d. A., Broekmans, M. A. T. M., and Sims, I., editors (2016). *Petrographic Atlas: Characterisation of Aggregates Regarding Potential Reactivity to Alkalis*. Number September. Springer Netherlands, Dordrecht, 1 edition.

Fournier, B. and Bérubé, M.-A. (2000). AlkaliAggregate Reaction in Concrete: a Review of Basic Concepts and Engineering Implications. *Canadian Journal of Civil Engineering*, 27:167–191.

Grattan-Bellew, P. E. and Mitchell, L. D. (2006). Quantitative petrographic analysis of concrete - the damage rating index (dri) method, a review. *Proc.Marc-Andre Brub Symp.on Alkali-Aggregate Reactivity in Concrete*, pages 321–334.

Haha, M. B., Gallucci, E., Guidoum, A., and Scrivener, K. L. (2007). Relation of expansion due to alkali silica reaction to the degree of reaction measured by SEM image analysis. *Cement and Concrete Research*, 37(8):1206–1214.

Haha, M. B. E. N. (2006). *Mechanical effects of alkali silica reaction in concrete studied by sem-image analysis*. Phd thesis, Swiss Federal Institute of Technology in Lausanne.

Hobbs, D. W. (1986). Alkali Silica Reaction in Concrete. *Structural Engineer*, 64 A(12):381–383.

Jakobsen, U. H., Laugesen, P., and Thaulow, N. (2000). Determination of Water-Cement Ratio in Hardened Concrete by Optical Fluorescence Microscopy, Water-Cement Ratio and Other Durability Parameters - Techniques for Determination. *ACI International*, 191(3).

Jensen, V. (1993). *Alkali Aggregate Reaction in Southern Norway*. PhD thesis, Norwegian Institute of Technology, Trondheim.

Karthik, M. M., Mander, J. B., and Hurlebaus, S. (2016). ASR/DEF related expansion in structural concrete: Model development and validation. *Construction and Building Materials*, 128:238–247.

Lindgård, J. (2013). *Alkali Silica Reaction (Performance Testing)*. Doctoral thesis, Norwegian University of Science and Technology.

Morenon, P., Multon, S., Sellier, A., Grimal, E., Hamon, F., and Bourdarot, E. (2017). Impact of stresses and restraints on ASR expansion. *Construction and Building Materials*, 140:58–74.

Multon, S. and Toutlemonde, F. (2006). Effect of applied stresses on alkali-silica reaction-induced expansions. *Cement and Concrete Research*, 36(5):912–920.

Neville, A. M. (2011). *Properties of Concrete*. Pearson Education Ltd., Essex, 5th edition.

Nijland, T. G. and de Bruijn, W. A. (2002). New Dutch guideline on ASR-prevention. *HERON*, 47(2):87–93.

Nixon, P. J. and Sims, I., editors (2016). *RILEM Recommendations for the Prevention of Damage by Alkali-Aggregate Reactions in New Concrete Structures*, volume 17 of *RILEM State-of-the-Art Reports*. Springer Netherlands, Dordrecht.

Perras, M. A. and Diederichs, M. S. (2014). A Review of the Tensile Strength of Rock : Concepts and Testing. *Geotech Geol Eng*, 32:525–546.

Poole, A. B. and Sims, I. (2015). *Concrete Petrography*. CRC Press, 2016 edition.

Qian, Z. (2008). *3D Lattice Analysis of Cement Paste*. Msc thesis, Delft University of Technology.

Reinhardt, H. W. and Mielich, O. (2011). A fracture mechanics approach to the crack formation in alkali-sensitive grains. *Cement and Concrete Research*, 41(3):255–262.

Rivard, P., Fournier, B., and Ballivy, G. (2000). Quantitative Petrographic Technique for Concrete Damage Due to ASR : Experimental and Application. *Cement, Concrete and Aggregates*, 22(1):63–72.

Sanchez, L. F. M., Fournier, B., Jolin, M., Bastien, J., and Mitchell, D. (2016). Practical use of the Stiffness Damage Test (SDT) for assessing damage in concrete infrastructure affected by alkali-silica reaction. *Construction and Building Materials*, 125:1178–1188.

Sanchez, L. F. M., Fournier, B., Jolin, M., and Duchesne, J. (2015). Reliable quantification of AAR damage through assessment of the Damage Rating Index (DRI). *Cement and Concrete Research*, 67:74–92.

Saouma, V. and Perotti, L. (2006). Constitutive model for alkali-aggregate reactions. *ACI Materials Journal*, 103(3):194–202.

Šavija, B., Pacheco, J., and Schlangen, E. (2012). Meso-Scale Simulation of Chloride Ingress in Cracked Concrete. In *Second International Conference on Microstructural-related Durability of Cementitious Composites*, number April, Amsterdam.

Schlangen, E. and Çopuroğlu, O. (2010). Modeling of expansion and cracking due to ASR with a 3D lattice model. *7th International Conference on Fracture Mechanics of Concrete and Concrete Structures*, pages 1017 –1023.

Schlangen, E. and Garboczi, E. J. E. (1997). Fracture Simulations of concrete Using Lattice Models: Computational Aspects. *Engineering Fracture Mechanics*, 57(2):319–332.

Schlangen, E. and van Breugel, K. (2005). Prediction of tensile strength reduction of concrete due to ASR. In *3th International Conference on Construction Materials, Performance, Innovations and Structural Implications*, pages 1–10.

Schlangen, E. and van Mier, J. (1992). Experimental and numerical analysis of micromechanisms of fracture of cement-based composites. *Cement and Concrete Composites*, 14(2):105–118.

Shayan, A. and Song, G.-L. (2000). Electrochemical effects of com- bined AAR and cathodic protection in concrete. In *11th International conference pn Alkali-Aggregate Reactions in concrete*, Québec.

Silva de Souza, L. M. (2016). *Electrochemical Lithium Migration To mitigate alkali silica reaction in existing concrete structures*. TU Delft, Delft.

Stanton, T. (1940). Expansion of concrete through reaction between cement and aggregate. *ASCE*, 66(10):1781–1811.

Swamy, R. N. (1992). *The Alkali-Silica Reaction in concrete*, volume 14. Blackie and Son ltd.

van Mier, J. (2012). *Concrete fracture : A multiscale approach*. CRC Press.

Vervuurt, A. (1997). *Interface Fracture in Concrete*. Doctoral thesis, Delft University of Technology.

Villeneuve, V., Fournier, B., and Duchesne, J. (2012). Determination of the damage in concrete affected by ASR- the damage rating index (DRI). *Proceedings of the 14th International Conference on Alkali-Aggregate Reaction in Concrete*, page 10.

Vree, R. T. D., Haverkort, R., Bakker, J. D., Berg, D., Bruijn, W. a. D., Dieleman, W. a., Rijnsburger, H. a., and Sagel, R. (2005). Measures to prevent damage to concrete by alkali-silica reaction (ASR). Technical report, CUR-Recommendation 89.

Wigum, B. J. (1995). Examination of microstructural features of Norwegian cataclastic rocks and their use for predicting alkali-reactivity in concrete. *Engineering Geology*, 40(3-4):195–214.

Wigum, B. J. (2006). Alkali Aggregate Reactions (AAR) in Concrete . Testing , Mitigation & Recommendations . The Norwegian approach during 15 years of research. In Fournier, B., editor, *Eighth CANMET/ACI International Conference on Recent Advances in Concrete Technology*, pages 111–128, Montréal, Québec, Canada.

Yurtdas, I., Chen, D., Hu, D. W., and Shao, J. F. (2013). Influence of alkali silica reaction (ASR) on mechanical properties of mortar. *Construction and Building Materials*, 47:165–174.